Finite Element Analysis of Shells with Layers

by

Jean-François N. Hiller

Submitted to the Department of Mechanical Engineering
in partial fulfillment of the requirements for the degree of

PhD in Mechanical Engineering

at the

MASSACHUSETTS INSTITUTE OF TECHNOLOGY

September 2002

Author .....

Department of Mechanical Engineering
August 23, 2002

Certified by .....

Klaus-Jürgen Bathe
Professor
Thesis Supervisor

Accepted by .....

Ain Ants Sonin
Chairman, Department Committee on Graduate Students

Finite Element Analysis of Shells with Layers

by

Jean-François N. Hiller

Submitted to the Department of Mechanical Engineering
on August 23, 2002, in partial fulfillment of the
requirements for the degree of
PhD in Mechanical Engineering

Abstract

It is well established that thin shell structures frequently feature narrow bands of strain concentration and localized displacement irregularities referred to as boundary and internal layers. It is crucial to capture these layers properly as they can be sources of structural failures. Unfortunately, while the absence of analytical solutions to most shell problems of practical interest has spawned the development of a variety of finite element formulations over the years, largely speaking these schemes were proposed without a rigorous and comprehensive testing procedure available. We are now faced with a wealth of existing formulations and little way to assess their ability to model boundary and internal layers.

Most of the difficulties in assessing the performance of shell finite elements stem from the use of mixed formulations. These are necessary to alleviate the locking phenomenon present in bending-dominated problems when displacement-based formulations are used.

We develop a new error measure approach that is physically-based and can be used to assess the performance of mixed-interpolated shell finite element formulations. We apply this approach to the MITC (Mixed Interpolation of Tensorial Components) family of shell elements, a widely-used mixed formulation. We focus in particular on the performance of these elements when employed to analyze problems featuring layers, and specifically we assess the effect of mesh refinement in the regions where layers are present. We demonstrate that the MITC elements are consistent with the basic shell model and find that local mesh refinement allows us to obtain optimal order convergence of the MITC solution to the solution of the mathematical model even in the presence of layers.

The proposed error measure can be easily extended to other mixed-formulated finite elements used for problems such as incompressible materials and fluids, beams or plates.

Thesis Supervisor: Klaus-Jürgen Bathe
Title: Professor

Acknowledgments

First and foremost, I would like to express my deep and sincere gratitude to my advisor, Professor Klaus-Jürgen Bathe, for his advice, guidance and encouragement throughout the course of this work. His enthusiasm for the topic was greatly inspirational. I am also thankful to the other members of my Thesis Committee, Professor Eduardo Kausel and Professor Tomasz Wierzbicki. Their suggestions and contributions are very much appreciated.

I am also grateful to Professor Jean Salençon for introducing me to the world of Mechanical Engineering. To this day I have fond memories of his lectures.

I also wish to thank my labmates at the Finite Element Research Group, Dr. Dena Hendriana, Dr. Alexander Iosilevich, Dr. Suvranu De, Dr. Sandra Rugonyi, Ramon Silva, Juan Pontaza, Denise Poy, Phill-Seung Lee, Jung-Wuk Hong, SeongHwa Park, Bahareh Banijamali, Jacques Olivier, Muhammed Baig, for their help and friendly support.

While at MIT, I received financial help from the MTS Corporation Fellowship, the Rocca Fellowship and a Renault SA fellowship. Their support is gratefully aknowledged.

Finally, my utmost gratitude is due to my wife, Jeri'Ann, for her unconditional support, love and affection.

Contents

List of Figures

List of Tables

Introduction

Preliminaries

The use of numerical methods is a well-established practice in the analysis of shell structures. Indeed, while analytical methods can be employed to some extent in the study of simple problems of academic interest, in industry the geometric complexity of the shell structures involved, along with the complexity of even simplified shell equations, frequently prohibits any analytical work. As a matter of fact, most of the analytical studies of shells focus on structures with very simple mid-surface geometries –such as cones, cylinders, hyperbolic paraboloids– and boundary conditions (see for instance [25, 37, 38]) which are of interest for certain types of applications but lack generality.

Specifically, a variety of finite element formulations have been developed over the years and are used in research and industry today [11]. For a large part, these formulations were proposed without a rigorous and comprehensive testing procedure available. We are now faced with a wealth of existing formulations, not to mention new ones still being developed, and little way to separate the oats from the hay [22].

To make matters worse, the push for lighter, more efficient and more appealing structures leads to the use of thinner shells in engineering designs, a trend that is bound to continue with the increased reliance on engineered materials and the development of nanotechnologies. It is recognized that these thin structures frequently feature narrow bands of strain concentration and localized displacement irregularities referred to as boundary and internal layers. The importance of modelling and understanding these layers is crucial since they can be sources of structural failure

[25].

Despite the long history of research in shell structures, the behavior of shell structures of small thickness (asymptotic analysis) has only been investigated fairly recently. These limit behaviors play a major role in conditioning the performance of finite element formulations. For instance, it is well-known that the basic displacement-based shell elements suffer from unreasonably high stiffness when thin shells acting mostly in bending action are considered. This phenomenon is referred to as 'locking'. If a bending-dominated structure is analyzed with displacement-based finite elements, element sizes may need to be chosen of the same order as the shell thickness or smaller [11] in order to compensate for locking and to obtain a reasonably accurate solution. This is obviously an impractical proposal.

To overcome these difficulties, numerous alternative finite element formulations have been developed and in particular mixed-interpolation degenerated formulations are now widely used in industry. One of these formulations is the Mixed Interpolation of Tensorial Components (MITC) approach (see [17, 18, 24]). However, a complete, rigorous analysis of the performance of mixed formulations is still lacking. Considering problems featuring boundary and internal layers, almost nothing is known about the convergence properties of existing finite element formulations and how they are impacted by the various meshing strategies.

In this work, we propose to develop a new error measure approach that can be used to assess the performance of mixed-interpolated formulations, and to apply this approach to the MITC family of shell elements. We focus in particular on the performance of these elements when employed to analyze problems featuring layers, and specifically assess the effect of mesh refinement in the regions where layers are present.

Thesis outline

The outline of this document is as follows.

In Chapter 1, we review the derivation of the basic shell mathematical model and its fundamental properties. This chapter is mostly intended to introduce basic

concepts and notations used throughout the rest of the document. Indeed, there are many textbooks dedicated to shell models (see Bibliography) and it is not our intention to summarize them here. For a modern and complete coverage of shell models we refer to [22], the notations of which we follow in this thesis.

Chapter 2 focuses on the asymptotic behavior of shells, that is, the behavior of shell structures as their thickness is reduced to zero. Very distinctive limit behaviors are possible with problems fitting in the categories of being bending-dominated, membrane-dominated or mixed. We show that boundary and internal layers may develop in the structure when the shell thickness decreases. We relate the appearance of these layers to the presence of singularities in the applied loadings or the shell geometry, and boundary conditions. We recall that characteristic widths of layers are determined by the local mid-surface geometry, and specifically the second form of the mid-surface, which determines whether the surface is elliptic, parabolic of hyperbolic, is critical. We illustrate these points with a number of finite element simulations that feature typical layers in shells of all geometric natures.

The finite element approach to shell problems is introduced in Chapter 3. We start with the displacement-based formulation and explain why this formulation shows poor performance ('locking') in bending-dominated problems. The MITC family of elements is then introduced and their formulation justified. We then briefly review the conditions a mixed finite element formulation such as the MITC scheme needs to satisfy for optimality. Unfortunately, these conditions can rarely be shown to hold analytically and numerical tests are in order to assess the performance of a finite element formulation. Critical issues in the selection of appropriate benchmark problems are listed, such as the need to study problems that feature boundary and internal layers.

The next chapter focuses on how to evaluate the discrepancy between the exact solution of a mathematical shell problem and the finite element solution of this problem. First we review the techniques that have historically been used to assess this finite element error and we show the limitations of these existing approaches. We propose an alternative error measure that is shown not to have the same limitations as the

current techniques. This novel approach is used to study the consistency and convergence properties of the MITC family of elements. To that end, we introduce two new benchmark problems which we show to be bending- and membrane-dominated. Both problems feature boundary layers. These problems, along with the Scordelis-Lo roof problem, a classic benchmark with a mixed asymptotic behavior, allow us to study the convergence properties of the MITC element when different meshing schemes are employed.

In Appendix A, we list the explicit expressions for the components of the strain / displacement tensor for the MITC4 element in terms of the node locations, director vectors, nodal thicknesses and local coordinates. These expressions can be used to implement the MITC4 element in a more computationally efficient way. Speed improvements are reported.

In Appendix B, we apply our proposed error measure to a Timoshenko cantilever beam. This structure, which features some of the basic behaviors of shell structures, allows for analytical calculations of exact and finite element solutions. In particular, we focus our attention on the behavior of our proposed error measure, but we also demonstrate a number of alternative error measures that have been advocated in the literature.

In Appendix C, we demonstrate the use of two alternative error measures that have been proposed for membrane-dominated and bending-dominated problems.

Finally, in Appendix D, we propose a modified MITC9 formulation that aims at correcting the shear locking behavior observed in the standard MITC9 element in one of the new benchmark problems introduced in Chapter 4. The performance of this new element in our test problems is reported.

Chapter 1

Basics of Shell Theory

The purpose of this first chapter is to review some classical results regarding shell theory while introducing the notations employed throughout this thesis.

First, we show what kinematic assumptions are made in the derivation of some classical shell models from three-dimensional analysis. This allows us to derive the dependance of strains and stresses on the assumed displacements. The classical Galerkin procedure then yields the variational formulation for shells. We also show how this variational formulation can be derived from the fundamental energy principles.

Plate and shell models show some similarities as some phenomena such as "shear locking" encountered in the study of shell finite element models are also observed when dealing with plate finite element models. Of course, because of their curved nature, shell finite element models also exhibit behaviors that have no equivalent in plate finite element models, such as "membrane locking". However, to gain insight into shell behaviors, we will occasionally use plates as particular examples of shells to illustrate complex behaviors that cannot be dealt with analytically in the context of a general shell geometry . It is therefore important to understand the similarities and differences in the behavior of mathematical models for shells and plates. Also, plate models can be described as a springboard for the analysis of shells: the analysis of plate models presents some of the difficulties encountered in the analysis of shell

models but are easier to study analytically. In fact, some shell finite element models were historically derived from plate models (see the MITC elements for instance [17]). For this reason, we occasionally extend our discussion of shells to plates.

1.1 Tensorial notations

In the following, it is assumed that the reader is familiar with standard results and notation conventions of differential geometry and with standard methods and results of tensor analysis. We refer to [22, 11, 28, 51, 52] for a presentation of tensorial analysis and to [22, 28] for an introduction to differential analysis.

We adopt the following notations for tensors:

$$\begin{cases} \vec{A} & \text{denotes the first order volume tensor A} \\ \overset{2\rightarrow}{A} & \text{denotes the second order volume tensor A} \\ \overset{4\rightarrow}{A} & \text{denotes the fourth order volume tensor A} \\ \bar{A} & \text{denotes the first order surface tensor A} \\ \overset{2-}{A} & \text{denotes the second order surface tensor A} \\ \overset{4-}{A} & \text{denotes the fourth order surface tensor A} \end{cases} \tag{1.1}$$

We introduce the following special fourth-order tensors:

$$I^{ijkl} = (\overset{4\rightarrow}{I})^{ijkl} = \frac{1}{2}(g^{ik}g^{jl} + g^{il}g^{jk}) \tag{1.2}$$

$$J^{ijkl} = (\overset{4\rightarrow}{J})^{ijkl} = \frac{1}{2}(g^{ik}g^{jl} + g^{il}g^{jk}) - \frac{1}{3}g^{ij}g^{kl} \tag{1.3}$$

and

$$K^{ijkl} = (\overset{4\rightarrow}{K})^{ijkl} = \frac{1}{3}g^{ij}g^{kl} \tag{1.4}$$

with the obvious relation:

$$\overset{4\rightarrow}{I} = \overset{4\rightarrow}{J} + \overset{4\rightarrow}{K} \tag{1.5}$$

These tensors satisfy the following important properties, where $\overset{2\rightarrow}{e}$ is an arbitrary

second order volume tensor:

$$\overset{4\rightarrow}{I} : \overset{2\rightarrow}{e} = \overset{2\rightarrow}{e} \tag{1.6}$$

$$\overset{4\rightarrow}{K} : \overset{2\rightarrow}{e} = \frac{1}{3} Tr(\overset{2\rightarrow}{e}) \ \overset{2\rightarrow}{I} \tag{1.7}$$

$$\overset{4\rightarrow}{J} : \overset{2\rightarrow}{e} = \overset{2\rightarrow}{e} - \frac{1}{3} Tr(\overset{2\rightarrow}{e}) \ \overset{2\rightarrow}{I} \tag{1.8}$$

where the term on the right hand side of Equation 1.8 is the deviatoric part of $\overset{2\rightarrow}{e}$ and the right hand side of Equation 1.7 is the non-deviatoric part of $\overset{2\rightarrow}{e}$. Of course $Tr(\overset{2\rightarrow}{e})$ denotes the trace of $\overset{2\rightarrow}{e}$, i.e. $Tr(\overset{2\rightarrow}{e}) = e^i_i$. Finally these tensors satisfy:

$$\begin{cases} \overset{4\rightarrow}{I} : \overset{4\rightarrow}{I} = \overset{4\rightarrow}{I} \quad ; & \overset{4\rightarrow}{J} : \overset{4\rightarrow}{J} = \overset{4\rightarrow}{J} \quad ; & \overset{4\rightarrow}{K} : \overset{4\rightarrow}{K} = \overset{4\rightarrow}{K} \quad ; & \overset{4\rightarrow}{J} : \overset{4\rightarrow}{K} = \overset{4\rightarrow}{K} : \overset{4\rightarrow}{J} = 0 \\ \overset{4\rightarrow}{I} : \overset{2\rightarrow}{I} = \overset{2\rightarrow}{I} = \overset{4\rightarrow}{K} : \overset{2\rightarrow}{I} \quad ; & \overset{4\rightarrow}{J} : \overset{2\rightarrow}{I} = \overset{2\rightarrow}{0} \quad ; & & \\ \overset{4\rightarrow}{I} : \overset{2\rightarrow}{d} = \overset{4\rightarrow}{J} : \overset{2\rightarrow}{d} = \overset{2\rightarrow}{d} \quad ; & \overset{4\rightarrow}{K} : \overset{2\rightarrow}{d} = \overset{2\rightarrow}{0} \quad ; & \overset{2\rightarrow}{d} : \overset{2\rightarrow}{I} = \overset{2\rightarrow}{I} : \overset{2\rightarrow}{d} = 0 & \end{cases} \tag{1.9}$$

where $\overset{2\rightarrow}{d}$ is the deviatoric part of an arbitrary second order symmetric tensor.

1.2 Derivation of the shell variational formulation for a continuum

In this section, we summarize the presentation of [22, 21]. This approach is justified by the results of [21] summarized in [20].

1.2.1 The shell geometry and its parametrization

We consider a three-dimensional solid occupying at rest a volume Ω and 'thin' (This condition will be quantified later on) in one direction compared to its other two directions.

In our later analysis, we restrict ourselves to a subset of such solids: we consider only the case where any point $\vec{x}$ in the volume Ω can be uniquely described by a

triplet of coordinates (ξ^1, ξ^2, ξ^3) such that $(\xi^1, \xi^2) \in \omega$ (with ω an open domain in $\mathbb{R}^2$) and $\xi^3 \in]-\frac{t(\xi^1,\xi^2)}{2}; \frac{t(\xi^1,\xi^2)}{2}[$,

$$\vec{x}\ (\xi^1, \xi^2, \xi^3) = \vec{\phi}\ (\xi^1, \xi^2) + \xi^3\ \vec{a}_3\ (\xi^1, \xi^2) \tag{1.10}$$

where

$$\vec{a}_\alpha\ (\xi^1, \xi^2) = \frac{\partial\ \vec{\phi}\ (\xi^1, \xi^2)}{\partial \xi^\alpha (\xi^1, \xi^2)} \tag{1.11}$$

and

$$\vec{a}_3\ (\xi^1, \xi^2) = \frac{\vec{a}_1\ (\xi^1, \xi^2) \wedge \vec{a}_2\ (\xi^1, \xi^2)}{||\ \vec{a}_1\ (\xi^1, \xi^2) \wedge \vec{a}_2\ (\xi^1, \xi^2)||}. \tag{1.12}$$

With this notation, $\vec{\phi}\ (\xi^1, \xi^2)$ represents the mapping function, $t(\xi^1, \xi^2)$ is the thickness of the shell at the point $\vec{x}\ (\xi^1, \xi^2, 0) = \vec{\phi}\ (\xi^1, \xi^2)$ measured in the direction of $\vec{a}_3\ (\xi^1, \xi^2)$, and $\vec{a}_3\ (\xi^1, \xi^2)$ is the vector normal to the mid-surface at that point. In the following, we will frequently use the simplified notation $\vec{a}_3$ instead of $\vec{a}_3\ (\xi^1, \xi^2)$, etc, and we will only consider the case where the thickness is constant and satisfies

$$t < 2 \inf_{(\xi^1,\xi^2)\in\omega} |R_{min}(\xi^1, \xi^2)| \tag{1.13}$$

where $R_{min}(\xi^1, \xi^2)$ denotes the radius of curvature with the smallest absolute value at the point corresponding to the coordinates (ξ^1, ξ^2) (The latter criterion is required to ensure the application $(\xi^1, \xi^2, \xi^3) \rightarrow \vec{x}$ is injective and quantifies the notion of thinness of the solids that fall under the shell description).

Note that we have restricted ourselves to the study of shells described by a single mapping. In fact, the geometry of most shells of practical interest can not be rendered by a single mapping. However, in practical applications, the geometry of a shell structure can be rendered by a finite number of mappings $\vec{\phi}_i$ defined over measurable sets ω_i (see [30]), and it can be shown that our analysis can be extended to that case. Considering problems defined by a single mapping function is therefore not a restriction to the theory, but it allows for a clearer presentation.

1.2.2 Derivation of the shell model

In this section we give the displacement assumptions, then derive the corresponding strains and, under the plane stress assumption, stresses. We then employ the classical Galerkin method to attain the general variational problem. We also present this variational problem as a consequence of the minimization of the potential energy.

Displacement assumptions It is assumed that the displacements $\vec{U}\ (\xi^1, \xi^2, \xi^3)$ of all points in the shell can be described by the triplet of functions $\vec{u}\ (\xi^1, \xi^2)$ and $\theta_\lambda(\xi^1, \xi^2)$ in the form:

$$\vec{U}\ (\xi^1, \xi^2, \xi^3) = \vec{u}\ (\xi^1, \xi^2) + \xi^3 \theta_\lambda(\xi^1, \xi^2)\ \vec{a}_\lambda\ (\xi^1, \xi^2) \tag{1.14}$$

The regularity conditions that the functions involved must satisfy in order for the model to make sense and for the resulting shell problem to be well-posed will be considered in Section 1.2.6. Of course, the solution must also satisfy the essential (i.e. displacement) boundary conditions (We only consider here the case where the boundary conditions imposed are sufficient to prevent rigid body motions, and where the imposed essential boundary conditions are all clamped conditions, i.e. all the imposed displacements are zero. These restrictions are only for the clarity of the presentation and other boundary conditions can be considered). We denote by $\mathcal{V}$ the space of admissible displacements of the form given by Equation 1.14. It is important to recognize the assumption that is being made here, namely that straight lines that are originally orthogonal to the mid-surface of the shell remain straight in the deformed configuration. In general these lines do not remain orthogonal to the mid-surface of the shell, because the functions $\theta_\lambda(\xi^1, \xi^2)$ are independent functions that are not related to the function $\vec{u}\ (\xi^1, \xi^2)$ that describes the displacements of the mid-surface. This kinematic assumption is known as the Reissner-Mindlin assumption [45, 50].

From displacements to strains Under these displacement assumptions, we can derive the strain fields by making use of the definition of the Green-Lagrange strain tensor (with $\vec{g}^{\,i}$ denoting the 3D contravariant base vectors):

$$\overset{2}{\vec{\epsilon}} = \epsilon_{ij}\ \vec{g}^{\,i} \otimes \vec{g}^{\,j} = \frac{1}{2}({}^1\vec{g}_i.{}^1\vec{g}_j - {}^0\vec{g}_i.{}^0\vec{g}_j)\ \vec{g}^{\,i} \otimes \vec{g}^{\,j} \tag{1.15}$$

where the left superscript 0 denotes the original configuration and the left superscript 1 denotes the deformed configuration. Since we are only concerned here with linear analysis, we make use of the linearized Green-Lagrange strain tensor, which is obtained by neglecting in Equation 1.15 the term quadratic in $\vec{U}$. Hence we are left with the following expression for the linearized Green-Lagrange strains:

$$\overset{2}{\vec{e}} = e_{ij}\ \vec{g}^{\,i} \otimes \vec{g}^{\,j} = \frac{1}{2}(\vec{g}_i.\vec{U}_{,j} + \vec{g}_j.\vec{U}_{,i})\ \vec{g}^{\,i} \otimes \vec{g}^{\,j} \tag{1.16}$$

With the displacement assumptions given by Equation 1.14, we obtain the expression for the strains in terms of the displacement functions $\vec{u}$ and $\bar{\theta}$:

$$\begin{cases} e_{\alpha\beta} = \gamma_{\alpha\beta}(\vec{u}) + \xi^3\,\chi_{\alpha\beta}(\vec{u},\bar{\theta}) - (\xi^3)^2\,\delta_{\alpha\beta}(\bar{\theta}) \\ e_{\alpha 3} = \zeta_\alpha(\vec{u},\bar{\theta}) \\ e_{33} = 0 \end{cases} \tag{1.17}$$

$\overset{2}{\bar{\gamma}}$, $\overset{2}{\bar{\chi}}$, $\overset{2}{\bar{\delta}}$, and $\bar{\zeta}$ are all surface tensors.

Different components of the strain tensor The different components of the strain tensor can be expressed in terms of the displacements and of second and third fundamental forms of the mid-surface (denoted by $\overset{2}{\bar{b}}$ and $\overset{2}{\bar{c}}$ respectively).

$\overset{2}{\bar{\gamma}}$ is known as the membrane strain tensor. It is independent of the rotation vector $\bar{\theta}$:

$$\gamma_{\alpha\beta}(\vec{u}) = \frac{1}{2}(u_{\alpha|\beta} + u_{\beta|\alpha}) - b_{\alpha\beta}\,u_3 \tag{1.18}$$

$\overset{2-}{\chi}$ is known as the bending strain tensor. Its components can be expressed in terms of the displacement functions $\vec{u}$ and $\bar{\theta}$:

$$\chi_{\alpha\beta}(\vec{u}, \bar{\theta}) = \frac{1}{2}(\theta_{\alpha|\beta} + \theta_{\beta|\alpha} - b^{\lambda}_{\beta}\, u_{\lambda|\alpha} - b^{\lambda}_{\alpha}\, u_{\lambda|\beta}) + c_{\alpha\beta}\, u_3 \tag{1.19}$$

The tensor $\overset{2-}{\delta}$ does not bear a particular name. Its components can be expressed in terms of the displacement functions $\bar{\theta}$ only:

$$\delta_{\alpha\beta}(\bar{\theta}) = \frac{1}{2}(b^{\lambda}_{\beta}\, \theta_{\lambda|\alpha} + b^{\lambda}_{\alpha}\, \theta_{\lambda|\beta}) \tag{1.20}$$

Finally, $\bar{\zeta}$ is known as the transverse shear strain tensor (sometimes simply referred to as the shear strain tensor). Its components can be expressed in terms of the displacement functions $\vec{u}$ and $\bar{\theta}$:

$$\zeta_{\alpha}(\vec{u}, \bar{\theta}) = \frac{1}{2}(\theta_{\alpha} + u_{3,\alpha} + b^{\lambda}_{\alpha} u_{\lambda}) \tag{1.21}$$

From strains to stresses The stresses in the shell corresponding to a given state of strains are obtained by making use of the stress-strain law (in the absence of thermal effects and preconstraints):

$$\sigma^{ij} = H^{ijkl}\, e_{kl} \tag{1.22}$$

or

$$\overset{2\rightarrow}{\sigma} = \overset{4\rightarrow}{H} : \overset{2\rightarrow}{e} \tag{1.23}$$

In the case of an isotropic material, we have Hooke's law (in component notation):

$$H^{ijkl} = \lambda g^{ij} g^{kl} + \mu(g^{ik} g^{jl} + g^{il} g^{jk}) \tag{1.24}$$

or (in tensorial notation)

$$\overset{4\rightarrow}{H} = 3\lambda \overset{4\rightarrow}{K} + 2\mu \overset{4\rightarrow}{I} = 2\mu \overset{4\rightarrow}{J} + 3k \overset{4\rightarrow}{K} \tag{1.25}$$

where k is the compressibility modulus, given in terms of the Lamé constants by the expression:

$$3k = 3\lambda + 2\mu \tag{1.26}$$

i.e.

$$\overset{2\rightarrow}{\sigma} = \lambda Tr(\overset{2\rightarrow}{e}) \overset{2\rightarrow}{I} + 2\mu \overset{2\rightarrow}{e} \tag{1.27}$$

The Lamé constants are related to the Young's modulus E and Poisson ratio ν by:

$$\lambda = \frac{\nu E}{(1+\nu)(1-2\nu)} \tag{1.28}$$

$$\mu = \frac{E}{2(1+\nu)} \tag{1.29}$$

Taking now into account the fact that $\vec{g}^3$ is orthonormal to $\vec{g}^1$ and $\vec{g}^2$, and making the assumption that $\sigma^{33} = 0$, we finally arrive at the following stress strain relations:

$$\begin{cases} \sigma^{\alpha\beta} = C^{\alpha\beta\lambda\mu} e_{\lambda\mu} \\ \\ \sigma^{\alpha 3} = \frac{1}{2} D^{\alpha\lambda} e_{\lambda 3} \end{cases} \tag{1.30}$$

with

$$\begin{cases} \overset{4-}{C} = 2\mu \overset{4-}{I} + 3\frac{\nu E}{1-\nu^2} \overset{4-}{K} \\ \\ \overset{2-}{D} = 4\mu \overset{2-}{I} \end{cases} \tag{1.31}$$

Note the slight abuse of notation: $\overset{4-}{C}$ and $\overset{2-}{D}$ are not quite surface tensors in the sense that they are defined over Ω, not ω. We finally obtain the variational problem of

seeking a $\vec{U} \in \mathcal{V}$ that satisfies:

$$\int_\Omega C^{\alpha\beta\lambda\mu} e_{\alpha\beta}(\vec{U}) e_{\lambda\mu}(\vec{V}) + D^{\alpha\lambda} e_{\alpha 3}(\vec{U}) e_{\lambda 3}(\vec{V}) d\Omega = \int_\Omega \vec{F} \,.\, \vec{V} d\Omega \tag{1.32}$$

or in tensorial form

$$\int_\Omega \overset{2-}{e}(\vec{U}) \,:\, \overset{4-}{C} \,:\, \overset{2-}{e}(\vec{V}) + \bar{\zeta}(\vec{U}) \,.\, \overset{2-}{D} \,.\, \bar{\zeta}(\vec{V}) d\Omega = \int_\Omega \vec{F} \,.\, \vec{V}\, d\Omega \tag{1.33}$$

for any $\vec{V}$ of the same form as $\vec{U}$:

$$\vec{V}(\xi^1, \xi^2, \xi^3) = \vec{v}(\xi^1, \xi^2) + \xi^3 \eta_\lambda(\xi^1, \xi^2)\, \vec{a}_\lambda(\xi^1, \xi^2) \tag{1.34}$$

that vanishes at the points of the boundary where the displacements are prescribed. This problem can also be interpreted as a minimization problem:

$$\vec{U} = \arg \inf_{\vec{V} \in \mathcal{V}} \left\{ \frac{1}{2} \int_\Omega \overset{2-}{e}(\vec{V}) \,:\, \overset{4-}{C} \,:\, \overset{2-}{e}(\vec{V}) + \bar{\zeta}(\vec{V}) \,.\, \overset{2-}{D} \,.\, \bar{\zeta}(\vec{V}) d\Omega - \int_\Omega \vec{F} \,.\, \vec{V}\, d\Omega \right\} \tag{1.35}$$

i.e. the solution minimizes the functional [60]

$$\Pi = \frac{1}{2} \int_\Omega \overset{2-}{e}(\vec{V}) \,:\, \overset{4-}{C} \,:\, \overset{2-}{e}(\vec{V}) + \bar{\zeta}(\vec{V}) \,.\, \overset{2-}{D} \,.\, \bar{\zeta}(\vec{V}) d\Omega - \int_\Omega \vec{F} \,.\, \vec{V}\, d\Omega \tag{1.36}$$

1.2.3 Naghdi model

Note that this model is referred to by D. Chapelle and K.J. Bathe as the "shear-membrane-bending model" [22].

We now consider only the case where the loading applied is constant through the thickness (i.e. $\vec{F} = \vec{F}(\xi^1, \xi^2)$), which allows model dimension reduction. We also restrict our presentation to the case of constant thickness (the case of varying thickness can also be considered provided there exists a strictly positive lower bound on the thickness, see [22]). Having obtained the general variational problem given by Equation 1.33, the next step in the derivation of the Naghdi model consists in dropping

higher order terms in ξ^3 in the expressions of the strains (effectively neglecting the $\overset{2-}{\delta}$ tensor in Equation 1.17), stress strain law (effectively employing for all the points located on a line perpendicular to the mid-surface the stress strain law expressed at the intersection of that line with the mid-surface) and the volume measure (effectively employing for all the points located on a line perpendicular to the mid-surface the volume measure expressed at the intersection of that line with the mid-surface) and in then performing all the integrations with respect to ξ^3 in Equation 1.32. We then obtain [46]:

$$\int_\omega \underbrace{t^3 \tilde{C}^{\alpha\beta\lambda\mu} \chi_{\alpha\beta}(\vec{U}) \chi_{\lambda\mu}(\vec{V})}_{\substack{\text{bending} \\ \text{work} \\ \text{density}}} d\omega + \int_\omega \underbrace{t \tilde{C}^{\alpha\beta\lambda\mu} \gamma_{\alpha\beta}(\vec{u}) \gamma_{\lambda\mu}(\vec{v})}_{\substack{\text{membrane} \\ \text{work} \\ \text{density}}} + \underbrace{t \tilde{D}^{\alpha\lambda} \zeta_\alpha(\vec{U}) \zeta_\lambda(\vec{V})}_{\substack{\text{transverse shear} \\ \text{work} \\ \text{density}}} \; d\omega = t \int_\omega \vec{F} \cdot \vec{V} d\omega \tag{1.37}$$

where

$$\tilde{C}^{\alpha\beta\lambda\mu} = \frac{E}{2(1+\nu)} \left(a^{\alpha\lambda} a^{\beta\mu} + a^{\alpha\mu} a^{\beta\lambda} + \frac{2\nu}{1-\nu} a^{\alpha\beta} a^{\lambda\mu} \right) \tag{1.38}$$

and

$$\tilde{D}^{\alpha\lambda} = \frac{2E}{(1+\nu)} a^{\alpha\lambda} \tag{1.39}$$

Note that a shear correction factor $k \in \mathbb{R}_+^*$ is also sometimes included in the formulation so as to take into account the non-uniformity of the transverse strain field across the thickness of the shell (Considering an isotropic material, the transverse strains must vanish on the surfaces on the shell, since no tangent surface traction is applied to the shell). Ways to select a reasonable value for k are presented in [11, 57, 60]. Should we decide to include such a shear correction factor, we can modify the definition of the tensor $\overset{2-}{D}$ to take it into account. We can then naturally define the two bilinear operators $A_b^N(.,.)$ and $A_m^N(.,.)$ and the linear operator $G^N(.)$ such that Equation 1.37 reads:

$$\text{Find } U \in \mathcal{V}, \quad \epsilon^3 A_b^N(U,V) + \epsilon A_m^N(U,V) = G^N(V) \quad \forall V \in \mathcal{V} \tag{1.40}$$

with $\epsilon = t/L$ the relative thickness (L is a typical dimension of the shell). $A_b^N(.,.)$ accounts for the part of the strain energy associated with bending strains (often referred to as "bending energy": bending energy=$\epsilon^3 A_B(U,U)/2$) and $A_m^N(.,.)$ accounts for the part of the strain energy associated with transverse shear and the membrane strains (often referred to as the "transverse shear energy" and "membrane energy" respectively: transverse shear and membrane energy=$\epsilon A_m(U,U)/2)$).

1.2.4 Koiter shell model

This model is referred to by D. Chapelle and K.J. Bathe as the "membrane-bending model".

The model derived in Section 1.2.2 can be further simplified by making the following (restrictive) assumption, known as the Love-Kirchhoff kinematic assumption or the "hypothesis on the preservation of the normal element" [26, 43, 58, 44, 36, 27]: we still assume that the displacements of all points of Ω are governed by Equation 1.14, but instead of considering $\bar{\theta}$ and $\vec{u}$ as independent variables, we now tie them in the following way:

$$\theta_\lambda = -u_{3,\lambda} - b_\lambda^\mu u_\mu \tag{1.41}$$

It is seen that this assumption is the equivalent for shells of the Bernoulli assumption for beams (see, for instance, [23, 43]): any line orthogonal to the mid-surface in the undeformed configuration remains orthogonal to the mid-surface in the deformed configuration. As a result of this kinematic assumption, the transverse shear strains vanish (see Equation 1.21). Also, in the Koiter model (based on the Kirchhoff-Love kinematic assumption), the boundary conditions that can be imposed on a shell are more restricted than in the Naghdi model (based on the Reissner-Mindlin kinematic assumption), see [11].

Using the assumption 1.41 and Equation 1.19, we can express the bending components of the strain field in terms of the displacement $\vec{u}$ of the mid-surface only:

$$\chi_{\alpha\beta}(\vec{u},\bar{\theta}) = \rho_{\alpha\beta}(\vec{u}) = u_{3|\alpha\beta} + b_{\alpha|\beta}^\mu u_\mu + b_\alpha^\mu u_{\mu|\beta} + b_\beta^\mu u_{\mu|\alpha} - c_{\alpha\beta} u_3 \tag{1.42}$$

It can be shown that $\overset{2-}{\rho}$ is the tensor of linearized change of curvature of the mid-surface corresponding to the mid-surface displacement $\vec{u}$.

As a result, we can express the variational problem in terms of $\vec{u}$ only:

$$\int_\omega \underbrace{t^3 \tilde{C}^{\alpha\beta\lambda\mu} \rho_{\alpha\beta}(\vec{u}) \rho_{\lambda\mu}(\vec{v})}_{\substack{\text{bending} \\ \text{work} \\ \text{density}}} d\omega + \int_\omega \underbrace{t \tilde{C}^{\alpha\beta\lambda\mu} \gamma_{\alpha\beta}(\vec{u}) \gamma_{\lambda\mu}(\vec{v})}_{\substack{\text{membrane} \\ \text{work} \\ \text{density}}} d\omega = t \int_\omega \vec{F} \,.\, \vec{V} d\omega \qquad (1.43)$$

That the variational problem can be expressed in terms of $\vec{u}$ only implies that in the finite element discretization of the Koiter model only displacement degrees of freedom will need to be used whereas in the Naghdi model rotation degree of freedom will also be required. However, the presence of second derivatives of $\vec{u}$ in Equation 1.43 implies that in the Koiter shell model, we will need to seek solutions for u_3 with a more regular behavior (in a sense that will be explained in greater detail in Section 1.2.6) than in the Naghdi model (because Equation 1.37 involves only first derivatives of $\vec{u}$ and $\bar{\theta}$).

Just like in the Naghdi model, we can rewrite the problem in a compact form by defining the appropriate operators:

$$\text{Find } U \in \mathcal{V}, \quad \epsilon^3 A_b^K(U,V) + \epsilon A_m^K(U,V) = G^K(V) \quad \forall V \in \mathcal{V} \qquad (1.44)$$

1.2.5 Plate models

Having derived models suited for the analysis of shells, a natural next step is to specialize them to the case of plates. This is done by taking into account the fact that a plate is simply a flat shell. Hence we obtain plate models by simply dropping from the shell models terms that arise due to the curvature of the geometry under

consideration.

Reissner-Mindlin plate model For the Naghdi model, the strains of Equations 1.18, 1.19, 1.20 and 1.21 now simplify to the following expressions:

$$\begin{cases} \gamma_{\alpha\beta} = \frac{1}{2}(u_{\alpha|\beta} + u_{\beta|\alpha}) \\ \\ \chi_{\alpha\beta} = \frac{1}{2}(\theta_{\alpha|\beta} + \theta_{\beta|\alpha}) \\ \\ \delta_{\alpha\beta} = 0 \\ \\ \zeta_{\alpha} = \frac{1}{2}(\theta_{\alpha} + u_{3|\alpha}) \end{cases} \tag{1.45}$$

Of course, because of the absence of curvature, $u_{3|\alpha}$ can also be denoted $u_{3,\alpha}$.

An important result is that the in-plane problem for $\bar{u}= (u_1, u_2)$ now decouples from the out-of-plane problem for u_3 and $\bar{\theta}$. We now have the following two separate problems to solve:

$$\begin{cases} \int_\omega t\tilde{C}^{\alpha\beta\lambda\mu}\gamma_{\alpha\beta}(\bar{u})\gamma_{\gamma\mu}(\bar{v})d\omega = \int_\omega \bar{F} \,.\, \bar{v}\; d\omega \\ \\ \int_\omega \frac{t^3}{12}\tilde{C}^{\alpha\beta\lambda\mu}\chi_{\alpha\beta}(\bar{\theta})\chi_{\lambda\mu}(\bar{\eta})d\omega + \int_\omega t\tilde{D}^{\alpha\beta}\zeta_{\alpha}(u_3, \bar{\theta})\zeta_{\beta}(v_3, \bar{\eta})d\omega = \int_\omega tF_3v_3d\omega \end{cases} \tag{1.46}$$

The problem for $\bar{u}$ is known as the membrane problem, and the second problem in 1.46 is known as the Reissner-Mindlin plate problem.

Kirchhoff plate problem Under the assumptions of the Koiter model, the strains simplify further:

$$\begin{cases} \gamma_{\alpha\beta} = \frac{1}{2}(u_{\alpha|\beta} + u_{\beta|\alpha}) \\ \\ \rho_{\alpha\beta} = u_{3|\alpha\beta} \\ \\ \delta_{\alpha\beta} = 0 \\ \\ \zeta_{\alpha} = 0 \end{cases} \tag{1.47}$$

The problems to be solved are the following:

$$\begin{cases} \int_{\omega} t\tilde{C}^{\alpha\beta\lambda\mu}\gamma_{\alpha\beta}(\bar{u})\gamma_{\gamma\mu}(\bar{v})d\omega = \int_{\omega} \bar{F} \,.\, \bar{v} \; d\omega \\ \\ \int_{\omega} \frac{t^3}{12}\tilde{C}^{\alpha\beta\lambda\mu}\rho_{\alpha\beta}(u_3)\rho_{\lambda\mu}(v_3)d\omega = \int_{\omega} tF_3 v_3 d\omega \end{cases} \tag{1.48}$$

The first equation in 1.48, defining the membrane problem, is identical to that in the Naghdi plate model. The second equation in 1.48 is referred to as the Love-Kirchhoff plate model.

Very often, it is convenient to use an orthonormal parametrization of the mid-surface, so that the covariant differentiations in Equations 1.46 and 1.48 become regular differentiations. For particular geometries however, other parametrizations may be more appropriate (e.g. polar coordinates in the case of a disc-shaped plate).

1.2.6 Existence and uniqueness of a solution to the shell problems

Considering the problems introduced in Sections 1.2.3 and 1.2.4, the first important question is whether these problems admit a unique solution (for a given, finite thickness t) over some functional space $\mathcal{V}$ to be determined. Both problems are in the

form:

$$\text{Find } U \in \mathcal{V}, \quad \epsilon^3 A_b(U,V) + \epsilon A_m(U,V) = G(V) \quad \forall V \in \mathcal{V} \tag{1.49}$$

where the operators $A_b(.,.)$ and $A_m(.,.)$ differ from one model to the other. As a result, the mathematical problem 1.49 is well-posed on different functional spaces for the two models. We have the following results (see [22] for a proof) based directly on the Lax-Milgram theorem. In the following we denote the boundary conditions by $\mathcal{BC}$.

Naghdi shell model Provided $\vec{F} \in L^2(S)$, there exists a unique solution $(\vec{u}, \bar{\theta})$ in $\mathcal{V}^N = (H^1(S))^5 \cap \mathcal{BC}$

$$\exists! U = (\vec{u}, \bar{\theta}) \in \mathcal{V}^N, \quad \epsilon^3 A_b^N(U,V) + \epsilon A_m^N(U,V) = G^N(V) \quad \forall V = (\vec{v}, \bar{\eta}) \in \mathcal{V}^N \tag{1.50}$$

Also, the solution is continuous with respect to the loading, i.e.

$$||U||_{\mathcal{V}^N} \leq C|| \vec{F} ||_{L^2(S)} \tag{1.51}$$

Koiter shell model Provided $\vec{F} \in L^2(S)$, there exists a unique solution $\vec{u}$ in $\mathcal{V}^K = \{(H^1(S))^2 \times H^2(S)\} \cap \mathcal{BC}$

$$\exists!\, U = \vec{u} \in \mathcal{V}^K, \quad \epsilon^3 A_b^K(U,V) + \epsilon A_m^K(U,V) = G^K(V) \quad \forall V = (\vec{v}) \in \mathcal{V}^K \tag{1.52}$$

also, the solution is continuous with respect to the loading, i.e.

$$||U||_{\mathcal{V}^K} \leq C|| \vec{F} ||_{L^2(S)} \tag{1.53}$$

The important thing to note at this point is that, as was announced earlier, the regularity requirements on u_3 are stronger in the Koiter model than in the Reissner-Mindlin model ($u_3 \in H^2(S)$ instead of $u_3 \in H^1(S)$).

Chapter 2

Shell asymptotic behaviors and layers

Having introduced the basic mathematical model employed in shell analysis in Chapter 1, we open this chapter with a discussion of the asymptotic behavior of shells when their thickness is reduced to zero. Of particular interest for our study is the presence of boundary and internal layers in the solution of shell problems. In Section 2.2, we introduce these local phenomena and explain their presence from a mathematical and physical standpoint. Finally, we illustrate this discussion with the results of numerical simulations that feature typical boundary and internal layers.

2.1 Asymptotic behaviors of shells

Here we first summarize in Section 2.1.1 general asymptotic analysis results given in References [22, 19], and then in Section 2.1.2 we illustrate our discussion with a simple beam example.

2.1.1 General presentation

The study of the asymptotic behavior of shells ([54, 55]) as their thickness is reduced to zero is not only an exercise of scholarly interest. It also sheds light on some behaviors

that are specific to shell finite element structures, and from a practical standpoint it helps understand why certain finite element formulations perform poorly (i.e. they display a "locking" behavior, see Section 3.1.3) when the thickness of the shell is decreased.

Space of inextensional displacements The behavior of a shell as its thickness goes to zero ($t \rightarrow 0$), with the loading being scaled accordingly to ensure that the solution remains bounded, is highly dependent on the following subspace $\mathcal{U}_0$

$$\mathcal{U}_0 = \{ V \in \mathcal{V}, \ A_m(V,V) = 0 \} \tag{2.1}$$

Since the bilinear operator $A_m(.,.)$ accounts for the transverse shear and membrane energy, the space $\mathcal{U}_0$ is called the space of pure bending displacements. Displacements in this space have the particularity that they leave the length of curves drawn on the mid-surface unchanged. This is why this space is also called the space of inextensional displacements. When $\mathcal{U}_0 = \{0\}$, the problem is termed an "inhibited pure bending problem" because there exists no non-trivial admissible displacement field that yields bending energy only. Otherwise, the problem is described as "non-inhibited pure bending problem". It should be noted that $\mathcal{U}_0$ is determined by the geometry of the problem and the boundary conditions, but not by the loading applied.

For special geometries, it is sometimes possible to determine the content of the space $\mathcal{U}_0$ based on the property that displacements in this space leave the length of curves drawn on the mid-surface unchanged. For instance, considering the problem of a cylinder clamped at both ends, it is immediately seen that for this problem, we have $\mathcal{U}_0 = \{0\}$.

In general, to determine the content of $\mathcal{U}_0$ we need to solve Equation 2.1, which is equivalent to

$$\gamma_{\alpha\beta}(\vec{u}) = \frac{1}{2}(u_{\alpha|\beta} + u_{\beta|\alpha}) - b_{\alpha\beta}\, u_3 = 0 \tag{2.2}$$

at all points (and of course the boundary conditions must be satisfied). We should also point out – and this is particularly clear in the form 2.2 – that the definition of the space of inextensional displacements is independent of rotations (in the Reissner-Mindlin formulation).

Looking at Equation 1.40, it is clear that in general if we do not scale the loading as $\epsilon \equiv t/L \rightarrow 0$, the solution of the problem will not remain unbounded (This is also intuitively obvious). That same equation shows that the part of the stiffness of the structure due to bending is proportional to the third power of ϵ, whereas the stiffness due to the shear and membrane energy is proportional to the first power of ϵ. This implies that for thin shells, the bending energy is in general relatively small compared to the membrane and transverse shear energy, so that if inextensional displacements (displacements that involve bending but no membrane and transverse shearing action) are admissible (i.e. if $\mathcal{U}_0 \neq \{0\}$) and excited by the loading, then the structure will tend to favor these displacement modes because of Equation 1.36 [39]. This qualitative analysis can be presented more formally as follows.

Inhibited pure bending case In the case where $\mathcal{U}_0 = \{0\}$, for the solution to Equation 1.40 to remain bounded as $\epsilon \rightarrow 0$, we need to use the following scaling for the loading:

$$G(V) = \epsilon F_m(V) \tag{2.3}$$

This reflects the fact that since pure bending is not allowed by the structure, the stiffness of the structure is proportional to ϵ.

Equation 1.40 can then be rewritten:

$$\text{Find } U^\epsilon \in \mathcal{V}, \quad \epsilon^2 A_b(U^\epsilon, V) + A_m(U^\epsilon, V) = F_m(V) \quad \forall V \in \mathcal{V} \tag{2.4}$$

This problem is a perturbed version of

$$\text{Find } U_0^m \in \mathcal{V}_m \quad A_m(U_0^m, V) = F_m(V) \quad \forall V \in \mathcal{V}_m \tag{2.5}$$

where the space $\mathcal{V}_m$ is defined by

$$V \in \mathcal{V}_m \Longleftrightarrow A_m(V,V) < \infty \tag{2.6}$$

In other words, $\mathcal{V}_m$ is the completion of $\mathcal{V}$ with respect to $A_m(.,.)$ (see [30]) which is a norm in bending inhibited cases. Note that the space $\mathcal{V}_m$ is larger than $\mathcal{V}$ because only the regularity conditions arising from the definition of the membrane part of the strain energy need be satisfied. In particular the derivatives of the normal displacement do not appear in the expressions of the membrane strains for instance. This implies that, roughly speaking, whereas the space $\mathcal{V}$ is $H^1(\omega) \times H^1(\omega) \times H^2(\omega) \cap \mathcal{BC}$ (in the Koiter model), the space $\mathcal{V}_m$ is the completion of $H^1(\omega) \times H^1(\omega) \times L^2(\omega) \cap \mathcal{BC}$ (and possibly even larger depending on the geometry). Since the normal displacements are only constrained to be in $L^2(\omega)$, the boundary conditions on these normal displacements are meaningless (the trace of a function of class $L^2(\omega)$ is meaningless).

Whether the perturbation introduced by the bending term affects the solution significantly is determined by the so-called "membrane condition":

$$\exists c \in \mathbb{R}, \quad F_m(V)^2 \leq c A_m(V,V) \quad \forall V \in \mathcal{V}_m \tag{2.7}$$

This is a condition that involves not only the geometry of the problem, but also the loading applied. It is equivalent to the condition

$$F_m \in \mathcal{V}_m{}' \tag{2.8}$$

Because the space $\mathcal{V}_m$ is larger than $\mathcal{V}$, its dual $\mathcal{V}_m{}'$ is smaller than $\mathcal{V}'$. If condition 2.7 is satisfied, then the solution of 2.4 converges strongly in the sense of the norm $A_m(.,.)$ to the solution of Equation 2.5 as $\epsilon \to 0$ ($A_m(.,.)$ is a norm for $\mathcal{V}_m$ because $\mathcal{U}_0 = \{0\}$) and we have:

$$\lim_{\epsilon \to 0} \frac{1}{2} \epsilon^2 A_b(U^\epsilon, U^\epsilon) = 0 \tag{2.9}$$

These results mean that for a bending-inhibited problem, as the thickness is decreased to zero and a loading satisfying the membrane condition is re-scaled according to Equation 2.3, the problem remains well-posed and in its solution the bending strain energy becomes negligible compared to the membrane and shear energy. For this reason, such problems are called membrane-dominated problems. Note that because the solution U_o^m of the limit problem is only guaranteed to be in $\mathcal{V}_m$ and not in $\mathcal{V}$, for very small thicknesses the solution may be ill-behaved [53, 49], see Section 2.2. If condition 2.7 is not satisfied – which is fairly possible considering that $\mathcal{V}_m{}'$ is small, the solution of the limit problem is not in the space $\mathcal{V}_m$ and if we use the scaling factor $\rho = 1$, we observe that the scaled energy

$$A_m(U^\epsilon, U^\epsilon) + \epsilon^2 A_b(U^\epsilon, U^\epsilon) \tag{2.10}$$

does not remain bounded as the thickness t is reduced to zero. At finite thicknesses, the solution of the shell problem corresponds to a mixed[1] state where neither the bending strain energy nor the membrane strain energy dominates and boundary and internal layers are usually present [53]. In this case, the ratio of the bending energy to the total strain energy may or may not tend to a constant as t goes to zero, as demonstrated by numerical studies [40, 5]. Dropping the scaling of the loading, if we assume that the strain energy varies as a power of the thickness:

$$\epsilon^\alpha E(\epsilon) \to \lambda \tag{2.11}$$

where $E(\epsilon) \equiv E(U^\epsilon, U^\epsilon)$ denotes the strain energy

$$E(\epsilon) = \frac{1}{2}(\epsilon A_m(U^\epsilon, U^\epsilon) + \epsilon^3 A_b(U^\epsilon, U^\epsilon)) \tag{2.12}$$

and we also assume that the fraction of the bending to the strain energy

$$R(\epsilon) = \frac{\frac{1}{2}\epsilon^3 A_b(U^\epsilon, U^\epsilon)}{E(\epsilon)} \tag{2.13}$$

[1]Mixed state are also sometimes referred to as intermediate states

goes to a limit

$$\exists \mu \in \mathbb{R} \text{ such that } R(\epsilon) \rightarrow \mu \text{ as } \epsilon \rightarrow 0 \tag{2.14}$$

Then it has been established recently [42, 2] that

$$\mu = \frac{\alpha - 1}{2} \tag{2.15}$$

Non-inhibited pure bending case In the case $\mathcal{U}_0 \neq \{0\}$, for the solution of Equation 1.40 to remain bounded as $\epsilon \rightarrow 0$, we need to use the following scaling for the loading:

$$G(V) = \epsilon^3 F_b(V) \tag{2.16}$$

This statement reflects the fact that since pure bending is possible, the stiffness of the structure is proportional to t^3.

Equation 1.40 can then be rewritten:

$$\text{Find } U^\epsilon \in \mathcal{V}, \quad A_b(U^\epsilon, V) + \tfrac{1}{\epsilon^2} A_m(U^\epsilon, V) = F_b(V) \quad \forall V \in \mathcal{V} \tag{2.17}$$

If the loading excites the inextensional admissible displacements, i.e. if

$$\exists V \in \mathcal{U}_0, \quad F(V) \neq 0 \tag{2.18}$$

then in the limit $\epsilon \rightarrow 0$, this problem is equivalent to

$$\text{Find } U_0^b \in \mathcal{U}_0 \quad A_b(U_0^b, V) = F_b(V) \quad \forall V \in \mathcal{U}_0 \tag{2.19}$$

where the constraint $U_0^b \in \mathcal{U}_0$ is imposed in 2.17 by a penalty method [11]. We then have

$$\lim_{\epsilon \rightarrow 0} \frac{1}{2\epsilon^2} A_m(U^\epsilon, U^\epsilon) = 0 \tag{2.20}$$

These results mean that for a non-inhibited problem, as the thickness is decreased to zero and the loading is re-scaled according to Equation 2.16, the problem remains well-

posed and in its solution the transverse shear and membrane strain energy become negligible compared to the bending strain energy. For this reason, such problems are called bending-dominated problems and the limit solution is an inextensional state.

If the loading does not excite the inextensional admissible displacements (i.e. Equation 2.18 is not satisfied), two behaviors are possible, both unstable. Defining

$$\mathcal{U}_c = \{U \in \mathcal{V} / \; A_b(U,V) = 0 \; \forall V \in \mathcal{U}_0\} = \{U / \; E(U,V) = 0 \; \forall V \in \mathcal{U}_0\} \tag{2.21}$$

and denoting $\mathcal{V}_m$ the completion[2] of $\mathcal{U}_c$ for $A_m(.,.)$ (which is consistent with and generalizes the previous definition of $\mathcal{V}_m$), if the membrane condition

$$\exists c \in \mathbb{R}, \quad F_m(V)^2 \leq c A_m(V,V) \quad \forall V \in \mathcal{V}_m \tag{2.22}$$

is satisfied, then the asymptotic behavior is a membrane-dominated one. If Equation 2.22 is not satisfied, then the asymptotic behavior is a mixed one. In either case, this situation can be described as "unstable" in the sense that if a small perturbation is added to the loading and excites the pure-bending modes then the problem reverses to a bending-dominated state, see References [22, 19] where also examples are given.

Summary of asymptotic behaviors The previous results on asymptotic behaviors are summarized in a mathematical setting in Figure 2-1 and more informally in Figure 2-2, as reported in [22].

It should be noted that which model (Kirchhoff-Love model or Koiter model) is used in the analysis does not influence the asymptotic behavior of the shell since the transverse shear strain energy vanishes in the limit of zero-thickness in all cases.

[2]Note that this is possible because A_m indeed defines a norm on $\mathcal{V}_c$ (see [30])

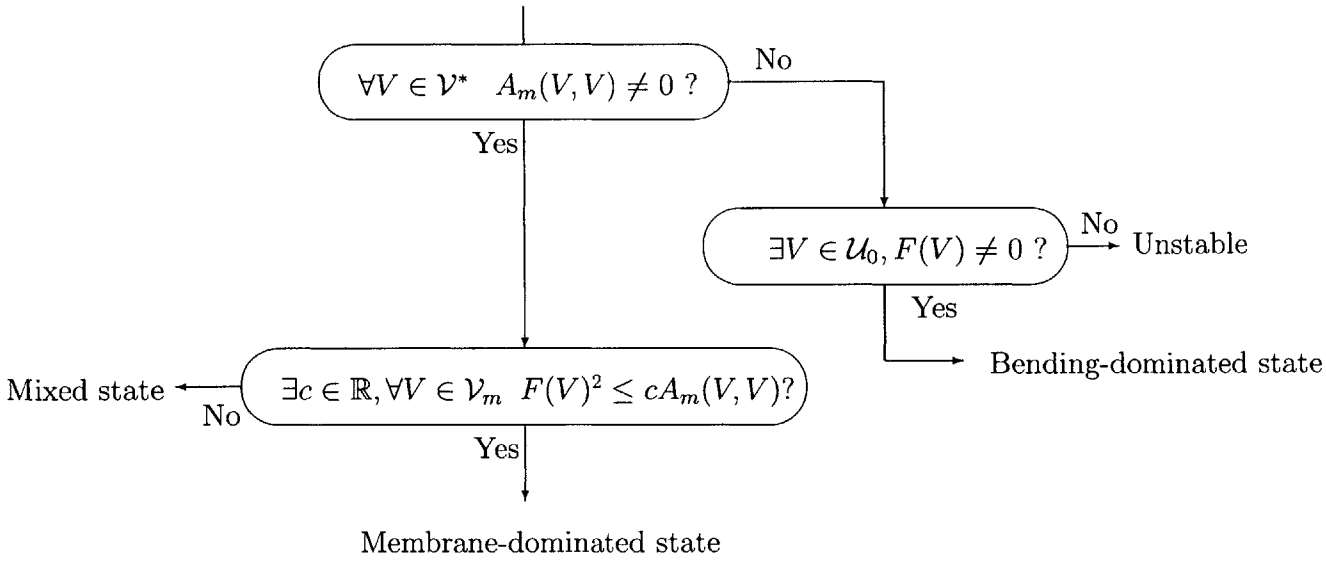

Figure 2-1: Asymptotic behaviors of shells (I), see Reference [22].

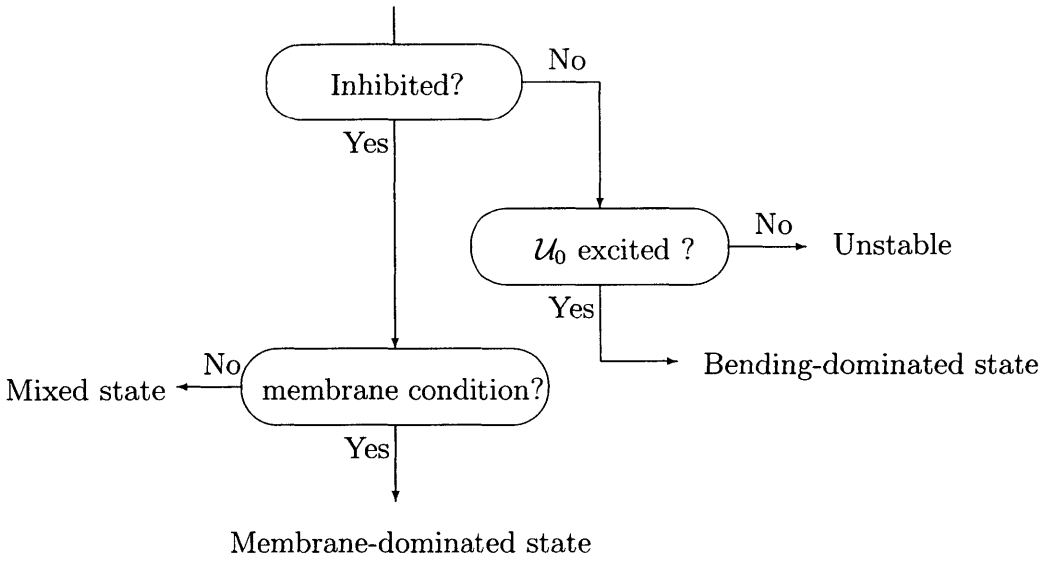

Figure 2-2: Asymptotic behaviors of shells (II), see Reference [22].

2.1.2 Asymptotic behaviors: an illustration

In this section we present the asymptotic analysis of a straight beam. Although the mathematical model employed for this structure is much simpler than either of the models presented for general shell structures it is characterized by somewhat similar asymptotic behaviors and therefore helps gain a better understanding of the limit behaviors discussed in Section 2.1 and summarized in the tables therein.

We consider a straight beam (say, of rectangular cross section with thickness t and width b) clamped at one end and loaded by a tip load with axial component T and a normal component F. We employ the classical Bernoulli (Kirschoff) beam model, so that the axial displacement $u_1(x)$ and normal displacement $u_2(x)$ of a particle located at the coordinate x along the beam are governed by the differential equations

$$\frac{d}{dx}(btE\frac{du_1}{dx}) = 0 \tag{2.23}$$

and

$$\frac{d^2}{d^2x}(bt^3E/12\frac{d^2u_2}{dx^2}) = 0 \tag{2.24}$$

In functional form, we can write

$$\epsilon^3 A_b(\underline{U},\underline{V}) + \epsilon A_m(\underline{U},\underline{V}) = F(\underline{V}) \tag{2.25}$$

where the similarity with the shell problem 1.49 is clear, but of course we now use the definitions

$$A_m(\underline{U},\underline{V}) = \frac{t}{\epsilon}\int_0^L bE\frac{du_1}{dx}\frac{dv_1}{dx}dx \tag{2.26}$$

$$A_b(\underline{U},\underline{V}) = \frac{t^3}{\epsilon^3}\int_0^L bE/12\frac{d^2u_2}{dx^2}\frac{d^2v_2}{dx^2}dx \tag{2.27}$$

which are essentially simplifications of the corresponding shell functionals for a ξ_2-independent problem and

$$F(\underline{U}) = Tu_1(L) + Fu_2(L) \tag{2.28}$$

It is easy to check that the membrane energy of the solution is $T^2L/(2Etb)$ and the bending energy is $2F^2L^3/(Et^3b)$. This is an example of a structure where $\mathcal{U}_0 \neq \{0\}$, but the loading T by itself does not excite the bending modes. Hence, under T alone, the behavior is a membrane-dominated one (in fact a "membrane-only" one), and the proper scaling of the loading is $\rho = 1$. But if we perturb T with $F \ll T$, the behavior becomes bending-dominated as the thickness goes to zero.

2.2 Boundary and internal layers

In this section, we first show on a practical example how boundary and internal layers can be present in the analysis of thin shells and then discuss the fundamental cause of this phenomenon. Finally we review where these layers can be expected to appear.

2.2.1 Typical case

We consider the Scordelis-Lo problem in which a cylindrical roof supported by membranes is submitted to a surface load. The geometry of the problem is recalled on Figure 2-3. Following the traditional definition of this standard test, the characteristic dimensions of the problem are $R = L = 25$ and $\epsilon = t/R = 10^{-5}$, the Young modulus is $4.32 \, . \, 10^8$ and the Poisson ratio 0. The surface loading has a magnitude of 90 per unit area. This problem has been proven to fall in the category of asymptotic mixed state problems (see [22, 20]) and this result has been verified through numerical experiments (see [2, 40]). In Figure 2-4, the results of a numerical simulation show that the displacements along the free edges of the roof are the only ones that are of significant magnitude.

2.2.2 Origin of boundary and internal layers

We have mentioned already the importance of the space of inextensional displacements $\mathcal{U}_0$ in the asymptotic behavior of shells. Here we will see how this space is related to the presence of boundary and internal layers. Let us recall that we defined

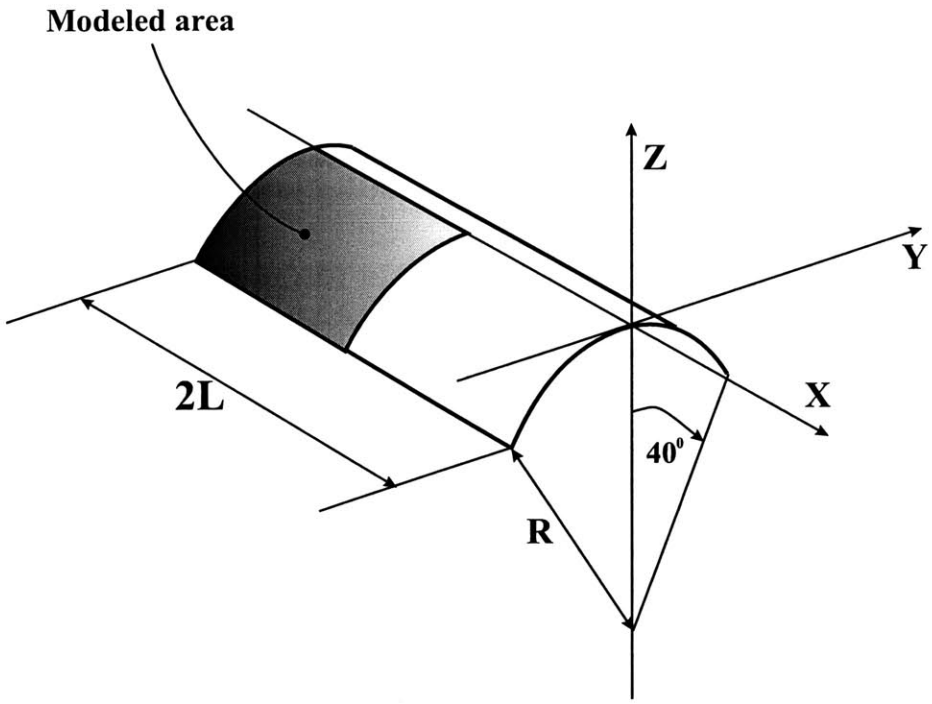

Figure 2-3: Scordelis-Lo roof: problem definition.

$\mathcal{U}_c$ by

$$\mathcal{U}_c = \{U \in \mathcal{V} / \; A_b(U,V) = 0 \quad \forall V \in \mathcal{U}_0\} = \{U \in \mathcal{V} / \; E(U,V) = 0 \quad \forall V \in \mathcal{U}_0\} \quad (2.29)$$

and we defined $\mathcal{V}_m$ as the completion of $\mathcal{U}_c$ for A_m. The space $\mathcal{V}_m$ is in general larger than the space $\mathcal{V}$. For instance, the membrane strains, which are the only strains that appear in the norm A_m, do not feature derivatives of u_3 and therefore $\mathcal{V}_m$ only requires $L^2(\omega)$ regularity for the displacements normal to the shell mid-surface. This implies that the dual space $\mathcal{V}'_m$ is in general smaller than $\mathcal{V}'$. Hence there may be loadings $F \in \mathcal{V}'$ that do not belong to $\mathcal{V}'_m$. If such a loading is used, it is admissible for the finite-thickness problem but it is not admissible for the limit problem (problem at $t = 0$). The solution to the limit problem in this case does not have the regularity of the finite-thickness problem, and can have discontinuities, distributional singularities, etc. For instance, any boundary condition on u_3 becomes meaningless as u_3 is now

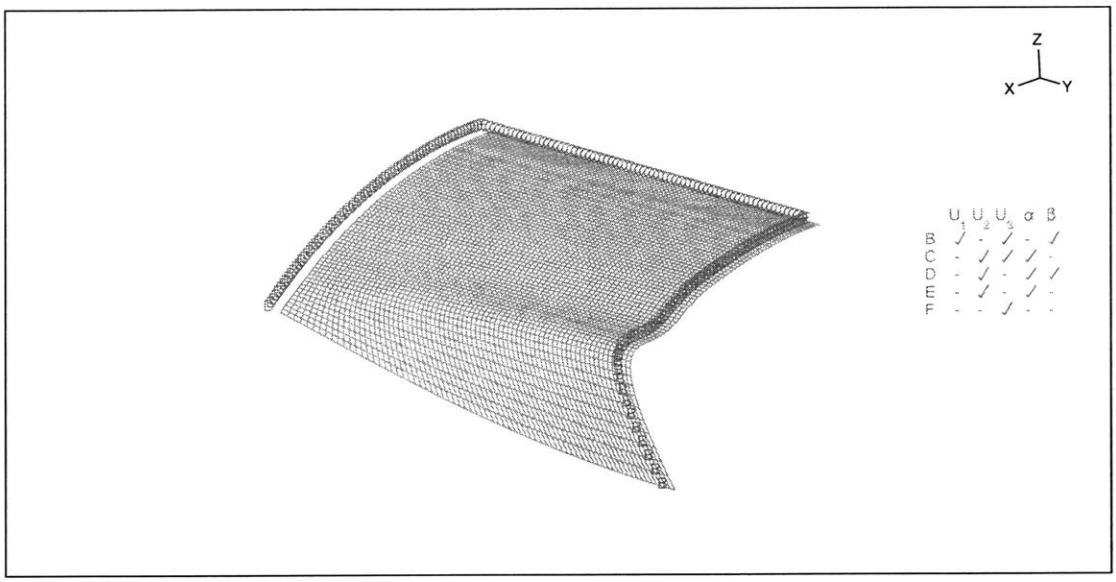

Figure 2-4: Scordelis-Lo roof: deformation of the mid-surface. Due to the symmetries, only one quarter of the structure is modelled (symmetry boundary conditions are indicated). A very fine 72x72 MITC4 mesh is used. Displacements are seen to decrease rapidly away from the free edge.

only guaranteed to be in $L^2(\omega)$ and the trace of such functions is irrelevant (see [22, 30]). At very small thicknesses, the loading is admissible and the solution is regular but the smaller the thickness becomes and the more irregular the solution gets, eventually losing regularity when $t = 0$. This explains why the phenomenon of boundary and internal layers becomes more and more evident as the thickness of a structure is reduced: as the thickness is reduced the typical width of the layers decreases while their magnitude increases.

Going back to the Scordelis-Lo roof problem of the previous section, it is clear that $\mathcal{U}_0 = \{0\}$. It can be shown [22, 56] that due to the fact that the loading does not vanish on the free edge it does not belong to $\mathcal{V}'_m$ and this is the fundamental cause why a boundary layer appears on that free edge when a small thickness is considered. The limit problem is a mixed state one. Indeed it is observed in numerical simulations that when a smooth loading that vanishes on the free edges is used in place of the uniform surface loading of the original Scordelis-Lo problem the solution does not

present a layer and that indeed we then have a membrane-dominated limit problem [40].

2.2.3 Location of boundary and internal layers and characteristic length scales

The location of boundary and internal layers has been studied and reported on in [56]. The following locations are prone to feature layers:

- Along the boundaries of the structures, both unconstrained ('free') edges and boundaries where essential boundary conditions are imposed.
- Along discontinuities of the loading.
- Along the curves where either the tangent plane or curvatures are discontinuous.
- Along characteristics issued from singular points of the geometry or loading.
- Along characteristics that are tangent to the four types of curves above.

We give examples in each case in the following section. The characteristic thickness δ of the boundary and internal layers has also been established theoretically and depends on the local geometry [47, 48, 56], as listed in Table 2.1.

2.2.4 Simulation results featuring boundary and internal layers

In this section, we present the results of numerical calculations that illustrate the presence of boundary and internal layers in thin shells. In all figures in this section, displacements are magnified so as to be clearly noticeable.

Along the boundaries of the structure The Scordelis-Lo roof problem of Section 2.2.1 illustrates this case.

Table 2.1: Characteristic width of layers. ϵ is the ratio of the thickness to a characteristic length scale L of the geometry: $\epsilon = t/L$. Since we are interested in the case $\epsilon << 1$, as ϵ is reduced the width of a boundary or internal layer decreases with t the slowest when the layer corresponds to a ruling at a parabolic point, and it decreases with t the fastest when the layer is not located along a ruling.

Characteristic width	Location
$\delta \propto \epsilon^{1/2}$	Along curves that are not characteristics
$\delta \propto \epsilon^{1/3}$	Along characteristics (rulings) in the case of a hyperbolic geometry
$\delta \propto \epsilon^{1/4}$	Along characteristics (rulings) in the case of a parabolic geometry

Along characteristics issued from singular points of the geometry or loading

- We consider the cylinder with equation

$$\begin{cases} x^2 + y^2 = 1 \\ |z| \leq 2 \end{cases} \tag{2.30}$$

loaded over the part of the mid-surface defined by the inequalities

$$\begin{cases} |x| \leq 0.3 \\ y \geq 0 \\ |z| \leq 0.6 \end{cases} \tag{2.31}$$

by a uniform force per unit area in the y direction. The geometry and loaded region are shown on Figure 2.2.4.

The solution presented in Figure 2-6 shows internal layers along each of the rulings originating from the singular points of the loading.

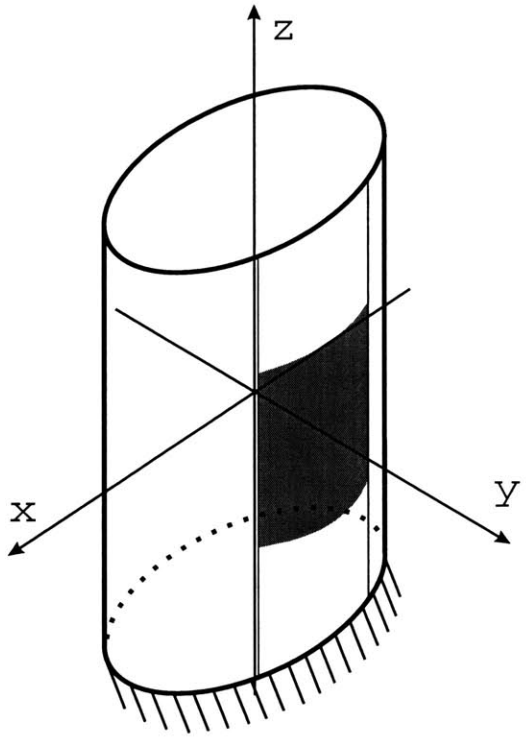

Figure 2-5: Cylinder of revolution: original geometry, loaded region and boundary conditions. The loaded region is shaded.

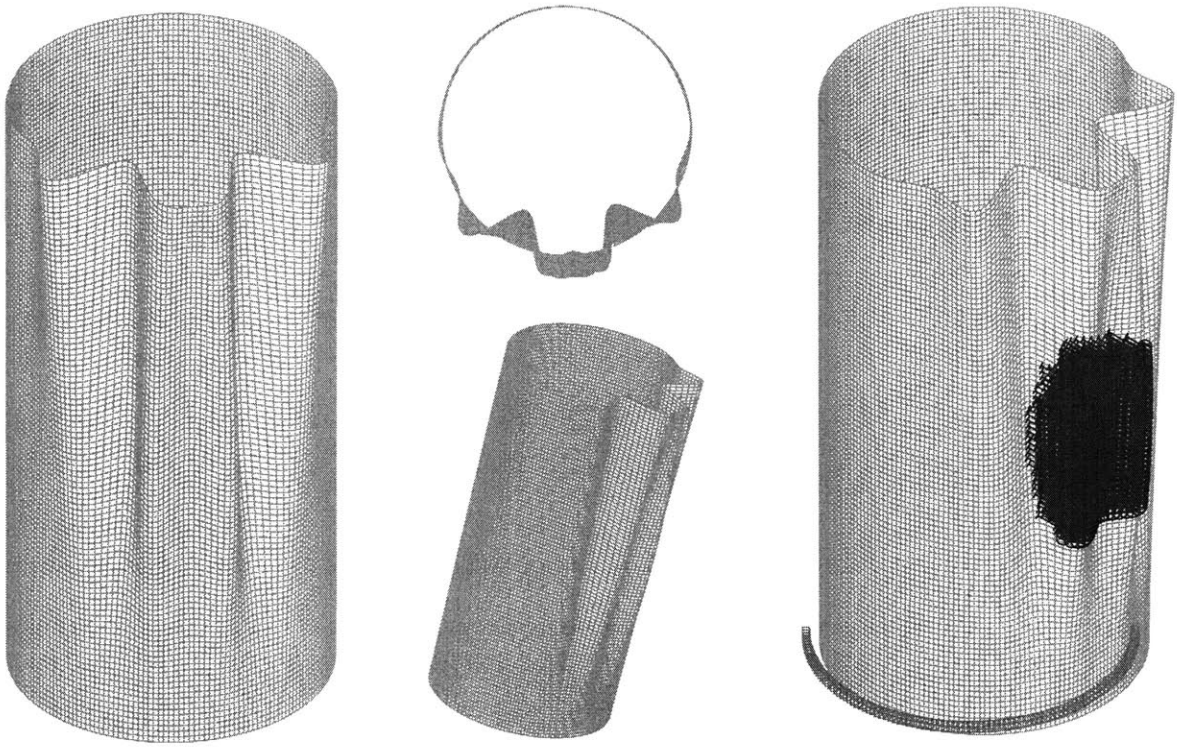

Figure 2-6: Cylinder of revolution: deformation of the mid-surface. A 200x100 MITC4 mesh is used. On the view on the right-hand side, the loading and boundary conditions are represented. Displacements are seen to decrease rapidly away from the ruling issued from each singular point of the loading.

- We consider the problem of a hyperboloid of one sheet loaded along one quarter of its top and clamped at its based, as shown in Figure 2-7. The equation of the hyperboloid is

$$\begin{cases} \frac{x^2}{a^2} + \frac{y^2}{b^2} = 1 + \frac{z^2}{c^2} \\ |z| \leq h/2 \end{cases} \tag{2.32}$$

A hyperboloid of one sheet is a doubly-ruled surface, as shown in Figure 2-7. A cooling tower is a typical example of the practical use of this shape. For our numerical tests we consider a thickness of $t = 10^{-4}$ and the values $a^2 = b^2 = 5$, $c^2 = 9$, and $h = 12$ and a loading of magnitude one per unit length. The resulting displacements, presented in Figure 2-8 show internal layers along the rulings issued form the singular points of the loading. The four internal layers are seen to interact in two points.

- We consider the elliptic hyperboloid of equation

$$\begin{cases} \frac{x^2}{a^2} + \frac{y^2}{b^2} = 1 + \frac{z^2}{c^2} \\ |z| \leq h/2 \end{cases} \tag{2.33}$$

with the parameters $a^2 = 30$, $b^2 = 10$, $c^2 = 64$ and $h = 40$. The elliptic hyperboloid is clamped along its bottom edge, and its thickness is $t = 10^{-4}$. A loading of magnitude one per unit area is applied in the y direction over the 'rectangular' area of the elliptic hyperboloid that satisfies the inequalities

$$\begin{cases} |x| \leq 2 \\ |z| \leq 6 \\ y \geq 0 \end{cases} \tag{2.34}$$

The elliptic hyperboloid, the area where the loading is applied and the rulings issued from the singular points of the loading are shown in Figure 2-9. Figure 2.2.4 shows the displacements obtained using a fine mesh. In particular it should be noted that internal layers are present along the rulings issued from the singular points of the loading.

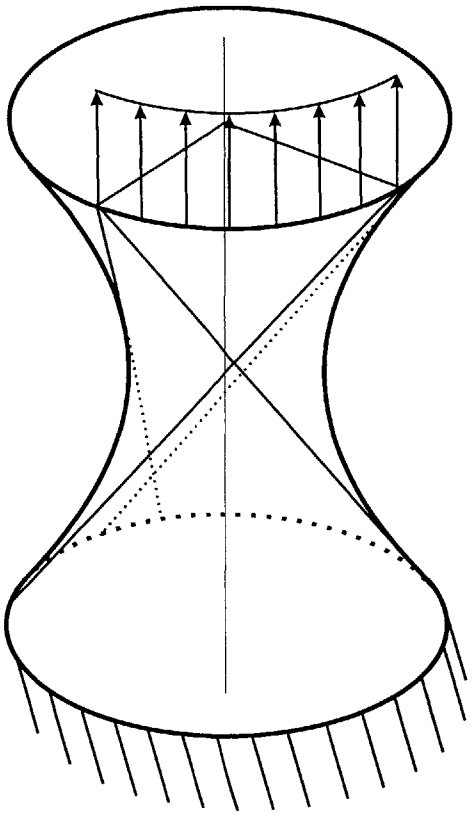

Figure 2-7: Hyperboloid of one sheet: geometry, loading and boundary conditions. The rulings originating from the two end-points of the loading are indicated.

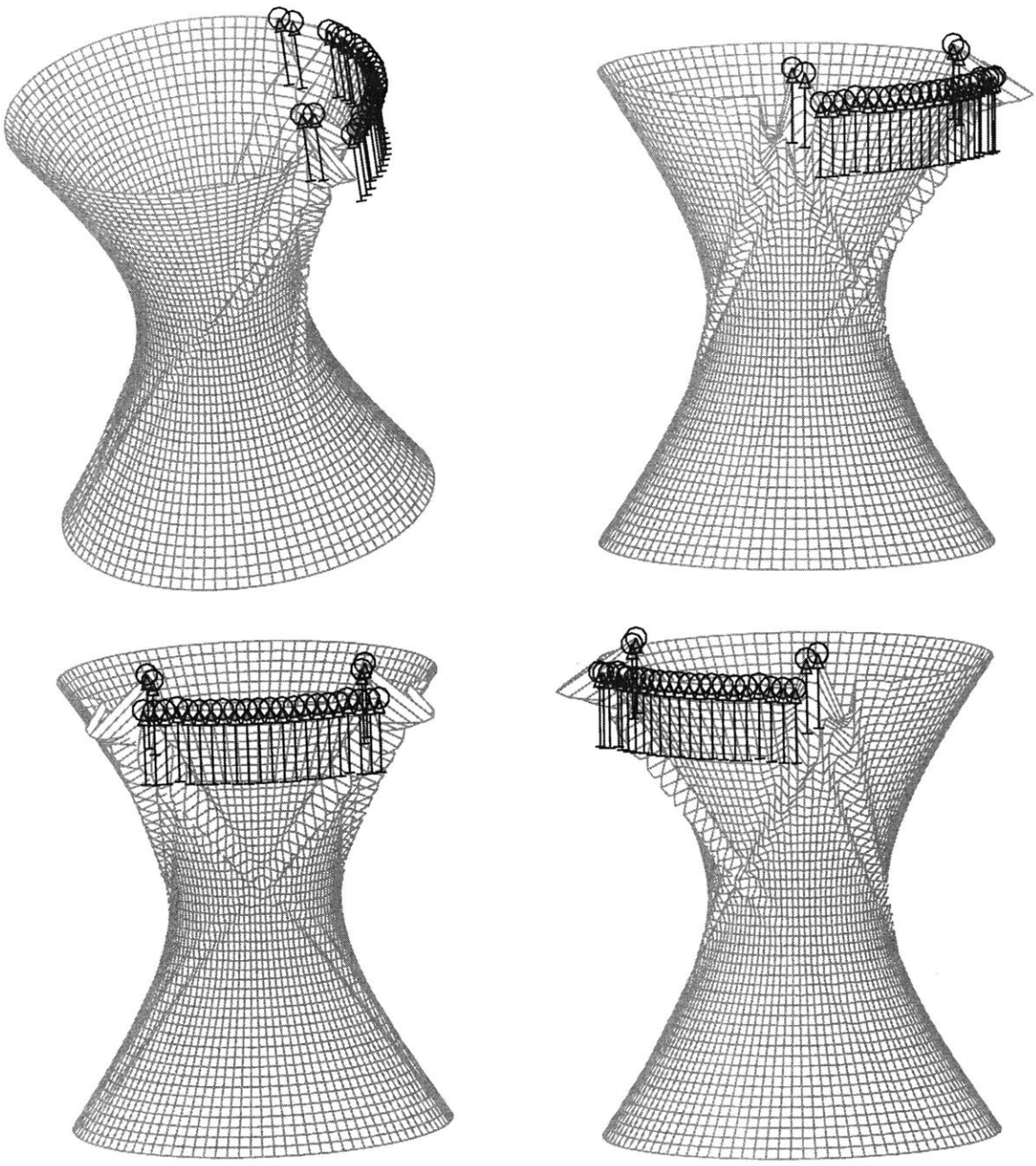

Figure 2-8: Hyperboloid of one sheet: deformation of the mid-surface seen from four different angles. A 100x50 MITC4 mesh is used. Displacements are seen to decrease rapidly away from the rulings issued from the singular points of the loading.

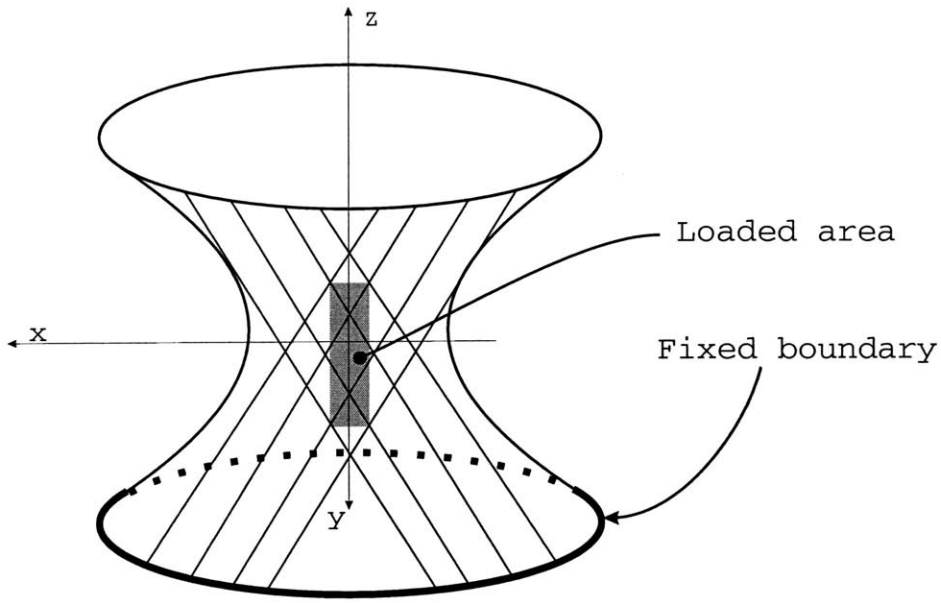

Figure 2-9: Elliptic hyperboloid of one sheet: geometry, loading area and rulings

- We consider the inverted "funnel" shape defined by the equations

$$\begin{cases} x^2 + y^2 = (3 - z)^2 \\ -6 < z < 0 \end{cases} \tag{2.35}$$

and

$$\begin{cases} x^2 + y^2 = 9 \\ 0 < z < 6 \end{cases} \tag{2.36}$$

The thickness is $t = 10^{-4}$. A loading of magnitude one per unit area and of direction x is applied over the part of the mid-surface with equation

$$\begin{cases} |\theta| < \pi/8 \\ -4 < z < -2 \end{cases} \tag{2.37}$$

where θ is the polar angle about the z direction. The funnel is clamped along the edge corresponding to $z = -6$. The results of the numerical simulation are presented in Figures 2-12 through 2-15 . The mesh employed is a non-uniform

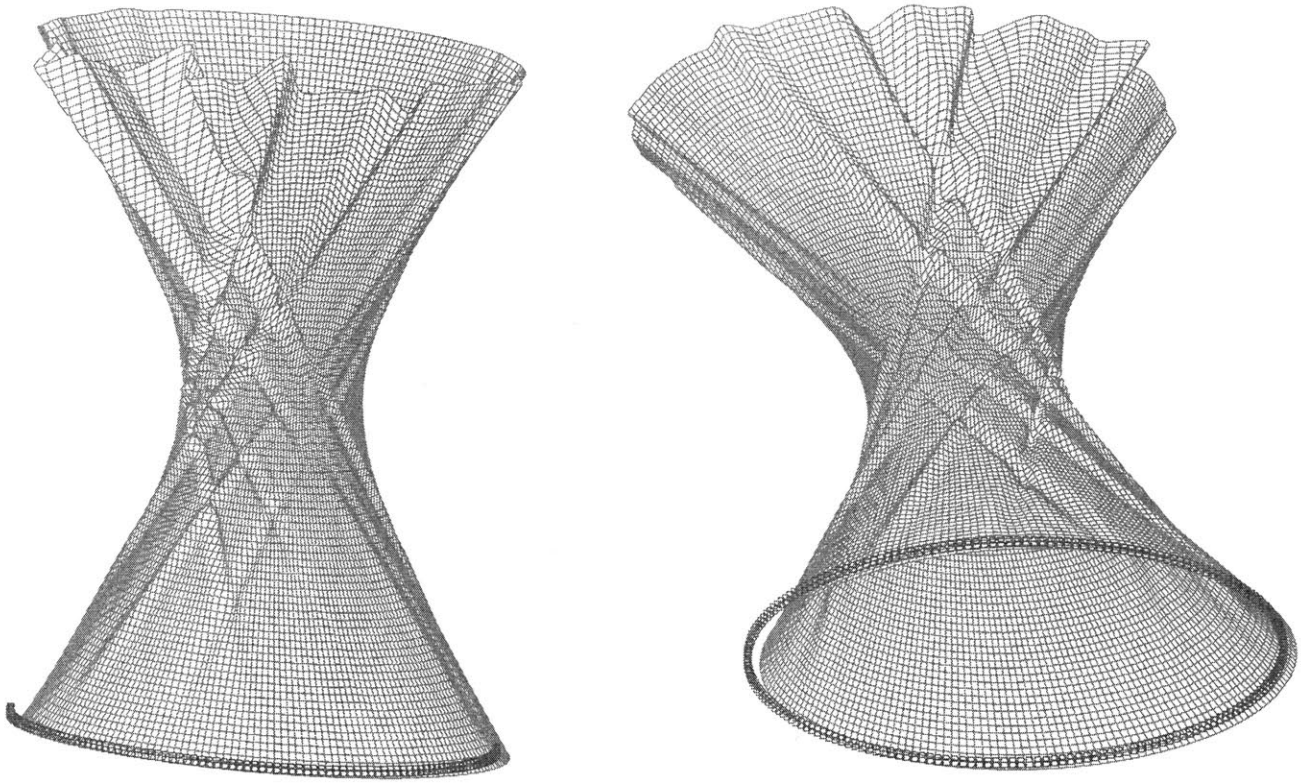

Figure 2-10: Elliptic Hyperboloid of one sheet: deformation of the mid-surface. The clamped boundary condition is indicated. A 200x100 MITC4 mesh is used. Displacements are seen to decrease rapidly away from the 2 rulings issued from each of the four singular points of the loading.

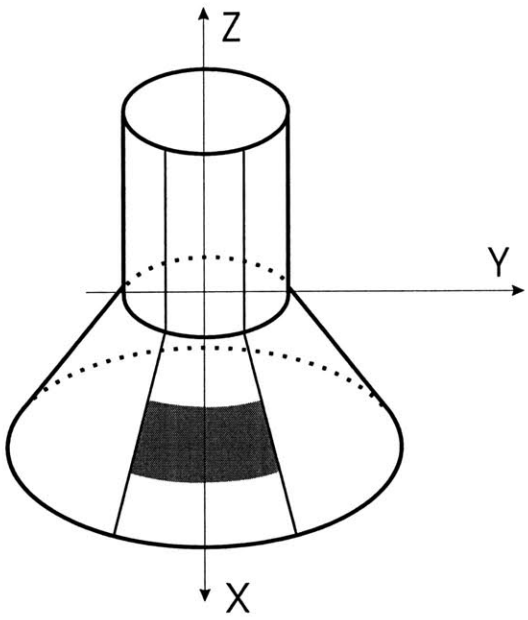

Figure 2-11: Funnel geometry. The loaded area (filled area) and the rulings (thin lines) issued from the singular points of the loading are presented.

mesh consisting of 80x100 elements in the part corresponding to $|\theta| < \pi/2$ and 20x100 elements in the part corresponding to $\pi/2 < \theta < 3\pi/2$. Besides the internal layers that are present in the conical part of the geometry, an interesting feature of the deformation pattern is the presence of internal layers in the cylindrical part of the geometry. As seen in the view from above in Figure 2-13, these take the form of damped oscillations originating from the continuation in the cylindrical part of the geometry of the rulings issued from the singular points in the loading, see Figure 2-11. To illustrate how the presence of boundary and internal layers is influenced by boundary conditions, in Figure 2-16 we show the results of a simulation identical to the preceding one except that the top edge ($z = 6$) is now clamped. With these modified boundary conditions the is no internal layer in the cylindrical part of the shell.

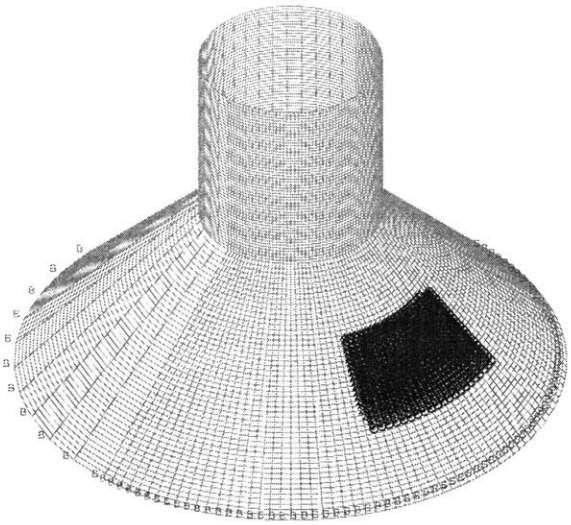

Figure 2-12: Funnel problem model. The original geometry and non-uniform mesh with the loading. The boundary condition is indicated.

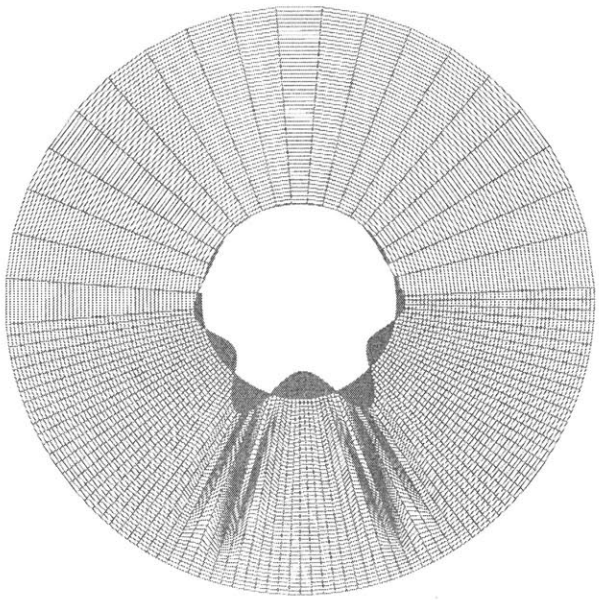

Figure 2-13: Funnel deformed geometry (I). In this view from above, the dampened oscillatory shape of the internal layer in the conical part of the geometry is apparent.

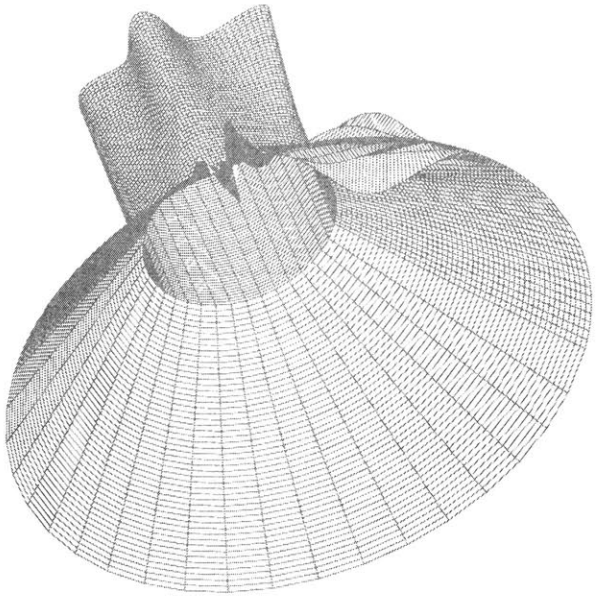

Figure 2-14: Funnel deformed geometry (II). In this view from below, the shape of the internal layer in the conical part of the geometry is apparent.

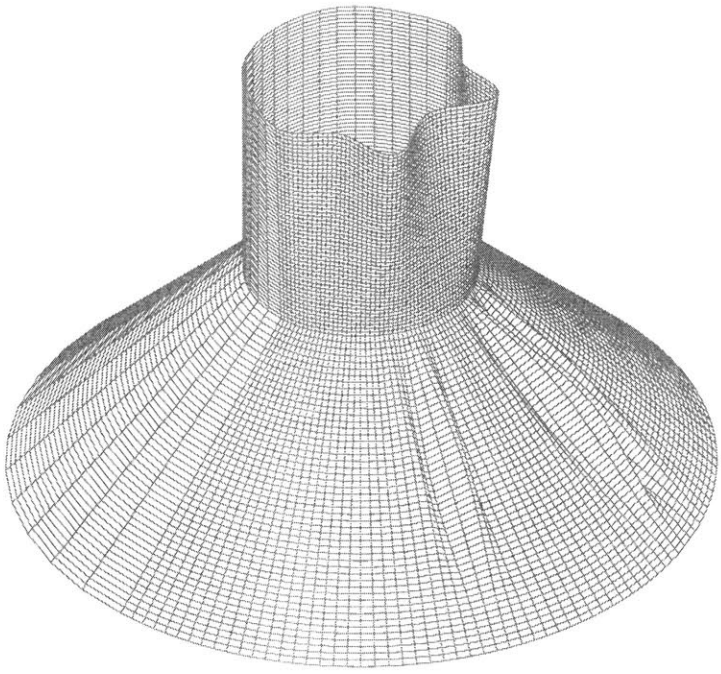

Figure 2-15: Funnel deformed geometry (III). This side view shows the internal layers in both the conical and cylindrical part of the geometry.

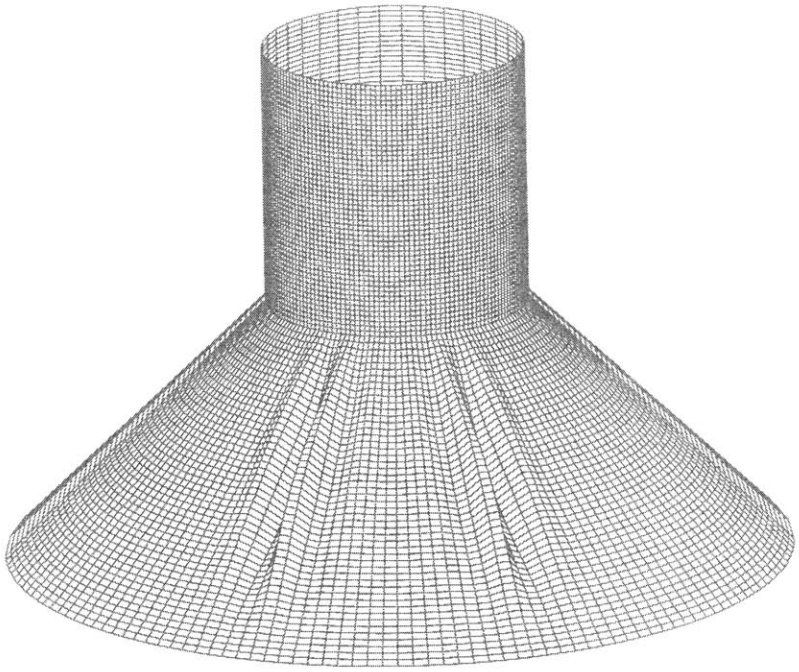

Figure 2-16: Deformed geometry of the funnel with modified boundary condition.

Along singular lines of the loading We consider the problem of the shell (see Figure 2-17) with an elliptic mid-surface of equation

$$\begin{cases} |x| < 5 \\ |y| < 5 \\ z = \frac{1}{20}(x^2 + y^2) \end{cases} \tag{2.38}$$

and thickness $t = 10^{-3}$, clamped along its entire boundary and subjected to a loading with magnitude one per unit area and direction y applied to the part of the mid-surface defined by

$$\begin{cases} |x| < 1 \\ |y| < 2 \end{cases} \tag{2.39}$$

This problem is solved with a non-uniform mesh consisting of 100x100 MITC4 elements. The solution features an internal layer all along the discontinuity in the loading and a boundary layer along the boundary of the shell. The boundary layer has an intensity that is much smaller than that of the internal layer.

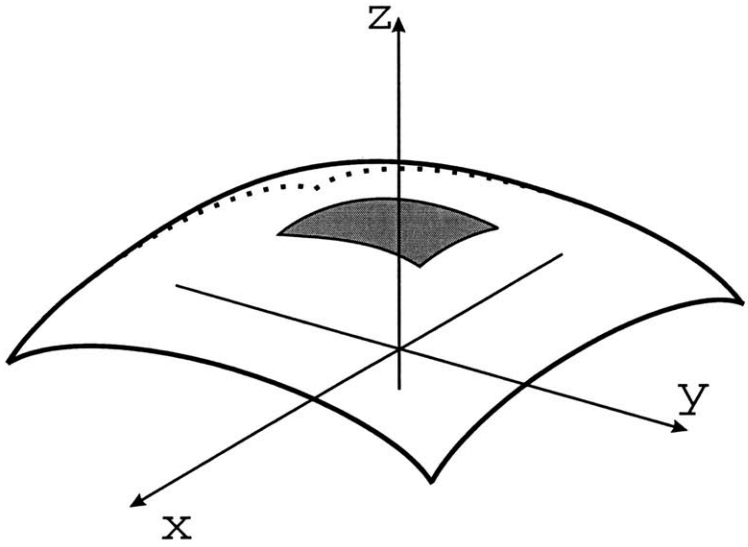

Figure 2-17: Geometry of the elliptic surface and loaded area. The loading is applied to the filled area. The entire boundary is clamped.

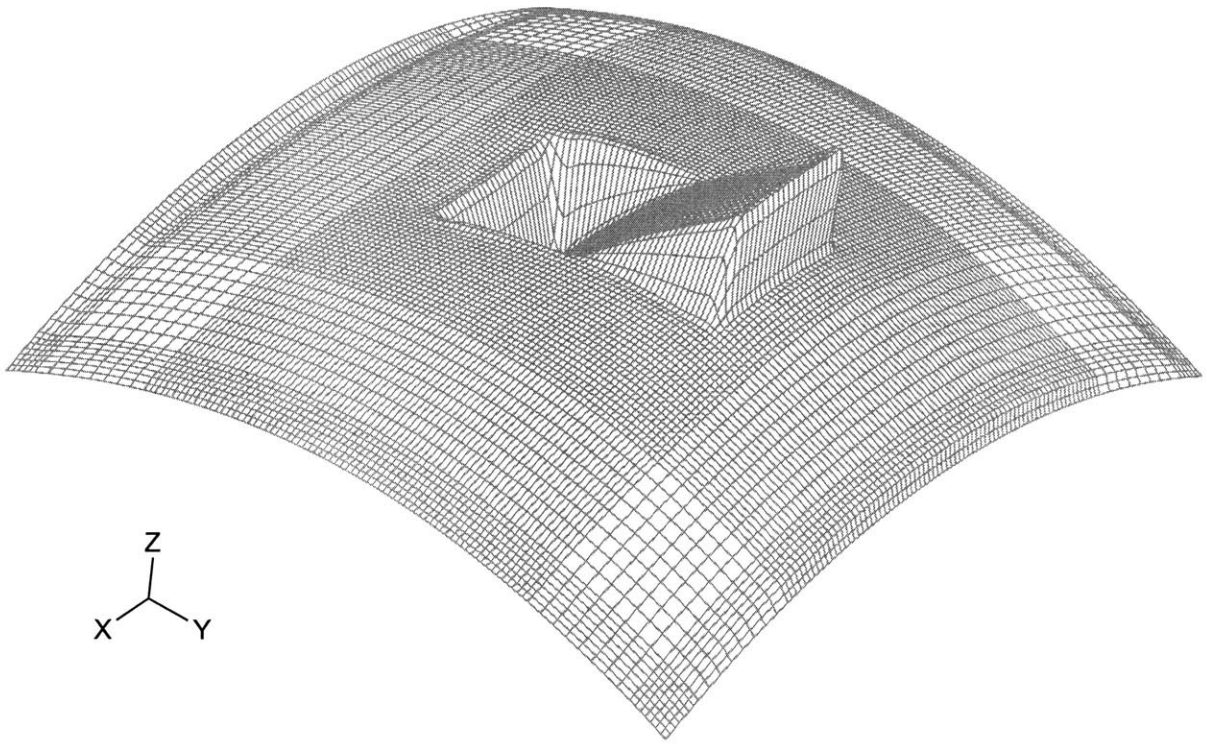

Figure 2-18: Deformation of an elliptic surface. The presence of boundary layers along the singular line of the loading is clear. There are also smaller layers along the clamped boundary. The layers along the parts of the boundary that satisfy $y = constant$ are the most visible.

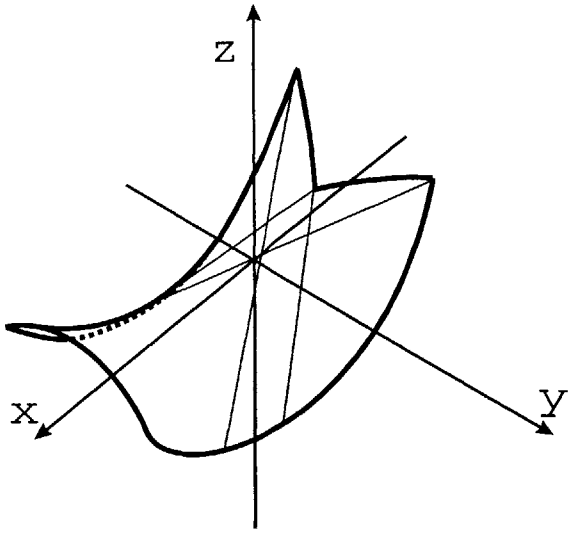

Figure 2-19: Geometry of the hyperbolic paraboloid with a reentrant corner. The entire boundary is clamped. Asymptotic lines originating from singular points of the boundary are indicated.

Along the rulings issued from the singular points of the boundary We consider the hyperbolic paraboloid section of thickness $t = 10^{-5}$ defined by

$$\begin{cases} z = (x^2 - y^2)/100 \\ |y| < 50 \\ -75 - y/4 < x < 50 \text{ when } 0 < y \\ -75 + y/4 < x < 50 \text{ when } y < 0 \end{cases} \tag{2.40}$$

clamped along its boundary and subjected to a uniform loading in the z direction of magnitude one per unit area on its whole mid-surface. A hyperbolic paraboloid is a doubly-ruled surface. This mid-surface possesses a reentrant corner at $(x, y) = (-75, 0)$, see Figure 2-19.

The deformed geometry obtained through a numerical simulation with a 100x100 mesh is presented in Figure 2-20. Besides a boundary layer along the entire boundary, the solution features internal layers issued from the reentrant corner and the points $(x, y) = (-100, -50)$ and $(x, y) = (-100, 50)$.

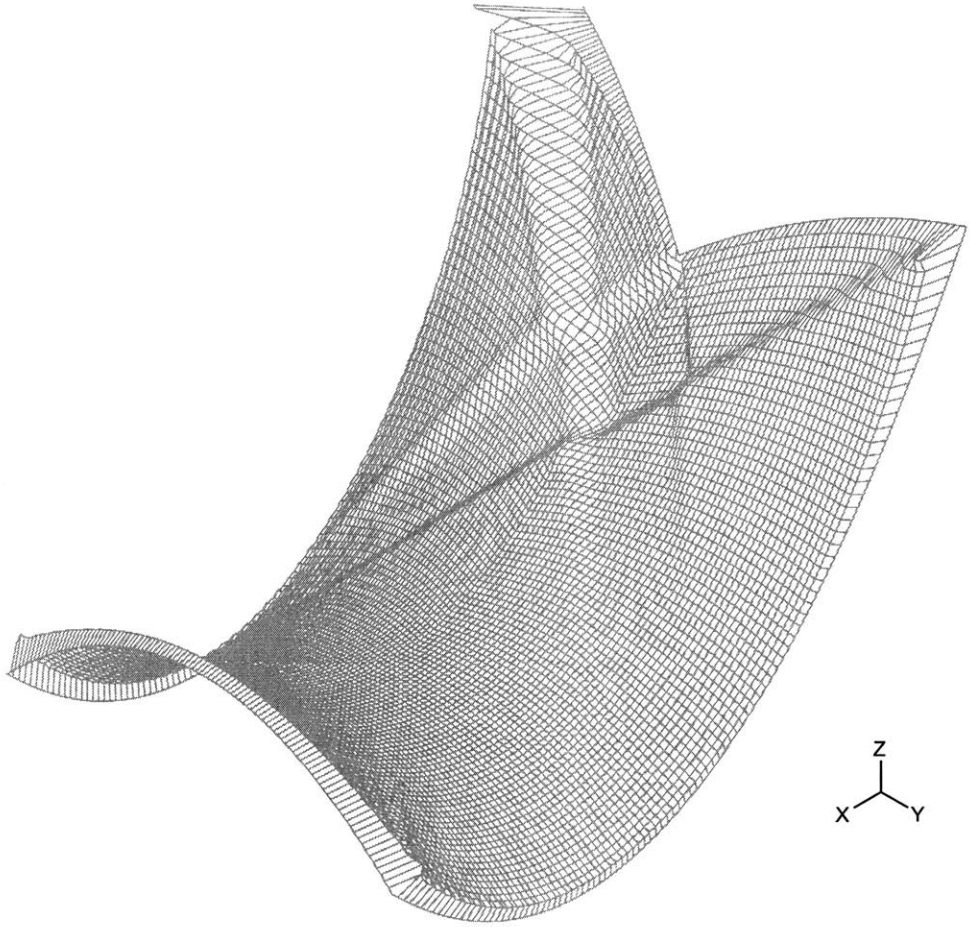

Figure 2-20: Deformed geometry of the hyperbolic paraboloid with a reentrant corner.

Along a curve where either the tangent plane or curvatures are discontinuous. We consider the "lamp shade" shape defined by the equations

$$\begin{cases} x^2 + y^2 = (3 + \sqrt{z - \frac{1}{2}} - \sqrt{\frac{1}{2}})^2 \\ -6 < z < 0 \end{cases} \tag{2.41}$$

and

$$\begin{cases} x^2 + y^2 = 9 \\ 0 < z < 6 \end{cases} \tag{2.42}$$

The thickness is $t = 10^{-3}$. A loading of magnitude one per unit area and of direction x is applied over the part of the mid-surface with equation

$$\begin{cases} |\theta| < \pi/8 \\ -4 < z < -2 \end{cases} \tag{2.43}$$

where θ is the polar angle about the z direction. The shell is clamped along the edges corresponding to $z = -6$ and $z = 6$. The geometry of the mid-surface as well as the loading are presented in Figure 2-21 The results of the numerical simulation are presented in Figure 2-22 . The mesh employed is a non-uniform mesh consisting of 80x100 elements in the part corresponding to $|\theta| < \pi/2$ and 20x100 elements in the part corresponding to $\pi/2 < \theta < 3\pi/2$. Besides the internal layers that are present in the tapered part of the geometry, an interesting feature of the deformation pattern is the presence of an internal layer along the curve separating the tapered and the cylindrical part of the geometry. This should be contrasted with Figure 2-15.

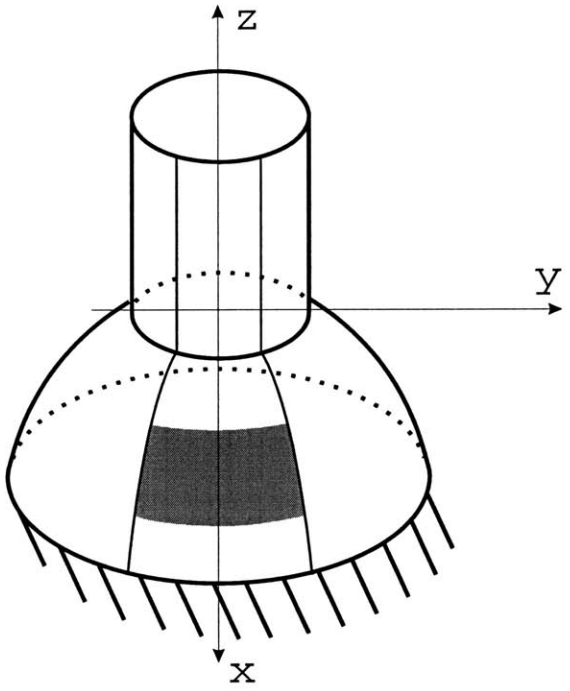

Figure 2-21: Finite element model for the "lamp shade".

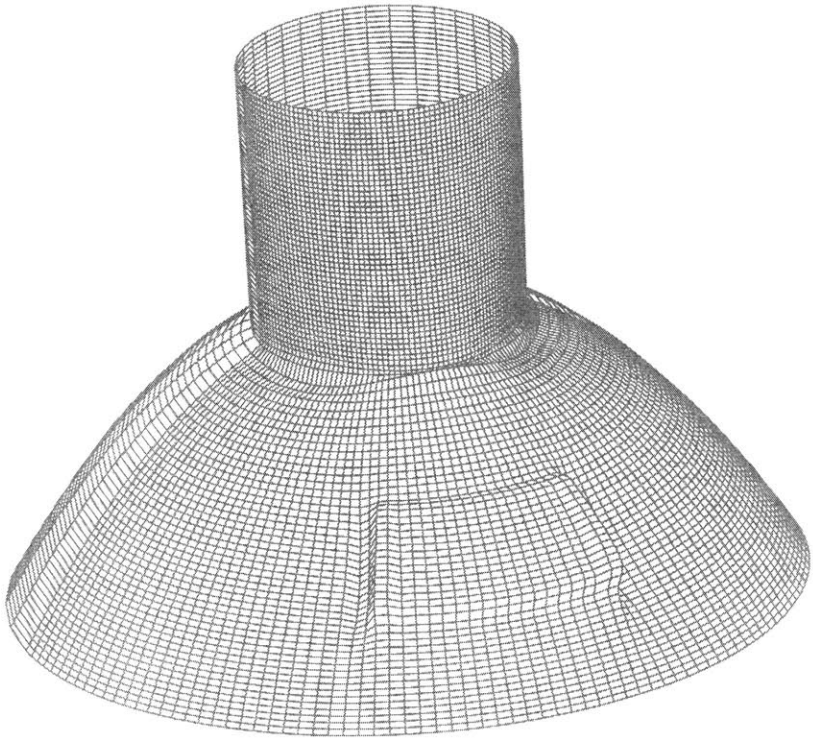

Figure 2-22: Deformed geometry of the "lamp shade".

Chapter 3

Finite Element Analysis of Shells

In this chapter, we introduce the finite element approximation of the variational problem developed in Chapter 1 and review the difficulties encountered when the classical displacement-based approach is followed. Different remedies to these problems are introduced, in particular the use of mixed interpolation methods. Specifically, the MITC approach is detailed. We then discuss the numerical tests that are designed to test shell finite element formulations and we discuss briefly the limits of the current knowledge of these mixed-interpolated methods. More details are given in References [22, 9, 10, 11, 12, 19].

3.1 Displacement-based methods

3.1.1 From the continuum to the discrete problem

We consider the solution by the finite element method [11] of a well-posed shell problem. It is assumed in the following that an appropriate mathematical model has been chosen so that the problem admits a unique solution. This means in particular that the operators $A_b(.,.)$, $A_m(.,.)$ and $G(.)$ are defined as in Sections 1.2.3 or 1.2.4 and that the functional space $\mathcal{V}$ is given by the results of Section 1.2.6.

3.1.2 Formulation of displacement-based elements

The standard displacement-based finite element procedure consists in seeking an approximate solution U_h to the problem (derived in Chapter 1)

$$\text{Find } U \in \mathcal{V}, \quad \epsilon^3 A_b(U,V) + \epsilon A_m(U,V) = G(V) \quad \forall V \in \mathcal{V} \tag{3.1}$$

in a finite-dimensional space $\mathcal{V}_h \subset \mathcal{V}$:

$$\text{Find } U_h \in \mathcal{V}_h, \quad t^3 A_b(U_h,V_h) + t A_m(U_h,V_h) = G(V_h) \quad \forall V_h \in \mathcal{V}_h \tag{3.2}$$

In practice, the stiffness matrix for a general displacement-based shell element can be established as follows. The first step consists in combining the linearized version of the Green-Lagrange covariant strains

$$e_{ij} = \frac{1}{2}\left(\frac{\partial U_n}{\partial \xi^i}\cdot\frac{\partial x_n}{\partial \xi^j} + \frac{\partial U_n}{\partial \xi^j}\cdot\frac{\partial x_n}{\partial \xi^i}\right) \tag{3.3}$$

the assumed Cartesian displacement patterns

$$U_i = \sum_{k=1}^{N} h_k U_i^k + \frac{\xi^3}{2}\sum_{k=1}^{N} a_k h_k (-V_{2i}^k \alpha_k + V_{1i}^k \beta_k) \tag{3.4}$$

and the interpolated geometry

$$x_i = \sum_{k=1}^{N} h_k X_i^k + \frac{\xi^3}{2}\sum_{k=1}^{N} a_k h_k V_{ni}^k \tag{3.5}$$

where U_i denotes the i^{th} cartesian component of the displacement, U_i^k is the i direction displacement of node k, X_i^k is the i^{th} coordinate of node k, V_{ni}^k is the i^{th} component of the director vector at node k and V_1^k and V_2^k are two vectors orthogonal to the director vector at node k. This leads to an expression for the covariant strains that can be written in the following matrix form:

$$(e_{rr}, e_{ss}, e_{tt}, 2e_{rs}, 2e_{st}, 2e_{rt})^T = B_{cov}^{DI} U \tag{3.6}$$

where U is the vector of all the degrees of freedom for the element and B_{cov}^{DI} is the displacement/covariant strains matrix. These strains and the material law for the shell (including the assumption that there is no stress through the thickness) are then expressed on dual bases and the element stiffness matrix is obtained by numerically carrying out the integration:

$$K_{el} = \int_{\Omega_K} B^T C B d\Omega_K \tag{3.7}$$

where B is the displacement/covariant strain matrix, C is the shell material law expressed in the corresponding contravariant basis and Ω_K is the domain occupied by the element considered. In this general shell element the numerical integration is carried out typically through the use of the Gaussian quadrature method. The integration orders in the three directions of integration should be selected high enough that spurious zero-energy modes are not present. However, because the cost of the numerical integration is essentially directly proportional to the number of integration points employed, using superfluous integration points should be avoided. Following [11], we use in this work the lowest integration order that allows exact integration of the stiffness matrix of undistorted elements ("full integration").

3.1.3 Limitations

In this traditional approach, all 5 fields of the Reissner-Mindlin kinematics are approximated by element-wise polynomial functions. This method performs satisfactorily in the case of problems that are membrane-dominated in the infinitely thin shell limit. However, in the case of asymptotically bending-dominated problems, the displacement-based shell finite elements are known to show poor performance. The convergence rate of the finite element solution to the exact solution of the problem as the typical element size h is reduced is lower than expected from the polynomial order of the elements used in the discretization. In some cases, convergence may be lost altogether. As a result, the displacement-based method overestimates the stiffness of the structure considered, a phenomenon known as "locking". At a given thickness,

the analysis of the convergence of the finite element solution to the mathematical solution as the typical element size h is decreased is classical. This analysis is based on the Lax-Milgram theorem and Cea's lemma (See for instance [30]). Cea's lemma gives us a measure of how effective at approximating the mathematical solution our element element is (in fact it can be seen that Cea's lemma gives the best bound on the performance of our finite element scheme). It is clear that if the distance of the finite element space $\mathcal{V}_h$ to the exact solution, as measured by the energy norm, is large then our finite element scheme will not be good. In some cases, it may happen that as the mesh is refined the distance from the finite element space to the solution does not decrease, leading to the complete loss of convergence mentioned above.

In engineering, locking may manifest itself as follows. While solving a shell problem with a finite element program, a practitioner will obtain an acceptable level of error in the finite element solution for a certain mesh. If the problem is solved again with a smaller shell thickness, the error increases to an unacceptably high level. The error level becomes acceptable again if the problem is solved again with a second finer (possibly much finer) mesh. But if the thickness is decreased once again and the problem solved anew with the second finer mesh, the level of error becomes unacceptable again unless an even finer mesh is employed. In other words, we have a situation where the error level is not uniform with the thickness of the shell.

An other form of locking appears when, at a given shell thickness, the convergence of the finite element solution to the exact solution does not occur at the optimal order allowed by the interpolation spaces used in the finite element formulation.

In the absence of locking the convergence of the finite element solution to the exact solution is uniformly optimal, i.e. there exists a constant C such that

$$\frac{||U - U_h||_*}{||U||_*} \leq Ch^k \tag{3.8}$$

where U is the exact solution, U_h is the finite element solution, h is the typical element size, k is the order of the complete polynomial included in the formulation and $||.||_*$ denotes an appropriate norm. Locking occurs when an inequality of the form 3.8

does not hold, either because we can not find a constant that is independent of the thickness or because the order of convergence is lower than k.

This phenomenon can be roughly explained as follows (see also [11]). Let us consider the simpler case of a flat shell, i.e. a plate, so the transverse shear strain is simply (see Equation 1.21):

$$\zeta_\alpha(\vec{u}, \bar{\theta}) = \frac{1}{2}(\theta_\alpha + u_{3,\alpha}) \tag{3.9}$$

We note that this expression for the transverse shear strains involves derivatives of two different orders: the transverse displacement u_3 appears in the form of its first derivative, whereas the rotation θ_α appears directly. In a finite element model using uniform 4-node displacement-based elements, since the rotations and the transverse displacements are approximated using the same element-wise bilinear polynomial functions, the finite element transverse shear strains can vanish only if the finite element rotation and the transverse displacement fields vanish (assuming homogenous boundary conditions). This implies that this displacement-based element can not represent a state of vanishing transverse shear strains without the rotations and transverse displacements going to zero. This is an issue in bending-dominated problems because in these problems we know that the strain energy due to the transverse shears must be negligible compared to bending energy. In such bending-dominated case, with the appropriate scaling for the loading, we solve the following finite element problem for various values of ϵ with a given mesh

$$\text{Find } U_h^\epsilon \in \mathcal{V}_h, \quad A_b(U_h^\epsilon, V_h) + \tfrac{1}{\epsilon^2} A_m(U_h^\epsilon, V_h) = F_b(V_h) \quad \forall V_h \in \mathcal{V}_h \tag{3.10}$$

As the bending energy of the finite element solution converges to some limit as ϵ goes to zero (see Section 2.1), the transverse shear energy of the finite element solution goes to zero (since we are considering a plate, the membrane energy does not appear in the form $A_m(.,.)$). This implies that the finite element transverse shear strain energy goes to zero in all the elements, and therefore the nodal transverse displacements and the nodal rotations must go to zero for the reasons given before.

Similarly, if we consider the quadrilateral 9-node displacement-based element, one sees from 3.9 that the quadratic part of the rotations need to vanish in order for the transverse shear strains to vanish. This implies that under the condition that the transverse shear strain vanish we can not expect to observe the rate of convergence that we would usually have with a quadratic interpolation.

The locking phenomenon is a fundamentally numerical one. As a matter of fact, in the continuum problem the exact transverse shear strain energy goes to zero but that does not imply that the transverse displacements or rotations go to zero, because the space $\mathcal{V}$, unlike $\mathcal{V}_h$, contains functions that are not polynomials. This analysis of the locking phenomenon suggests a possible remedy. To allow for non-zero transverse displacements and rotations when the transverse shear strains vanish, one could interpolate transverse displacements and rotations using polynomials of different order, for example one can think of formulating a quadrilateral element with 9 degrees of freedom for the transverse displacement and 4 degrees of freedom for each of the two rotations[1]. This is the idea of the reduced rotation method. It is shown to be equivalent to using reduced integration to evaluate the part of the stiffness matrix corresponding to the transverse shear strain energy. Unfortunately, (selective) reduced integration is known to yield unreliable elements since structures modelled with such elements may contain spurious zero-energy non-rigid-body modes [33, 11], which makes them inappropriate for practical engineering.

In the case of a plate, the only locking phenomenon occurs due to the transverse shear strain energy, and is therefore labelled "shear locking". In the case of a "true" shell –by which we mean one that is not a plate–, locking can also occur due to the membrane strains, for the exact same reasons: the membrane strains

$$\gamma_{\alpha\beta}(\vec{u}) = \frac{1}{2}(u_{\alpha|\beta} + u_{\beta|\alpha}) - b_{\alpha\beta}\, u_3 \tag{3.11}$$

[1]An element with 16 translation and 9 rotation degrees of freedom could also be considered, etc.

shows the same imbalance in differentiation orders as the transverse shear strains. The phenomenon is then referred to as "membrane locking". It does not occur in plates because with the flat geometry the second fundamental form in 3.11 vanishes. For a further discussion of locking issues, see References [11, 12].

3.2 Mixed-interpolation methods

3.2.1 General method

The numerical difficulties encountered with displacement-based finite element formulations when dealing with thicknesses of practical engineering importance means these methods are of little use. To remedy these problems, mixed-interpolation methods have been developed. We focus here on one such method, the Mixed Interpolation of Tensorial Components (MITC) method. In this approach, displacements of the mid-surface of a shell structure are approximated using the same basis functions as in the displacement-based method. However, whereas in the displacement-based method the strain field is directly derived from the nodal displacements using the derivatives of the displacements, in the MITC approach some of the tensorial strain components are obtained as a linear combination of assumed shape functions. The weights of these linear combinations are chosen so that the resulting strains are equal at certain points to the strains obtained in the displacement-based approach. These points are naturally called tying points. The idea consists in carefully choosing the appropriate number of tying points and locations for these tying points for the different strain components so as to remove the locking phenomenon. The finite element problem can then be stated in the form

$$\text{Find } U_h \in \mathcal{V}_h, \quad \epsilon^3 A_b^h(U_h, V_h) + \epsilon A_m^h(U_h, V_h) = G(V_h) \quad \forall V_h \in \mathcal{V}_h \tag{3.12}$$

to be compared with Equation 3.2 which relates to displacement based methods. There exist several closely related mixed formulations for shells structures, which only differ from one another in the way the forms A_m^h and A_b^h are evaluated. In

the following we show how these forms are evaluated in the MITC formulation, and justify this approach.

3.2.2 The MITC shell elements

Recalling the formulation of the general displacement-based shell elements presented in Section 3.1.2, we had expressed the covariant strains in terms of the nodal degrees of freedom in the form:

$$(e_{rr}, e_{ss}, e_{tt}, 2e_{rs}, 2e_{st}, 2e_{rt})^T = B_{cov}^{DI} U \tag{3.13}$$

which we can rewrite in the form

$$(e_{rr}, e_{ss}, e_{tt}, 2e_{rs}, 2e_{st}, 2e_{rt})^T = \begin{pmatrix} B_{rr}^{DI} \\ B_{ss}^{DI} \\ B_{tt}^{DI} \\ B_{rs}^{DI} \\ B_{st}^{DI} \\ B_{rt}^{DI} \end{pmatrix} U \tag{3.14}$$

where we denote by $B_{\xi^i\xi^j}^{DI}$ the rows of the matrix B_{cov}^{DI}. In the MITC formulation, the strain e_{tt} is set to zero (its analytical value in the exact solution considering our model) and some of the remaining components of the covariant strain tensor are interpolated using assumed shape functions. Which of the strain components are treated this way depends on which MITC element is considered: in the 4-node MITC element[2], only e_{rt} and e_{st} are mixed-interpolated, whereas in the 9- and 16-node MITC elements all five remaining strains are mixed-interpolated (see for instance [11, 18, 17]). The assumed shape functions employed vary from strain to strain and from element to element and are summarized in Section 3.2.3. The assumed strains are related to the nodal displacements through the assumption that the assumed strains are equal

[2]Following the traditional convention, we call MITC4 the 4-node MITC element, MITC9 the 9-node MITC9 element and MITC16 the 16-node MITC element [11, 18, 17].

to the directly interpolated strains throughout the thickness[3] at a number of tying points:

$$e_{\xi^i\xi^j}(r,s,t) = \sum_{k=1}^{k=n_{ij}} B^{DI}_{\xi^i\xi^j}(r^k_{ij}, s^k_{ij}, t) h^k_{ij}(r,s) U \tag{3.15}$$

where n_{ij} is the number of tying points for the strain component and element considered, r^k_{ij} and s^k_{ij} are the coordinates of the corresponding tying points and h^k_{ij} are the assumed shape functions. These assumed shape functions satisfy

$$h^k_{ij}(r^l_{ij}, s^l_{ij}) = \delta^l_k \tag{3.16}$$

Equation 3.15 can be put in the form

$$e_{\xi^i\xi^j}(r,s,t) = B^{AS}_{ij} U \tag{3.17}$$

where B^{AS} is the displacement/assumed strain matrix. The displacement/covariant strain relationship for the MITC4 shell element is then given by:

$$(e_{rr}, e_{ss}, e_{tt}, 2e_{rs}, 2e_{st}, 2e_{rt})^T = \begin{pmatrix} B^{DI}_{rr} \\ B^{DI}_{ss} \\ 0 \\ B^{DI}_{rs} \\ B^{AS}_{st} \\ B^{AS}_{rt} \end{pmatrix} U \tag{3.18}$$

The strain tensor and material law (including the assumption of no through-thickness stress) are then expressed on a set of dual bases, multiplied and integrated in a similar

[3]Note that in the original formulation [17] the proposed tying scheme involved imposing that the assumed transverse strains be equal to the directly interpolated strains at the mid-surface only. We tested both formulations and did not find any significant impact on the results. All results reported in this work are based on the original formulation.

fashion as for displacement-based elements:

$$K_{el} = \int_{\Omega_K} B^T C B d\Omega_K \tag{3.19}$$

where B denotes the strain displacement matrix for the MITC element.

3.2.3 MITC assumed shape functions and tying points

In this section, we give the shape functions employed for the assumed strains and we list the coordinates of the tying points. We follow the notation used in [10]: $\tilde{\mathcal{E}}_{13}^h$ denotes the space spanned by the assumed shape functions used for e_{13}, etc. It is understood that the assumed shape functions vanish outside of the element considered.

MITC4 element

$$\begin{cases} n_{13} = 2 \\ \tilde{\mathcal{E}}_{13}^h = \text{span}\{1, s\} \\ \left\{(r_{13}^k, s_{13}^k), k \in \{1,2\}\right\} = \{(0,1),(0,-1)\} \end{cases} \tag{3.20}$$

$$\begin{cases} n_{23} = 2 \\ \tilde{\mathcal{E}}_{23}^h = \text{span}\{1, r\} \\ \left\{(r_{23}^k, s_{23}^k), k \in \{1,2\}\right\} = \{(1,0),(-1,0)\} \end{cases} \tag{3.21}$$

MITC9 element

$$\begin{cases} n_{11} = n_{13} = 6 \\ \tilde{\mathcal{E}}_{11}^h = \tilde{\mathcal{E}}_{13}^h = \text{span}\{1, r, s, rs, s^2, rs^2\} \\ \left\{(r_{11}^k, s_{11}^k), k \in \{1,..,n_{11}\}\right\} = \left\{(r_{13}^k, s_{13}^k), k \in \{1,..,n_{13}\}\right\} = ... \\ ... = \{-\frac{1}{\sqrt{3}}, \frac{1}{\sqrt{3}}\} \times \{-\sqrt{\frac{3}{5}}, 0, \sqrt{\frac{3}{5}}\} \end{cases} \tag{3.22}$$

$$\begin{cases} n_{22} = n_{23} = 6 \\ \tilde{\mathcal{E}}^h_{22} = \tilde{\mathcal{E}}^h_{23} = \text{span}\{1, r, s, rs, r^2, sr^2\} \\ \{(r^k_{22}, s^k_{22}), k \in \{1, .., n_{22}\}\} = \{(r^k_{23}, s^k_{23}), k \in \{1, .., n_{23}\}\} = ... \\ ... = \{-\sqrt{\frac{3}{5}}, 0, \sqrt{\frac{3}{5}}\} \times \{-\frac{1}{\sqrt{3}}, \frac{1}{\sqrt{3}}\} \end{cases} \tag{3.23}$$

$$\begin{cases} n_{12} = 4 \\ \tilde{\mathcal{E}}^h_{12} = \text{span}\{1, r, s, rs\} = Q_1 \\ \{(r^k_{12}, s^k_{12}), k \in \{1, .., n_{12}\}\} = \{-\frac{1}{\sqrt{3}}, \frac{1}{\sqrt{3}}\} \times \{-\frac{1}{\sqrt{3}}, \frac{1}{\sqrt{3}}\} \end{cases} \tag{3.24}$$

MITC16 element

$$\begin{cases} n_{11} = n_{13} = 12 \\ \tilde{\mathcal{E}}^h_{11} = \tilde{\mathcal{E}}^h_{13} = \text{span}\{1, r, s, r^2, rs, s^2, r^2 s, rs^2, s^3, r^2 s^2, rs^3, r^2 s^3\} \\ \{(r^k_{11}, s^k_{11}), k \in \{1, .., n_{11}\}\} = \{(r^k_{13}, s^k_{13}), k \in \{1, .., n_{13}\}\} = ... \\ ... = \{-\sqrt{\frac{3}{5}}, 0, \sqrt{\frac{3}{5}}\} \times \{\pm\sqrt{(\pm\sqrt{480} + 30)/70}\} \end{cases} \tag{3.25}$$

$$\begin{cases} n_{22} = n_{23} = 12 \\ \tilde{\mathcal{E}}^h_{22} = \tilde{\mathcal{E}}^h_{23} = \text{span}\{1, r, s, r^2, rs, s^2, r^3, r^2 s, rs^2, r^3 s, r^2 s^2, r^3 s^2\} \\ \tilde{\mathcal{E}}^h_{22} = \tilde{\mathcal{E}}^h_{23} = \text{span}\{1, r, s, rs, r^2, sr^2\} \\ \{(r^k_{22}, s^k_{22}), k \in \{1, .., n_{22}\}\} = \{(r^k_{23}, s^k_{23}), k \in \{1, .., n_{23}\}\} = ... \\ ... = \{\pm\sqrt{(\pm\sqrt{480} + 30)/70}\} \times \{-\sqrt{\frac{3}{5}}, 0, \sqrt{\frac{3}{5}}\} \end{cases} \tag{3.26}$$

$$\begin{cases} n_{12} = 9 \\ \tilde{\mathcal{E}}^h_{12} = \text{span}\{1, r, s, r^2, rs, s^2, rs^2, sr^2, r^2 s^2\} = Q_2 \\ \{(r^k_{12}, s^k_{12}), k \in \{1, .., n_{12}\}\} = \{-\sqrt{\frac{3}{5}}, 0, \sqrt{\frac{3}{5}}\} \times \{-\sqrt{\frac{3}{5}}, 0, \sqrt{\frac{3}{5}}\} \end{cases} \tag{3.27}$$

Note that $\pm\frac{1}{\sqrt{3}}$ (respectively $\{-\sqrt{\frac{3}{5}}, 0, \sqrt{\frac{3}{5}}\}$ and $\pm\sqrt{(\pm\sqrt{480} + 30)/70}$) are the two (respectively three and four) solutions of the equation (respectively and $35x^4 - 30x^2 + 3 = 0$), i.e. the zeros of the second (respectively third and fourth) Legendre polynomial. Their approximate explicit expressions are $\pm 0.57735...$ (respectively $\{-0.77459..., 0, 0.77459...\}$ and $\{-0.86113..., -0.33998..., 0.33998..., 0.86113...\}$).

3.2.4 Justification

We saw in the previous section that the locking phenomenon was due to the imbalance of the differentiation orders in strain components such as (for a flat element):

$$\zeta_\alpha(\vec{u}, \bar{\theta}) = \frac{1}{2}(\theta_\alpha + u_{3,\alpha}) \tag{3.28}$$

Considering like in Section 3.1.3 a problem with Dirichlet boundary conditions solved with 4-node elements, we can show that in the MITC formulation, the constraint

$$\zeta_1^h = 0 \tag{3.29}$$

does not imply that both the translation u_3 and rotation θ_1 must vanish as it did in the displacement-based formulation. As a matter of fact, in the MITC4 element, the transverse shear ζ_1 is related to nodal displacements through Equation 3.15, and we can see from the assumed shape functions presented in the previous paragraph that it is possible to have a zero transverse shear strains with non-zero displacements. For instance if the nodal displacements are such that

$$\begin{cases} \theta_1^h = r + 1 \\ u_3^h = r - 1 \end{cases} \tag{3.30}$$

we have for the assumed transverse shear strain

$$2 * \zeta_1^{AS} = (\theta_1^h - u_{3,1}^h)|_{(0,1)} * \frac{1+s}{2} + (\theta_1^h - u_{3,1}^h)|_{(0,-1)} * \frac{1-s}{2} = 0 \tag{3.31}$$

Hence with the MITC4 shell element it is possible to have non-vanishing translation u_3 and rotation θ_1 while satisfying the zero transverse shear constraint, unlike with the displacement-based 4-node shell element. Indeed the plate bending and plane stress patch tests are satisfied [7]. This means that the constraints have been relaxed by the MITC formulation. A similar reasoning is valid for other strain components and elements. In Appendix B, we give the example of a beam in flexion due to a tip

moment and show that the mixed-interpolated elements give no spurious shear and do not lock.

3.3 Analysis of shell formulations

3.3.1 Mathematical analysis of a shell formulation

To be considered reliable and efficient, a shell finite element formulation must satisfy three conditions, which we summarize here and have been discussed in great detail in [4, 22, 6, 9, 10, 11, 18, 24, 15, 34, 16, 35]. These three conditions are:

- Ellipticity: for the finite element problem to be solvable, the form $\epsilon^3 A_b^h(.,.) + \epsilon A_m^h(.,.)$ must be elliptic (see [30]) , i.e.

$$\exists C \in \mathbb{R} \quad \text{Such that } \forall U_h \in V_h, \quad \epsilon^3 A_b^h(U_h, U_h) + \epsilon A_m^h(U_h, U_h) \geq C||U_h||_{U_h}^2. \tag{3.32}$$

  Mathematically, this condition assures that the stiffness matrix K is positive definite. In physical terms, this means that the structure considered does not have any zero-energy mode (spurious mode). Of course if we consider an unsupported structure, we should have that 0 is an eigenvalue of the stiffness matrix with order six, corresponding to the six rigid-body modes. The ellipticity is relatively simple to verify since it suffices to verify that 0 is an eigenvalue of the stiffness matrix for a single un-supported element with order six exactly to assure the ellipticity of the form $\epsilon^3 A_b^h(.,.) + \epsilon A_m^h(.,.)$. If the formulation satisfies the ellipticity condition, the problem in Equation 3.12 can be solved. The ellipticity condition by itself does not guarantee that the solution of this problem is accurate (i.e. that as the mesh is refined the finite element solution converges to the solution of the mathematical problem given in Equation 1.49). For this, the form $\epsilon^3 A_b^h(.,.) + \epsilon A_m^h(.,.)$ also needs to satisfy consistency. The MITC elements have been shown to satisfy the ellipticity condition.

- Consistency: Replacing the form $\epsilon^3 A_b(.,.) + \epsilon A_m(.,.)$ by the form $\epsilon^3 A_b^h(.,.) +$

$\epsilon A_m^h(.,.)$ may introduce inconsistencies in the model, i.e. the solution of the finite element problem may not converge to the solution of the mathematical problem as the typical element size h tends to zero. In the absence of analytical proof of consistency, numerical patch tests (see [11]) are used to assess whether a finite element formulation is consistent. For the MITC elements, patch test results have been reported in [17, 24]. To avoid 'locking', we need to verify that consistency errors approach zero with the highest possible order of convergence for the finite element interpolation given. We refer to this order of convergence as the "optimal" convergence rate. Consistency of the MITC formulation has not been proven analytically, but it should be noted that despite the large use made of the MITC elements in research and industry we do not know of any problem that would indicate that the MITC elements are not consistent.

- Inf-Sup Condition: Ideally, a mixed finite element formulation should satisfy the appropriate Inf-Sup condition to guarantee that locking does not occur (see for instance [22, 11, 35]). Unfortunately it is generally not possible to prove analytically whether this condition is satisfied for a practical finite element formulation, and numerical tests must be employed (see [11, 35]). A numerical Inf-Sup test for shell elements was developed and applied to the MITC elements in [9, 35].

3.3.2 Numerical testing of shell finite element formulation

As was mentioned earlier, only limited analytical results can be carried out for the assessment of the performance of a practical shell finite element formulation. Typically, of the three mathematical requirements mentioned in Section 3.3.1 (ellipticity, consistency and Inf-Sup condition), only ellipticity can be shown analytically to hold or not, and this condition does not guarantee that the finite element solution converges to the exact solution of the mathematical problem, let alone establish whether this convergence is with the optimal order.

With analytical proofs of the Inf-Sup condition and consistency out of reach, we need to turn to carefully selected numerical experiments to assess the performance of finite element formulations. Great care must be taken in choosing these benchmark problems as we want to test the performance of finite elements over a wide range of conditions [22, 14, 19, 47]. As discussed earlier, we know that the performance of certain finite element formulations is widely different depending on whether we employ a membrane-dominated problem or a bending-dominated problem and it is therefore crucial to run benchmark problems that represent both ends of the asymptotic spectrum. Also, considering that in engineering practice boundary and internal layers are frequently present, we need to consider test problems that feature these layers. Finally the meshes employed in these tests should also be selected very carefully as an inappropriate meshing strategy may result in loss of optimal convergence, in particular when layers are present.

The goals of numerical tests are

- To determine whether a formulation is consistent.
- To evaluate whether a formulation locks.
- To determine the impact of various meshing schemes on convergence.

One difficulty attached to the numerical testing of shell finite elements is that, once a finite element code has been employed to solve a shell problem, it is not immediately obvious how to estimate the error between the finite element solution obtained and the exact solution to the mathematical problem (which is usually not known explicitly). In Chapter 4, we summarize the various approaches to error measurement that have been employed in the literature, indicate what problems are encountered with these approaches, introduce a new approach and use this proposed approach in some new benchmark problems.

Chapter 4

Convergence Analysis

In this chapter, we start by reviewing existing procedures employed to estimate the discrepancy between the exact solution to the mathematical shell problem of Equation 3.1 and the numerical solution of the corresponding mixed-formulated finite element problem expressed by Equation 3.12. Note that our focus is on mixed-interpolated finite elements because, for the reasons presented in Chapter 3, displacement-based finite elements are not used in practice. Following this review of existing error measurement techniques, we introduce a new error measure which does not suffer from the limitations of existing approaches. This proposed algorithm is then employed to study the convergence of the MITC family of elements. To that end, two new benchmark problems are introduced.

4.1 Measurement of the error

The estimation of the discrepancy between the exact solution of a mathematical problem and its approximate numerical solution is a crucial step in an analysis. In some cases, and in particular if a *displacement-based* finite element approach is used to reach the numerical solution, it is fairly simple to measure this error. As a matter of fact, it can easily be shown that the difference between the strain energy of the exact solution and the strain energy of the numerical solution defines a norm for the error in the displacements [11]. However, when mixed-interpolated formulations are

used, as is commonly the case in the analysis of shell problems, this approach can not be followed, and there is no well-established procedure to measure the error. A variety of techniques have been used by researchers over the years, and we review these techniques in Section 4.1.1. Based on the deficiencies and limitations of these existing techniques, we define in Section 4.1.2 the properties that an ideal error measure would satisfy, and in Section 4.1.3 we propose a new error measure. The details of the implementation of this error measure are given in Section 4.1.4.

4.1.1 Previous work

To evaluate the difference between the solution U of the mathematical problem 3.1 and the finite element solution U_h of the problem 3.12, researchers have mostly compared to reference solutions the values of displacements at a few points of the shell or the deformed shapes of special lines on the mid-surface. The reference solutions can either be obtained through analytical methods or numerical methods. Frequently when analytical methods are used, simplifying assumptions (shallow shell assumption, etc...) must be made to make the problem tractable. These assumptions can result in inconsistencies between the analytical problem and the numerical problem (i.e. as the mesh is refined in the finite element model, the finite element solution does not converge to the reference analytical solution because the reference solution and the finite element formulation are based on fundamentally different models). This is particularly the case when the finite elements considered are of the degenerated type (such as the MITC elements which we are interested in and other mixed interpolated formulations) because there are few analytical solutions to meaningful shell problems based on the degenerated approach. Even for simpler models, there are few meaningful complex problems for which closed-form analytical solutions exist at finite thicknesses. Often the analytical solutions that are available are in the form of infinite series (resulting from Fourier or similar analysis), the coefficients of which frequently need to be evaluated numerically.

In any case, in practice analytical solutions can be obtained only when very simple geometries are considered (although it must be said that these simple geometries may

be of some interest in engineering).

For all these reasons, numerical methods are frequently preferred in obtaining reference solutions. There are of course some pitfalls associated with this approach as well, in particular, the fact that the numerical scheme used to establish the reference solution must be consistent with the formulation analyzed. Another issue lies in obtaining a numerical reference solution that is sufficiently accurate. As shown in [11], if an inappropriate formulation is employed the number of finite elements needed to obtain a reasonably accurate reference solution can be much larger than it would be if an appropriate scheme were used. In fact, the number of elements needed may be so large that the problem can not be tackled by available computers. Clearly, the use of such formulations should be avoided. This problem is all the more crucial as we do not know of any well-established reliable error estimator[1] [32, 29, 1] for shells.

Whether an analytical or numerical reference solution is used, comparing point-wise values of the displacements to a reference can not give a *complete* measure of the accuracy of the finite element solution. Say for instance that the displacement at one point of a structure calculated using a series of increasingly refined meshes converges to the reference value; there is no guarantee whatsoever that displacements at other points converge identically (convergence may be non-uniform spatially) , and there is no guarantee that strains – which are often more critical in engineering analysis than displacements – converge at all at any point. Also, we observed in Section 1.2.6 that the appropriate space for the study of the convergence of Naghdi shell problems is a combination of H^1 spaces. Point-wise values of functions are meaningless in those spaces (see [30]).

In addition, comparing point-wise values of the displacements to a reference can not give a *quantitative* measure of the accuracy of the finite element solution. In principle, with such an approach, we could derive the order of convergence of the

[1]Error measurement procedures, the topic of this chapter, should not be confused with error estimators. While we set out to evaluate the discrepancy between U and U_h when U (or a close approximation thereof) is known, error estimators are used to evaluate the discrepancy between U and U_h without any knowledge of U. Error estimators are typically used in automatic re-meshing algorithms to determine what regions of a structure require mesh refinement.

finite element solution displacements to their reference value *at one point* or *along a line*. However, such studies are usually not carried out and, in the event that they were, they would not yield any information as to the convergence rate over the entire structure. Usually researchers content themselves to check that the finite element solution obtained with a rather coarse mesh makes physical sense by visually comparing it to a reference solution.

The fact that these methods are not quantitative implies that they can not be employed to rigorously analyze the presence of locking in a finite element formulation. That is not to say that these approaches are worthless. Indeed, when an engineer tackles a new problem or tackles a familiar problem with a new type of finite elements, these methods provide a quick check that a reasonable solution has been attained. However when a deeper understanding or assessment of the performance of a finite element formulation is sought more advanced techniques are clearly necessary.

In [9, 35, 31], a new approach to the problem was employed. This approach is inspired by properties of the displacement-based finite element method. Let us consider the problem

Find $U \in \mathcal{V}$ *such that*

$$A(U, V) = F(V) \quad \forall V \in \mathcal{V} \tag{4.1}$$

discretized into the displacement-based finite element problem

Find $U_h \in \mathcal{V}_h$ *such that*

$$A(U_h, V_h) = F(V_h) \quad \forall V_h \in \mathcal{V}_h \tag{4.2}$$

where as usual $\mathcal{V}_h \subset \mathcal{V}$ and $A(.,.)$ is a bilinear symmetric form that is coercive on the Hilbert space $\mathcal{V}$. Then it is well-known (see [1, 11, 30]) that we have the orthogonality property

$$A(U - U_h, V_h) = 0 \quad \forall V_h \in \mathcal{V}_h \tag{4.3}$$

(The error is orthogonal to the finite element space.) which yields immediately

$$A(U,U) = A(U_h,U_h) + A(U-U_h,U-U_h) \tag{4.4}$$

When embedded meshes with varying element sizes are used (By embedded we mean that with the ordering $h_1 > h_2 > h_3 > ... > 0$ we require $\mathcal{V}_{h_1} \subset \mathcal{V}_{h_2} \subset \mathcal{V}_{h_3} \subset ... \subset \mathcal{V}$), a classical result of convergence is (cf [11]):

$$||U-U_h||_{H^1} = ch^k||U||_{H^{k+1}} \tag{4.5}$$

where k denotes the order of completeness of the polynomials used in the construction of the finite element formulation (i.e. for elements including P1 polynomials, $k=1$, etc...), c is a constant (which depends on the materials properties but not on U), and h is the typical element size (conforming meshes being assumed). Using Equations 4.4 and 4.5, as well as equivalences (see [30]) between the three norms used, we see that we have

$$\ln(1-\frac{A(U_h,U_h)}{A(U,U)}) = \ln(c) + k\ln(h) \tag{4.6}$$

The order of convergence k can therefore be seen to be the slope of the graph "$ln(1-\frac{A(U_h,U_h)}{A(U,U)})$" versus "$ln(h)$".

This approach is particularly adequate to judge the accuracy of a finite element scheme: by construction it yields quantitative results and takes into account the quality of the finite element solution U_h over the entire mesh.

In [9, 35], this approach was extended to the assessment of the accuracy of mixed-formulated shell finite elements. In these studies, the authors plotted "$ln(|1-\frac{A^{AS}(U_h,U_h)}{A(U,U)}|)$" versus "$ln(h)$" where $A^{AS}(U_h,U_h)$ denotes the mixed-interpolated (assumed strains) energy of the finite element solution. Depending on the problems, values for $A(U,U)$ were obtained using either accurate semi-analytical solutions or accurate finite element solutions obtained through the use of very fine meshes of MITC elements (i.e. $A(U,U)$ was then replaced by $A^{AS}(U_{h\ fine}, U_{h\ fine})$).

There are a number of difficulties attached with extending to mixed formulations

an approach originally designed for the assessment of the performance of displacement-based formulations.

First, unlike in a displacement-based formulation where Equation 4.3 holds, in a mixed formulation no such result holds. This implies that we no longer have Equation 4.4, and therefore in general

$$A^{AS}(U,U) - A^{AS}(U_h,U_h) \neq A^{AS}(U-U_h,U-U_h) \tag{4.7}$$

which implies that

$$1 - \frac{A^{AS}(U_h,U_h)}{A^{AS}(U,U)} \neq \frac{A^{AS}(U-U_h,U-U_h)}{A^{AS}(U,U)} \tag{4.8}$$

As a result, $\ln(A^{AS}(U,U) - A^{AS}(U_h,U_h))$ is not equal to $\ln(A^{AS}(U-U_h,U-U_h))$. There is also no guarantee that $A^{AS}(U,U) - A^{AS}(U_h,U_h)$ is positive, and numerical experiments show that this quantity is frequently negative.

This is an immediate result of the energy convergence not being from below in a mixed formulation. In a displacement-based formulation, if we consider a series of embedded meshes of typical element sizes $h_1 > h_2 > h_3 > ... > 0$, then it is assured that we have

$$A(U_{h_1},U_{h_1}) \leq A(U_{h_2},U_{h_2}) \leq A(U_{h_3},U_{h_3}) \leq ... \leq A(U,U) \tag{4.9}$$

In the case of mixed methods, we do not have a similar result, and although for reasonable elements we have $A^{AS}(U_{h_i},U_{h_i}) \rightarrow A(U,U)$ as i increases, this is generally not in a one-sided way.

Indeed, it is the fact that $A^{AS}(U,U) - A^{AS}(U_h,U_h)$ is frequently negative that prompted in [9, 35] the use of $\ln(|1 - \frac{A^{AS}(U_h,U_h)}{A(U,U)}|)$ rather than $ln(1 - \frac{A^{AS}(U_h,U_h)}{A(U,U)})$.

Also, because of Equation 4.8, we do not have in general that $\ln(|1 - \frac{A^{AS}(U_h,U_h)}{A(U,U)}|)$ is a function of $U-U_h$ only, let alone an actual norm for $U-U_h$. Hence, the approach of [9, 35], although an improvement over the more basic methods presented higher, is not sufficient to assess whether a mixed finite element scheme is optimal.

4.1.2 Design of an error measure

Goals

From the previous section, it is clear that the proper procedure to assess the performance of mixed-interpolated shell finite elements should ideally satisfy the following conditions:

1. It should take into account the finite element solution – and of course the exact solution – over the *entire* structure, not just a few selected points or lines.

2. It should give quantitative results regarding the performance of the element tested. In particular, it should define a proper *norm* (see [30]) for the error. Hence, we denote this error measure by $||U - U_h||_*$ where U denotes the exact solution and U_h denotes a finite element solution. That norm should be easily related to the physical problem analyzed (i.e. we would like a physics-based norm).

3. We should be able to employ the procedure whether or not an analytical solution is available for the problems considered. Indeed the procedure should be flexible enough that it can handle arbitrary geometries, loadings, etc...

4. It should be possible to employ a single procedure to assess the performance of various element formulations, allowing easy comparison between different formulations.

5. A method that can be easily related to the assessment method already existing for displacement-based formulations is highly desirable. Of course a procedure that can be easily extended to mixed finite element formulations other than shell finite elements – such as u/p formulations for the analysis of incompressible materials and incompressible fluids – would be of great value.

6. Finally, the same norm would be used for all shell problems, regardless of their asymptotic behaviors.

Given such an error measure, the goal in developing finite elements would be to identify elements such that, for any problem with a relative thickness $\epsilon = t/L$ considered, the finite element solution U_h^ϵ and the reference solution U_{ref}^ϵ satisfy

$$\frac{||U_{ref}^\epsilon - U_h^\epsilon||_*}{||U_{ref}^\epsilon||} = Ch^k \tag{4.10}$$

for all thicknesses, with C a constant independent of the shell thickness and k the order of the complete polynomial included in the formulation, see [11]. Such a formulation would be *uniformly optimal* and would be guaranteed not to lock. Currently, there does not exist a mathematical result of uniform optimality for the MITC shell elements.

Based on these objectives, we propose a new procedure in Section 4.1.3 [8].

4.1.3 Proposed error measure

In order to make our presentation of the proposed algorithm simple, we first assume that an analytical solution of the shell problem considered is available. This requirement will be removed later on.

So for now, let us assume that we are considering a shell problem based on the Reissner-Mindlin kinematic assumption for which we know the exact analytical solution for the displacements and rotations, collectively denoted by U. For this problem we can therefore evaluate the exact strains at every point x in the solution. We denote the shell domain by Ω and the exact cartesian strains by $B(x)U(x)$ where $B(x)$ is the strain operator. We discretize this problem and solve it using a certain finite element formulation, yielding a finite element solution $U_h(x_h)$ (again, U_h denotes collectively translations and rotations) at every point of the discretized domain Ω_h. Note that because we have discretized the geometry, the finite element domain and the actual domain are different in general. Our finite element formulation allows us to calculate the cartesian strains $B_h(x_h)U_h(x_h)$ related to this solution at every point $x_h \in \Omega_h$.

As indicated earlier, since we have discretized the geometry, in general a point $x_h \in \Omega_h$ does not belong to the exact geometry, see Figure 4-1. It is however possible

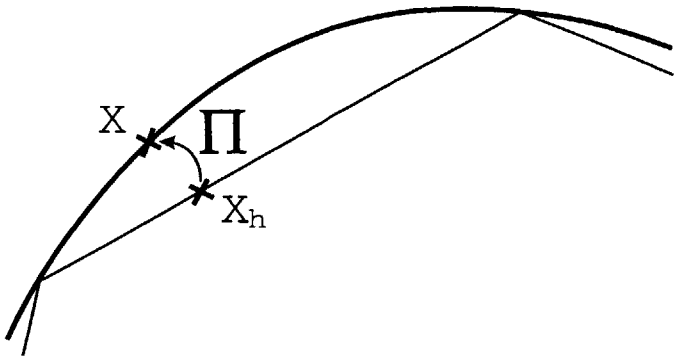

Figure 4-1: Mapping between a coarse mesh and the exact geometry. The mapping defines a bijection between the coarse mesh (straight line) and the exact geometry of the structure (curved line).

to define a one-to-one mapping between every point $x_h \in \Omega_h$ and every point $x \in \Omega$. Let us denote this mapping by Π, so that

$$\forall x \in \Omega \quad \exists! x_h \in \Omega_h \quad \text{such that} \quad x = \Pi x_h \tag{4.11}$$

It should be noted that there is not a unique way of selecting Π: proper care should therefore be taken to select a reasonable mapping. In certain analysis cases, the actual geometry of the structure can be exactly represented by the finite elements considered – for instance if we model a parabolic cylinder with 9-node quadrilateral elements – , in which case Π is the identity operator. But in general picking the mapping is a matter of engineering choice, similarly to picking a meshing scheme. This choice is usually not expressed explicitly but is always required implicitly when the finite element method is used for shell structures. In the proposed procedure, this choice needs to be expressed explicitly.

The error measure EM we propose is then simply

$$EM(U, U_h) = \frac{1}{2} \int_\Omega \Delta e^T \, C(x) \, \Delta e \; d\Omega \tag{4.12}$$

where $C(x)$ denotes the material law expressed in the cartesian coordinate system and

$$\Delta e = B(x)U(x) - B_h(\Pi^{-1}(x))U_h(\Pi^{-1}(x)) \tag{4.13}$$

In physical terms, Δe denotes the difference between the exact strains at one point of the structure and the finite element strains at the corresponding point of the mesh, while $EM(U, U_h)$ is simply the strain energy associated with this difference. That EM is the square of a norm for Δe is a classical result of mechanics and an immediate result of the material law fourth-order tensor defining a positive definite bilinear form. It is however not the square of a norm for the displacements, as shown in Appendix B where the use of the proposed error measure is demonstrated on a simple Timoshenko beam example.

Note that if we were interested in defining an error measure that is also a norm for the error in the displacements we may consider using as an alternative error measure EM' defined by $EM'(U, U_h) = EM(U, U_h) + C||U - U_h||^2_{L^2} + C'||\theta - \theta_h||^2_{L^2}$ where C and C' are constants needed for the sake of dimensional homogeneity. These constants would need to be selected carefully to assure that EM' can be used to detect locking. Also, in practice, these constants would need to be selected based on typical dimensions, material properties, etc of the problem in such a way as to assure that in numerical experiments $EM(U, U_h)$ and $C||U - U_h||^2_{L^2}$ and $C'||\theta - \theta_h||^2_{L^2}$ are of comparable magnitudes. However, in our experience, when the MITC elements are employed, the strains converge to their exact values slower than the displacements and therefore whether we include the L^2 norm of the displacements in the error measure may be of little consequence. Various norms are investigated analytically in Appendix B.

In the case where an analytical solution is not known for the problem considered, we can substitute in Equation 4.12 the strains of the exact solution with an accurate approximation of these strains. This accurate approximation can be obtained for example by solving by a finite element method the problem using a very fine mesh. Note that it is entirely possible to employ finite elements of a different type than the

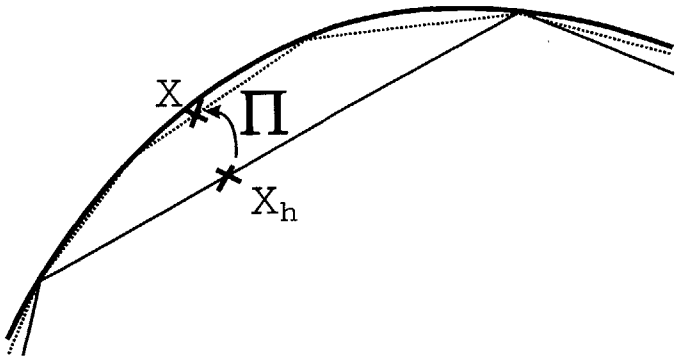

Figure 4-2: Mapping between a coarse mesh and a reference mesh. The mapping defines a bijection between the coarse mesh (solid straight line) and the reference mesh (dotted straight line). The exact geometry is also shown (curved line).

element analyzed to obtain this reference solution, provided the two finite element schemes are consistent (i.e. they tend to the same solution as the element size is reduced to zero).

Let us put this approach (when an accurate finite element solution is used in place of the exact analytical solution) in rigorous terms. There exists a mapping Π between the coarse mesh domain Ω_h and the reference fine mesh domain Ω_{ref} (see Figure 4-2). Then we use as our error estimate

$$EM(U, U_h) = \frac{1}{2} \int_{\Omega_{ref}} \Delta e^T \, C(x) \, \Delta e \;\; d\Omega_{ref} \tag{4.14}$$

where

$$\Delta e = B_{ref}(x) U_{ref}(x) - B_h(\Pi^{-1}(x)) U_h(\Pi^{-1}(x)) \tag{4.15}$$

To analyze convergence rates and locking, we propose to plot $\ln(EM(U, U_h)/E(U, U))$ versus $\ln(h)$ (we recall the notation $E(U, U) \equiv \frac{1}{2} A(U, U)$). Here again, in practice $A(U, U)$ is replaced with the energy of the numerically computed reference solution $A^{AS}(U_{ref}, U_{ref})$.

It is important to observe that when the geometry of the problem considered allows for Π to be the identity operator (i.e. the geometry is exactly represented) and a displacement-based formulation is analyzed then clearly we have $EM(U, U_h) =$

$E(U,U) - E(U_h,U_h) = E(U-U_h, U-U_h)$. Therefore in that case plotting $\ln \frac{EM(U,U_h)}{E(U,U)}$ is equivalent to plotting $ln(1 - A(U_h,U_h)/A(U,U))$. Hence in this case the proposed procedure reduces to the usual procedure employed to analyze the convergence rate of a displacement-based formulation.

4.1.4 Implementation of the proposed procedure

Our procedure to calculate error measures is summarize in flow-chart style in Figure 4-3.

General considerations

Let us assume that we have solved one problem using two separate meshes of MITC shell elements, one coarse and one very fine to be used as reference solution. In each case, we have access to all nodal displacements (by which we mean translations and rotations).

In our implementation, the mapping Π is given as follows. For every node of the reference mesh, we define the location of the corresponding point in the coarse mesh by specifying the number of the element of the coarse mesh to which this point belongs and the iso-parametric coordinates of that point. For instance, we might say that "node #12345 of the fine mesh maps to the point of iso-parametric coordinates $(0.3, 0.5)$ in element #12 of the coarse mesh".

For points of the fine mesh that are not nodes[2], we calculate the location of their mapping by extrapolation from the nodes of the fine mesh element they belong to, using the iso-parametric shape functions. For instance, let us say that the 4 nodes of a 4-node element of the fine mesh map to the points of global coordinates $(11, 11)$, $(10, 11)$, $(10, 10)$ and $(11, 10)$. Then the point of iso-parametric coordinates $(0, 1)$ in the element of the fine mesh maps to the point of coordinates $(10.5, 11)$.

By this procedure, Π is implicitly specified for all points of the reference mesh.

This mapping allows us to evaluate $EM(U, U_h)$ by way of Gaussian quadrature.

[2]In particular, for integration points

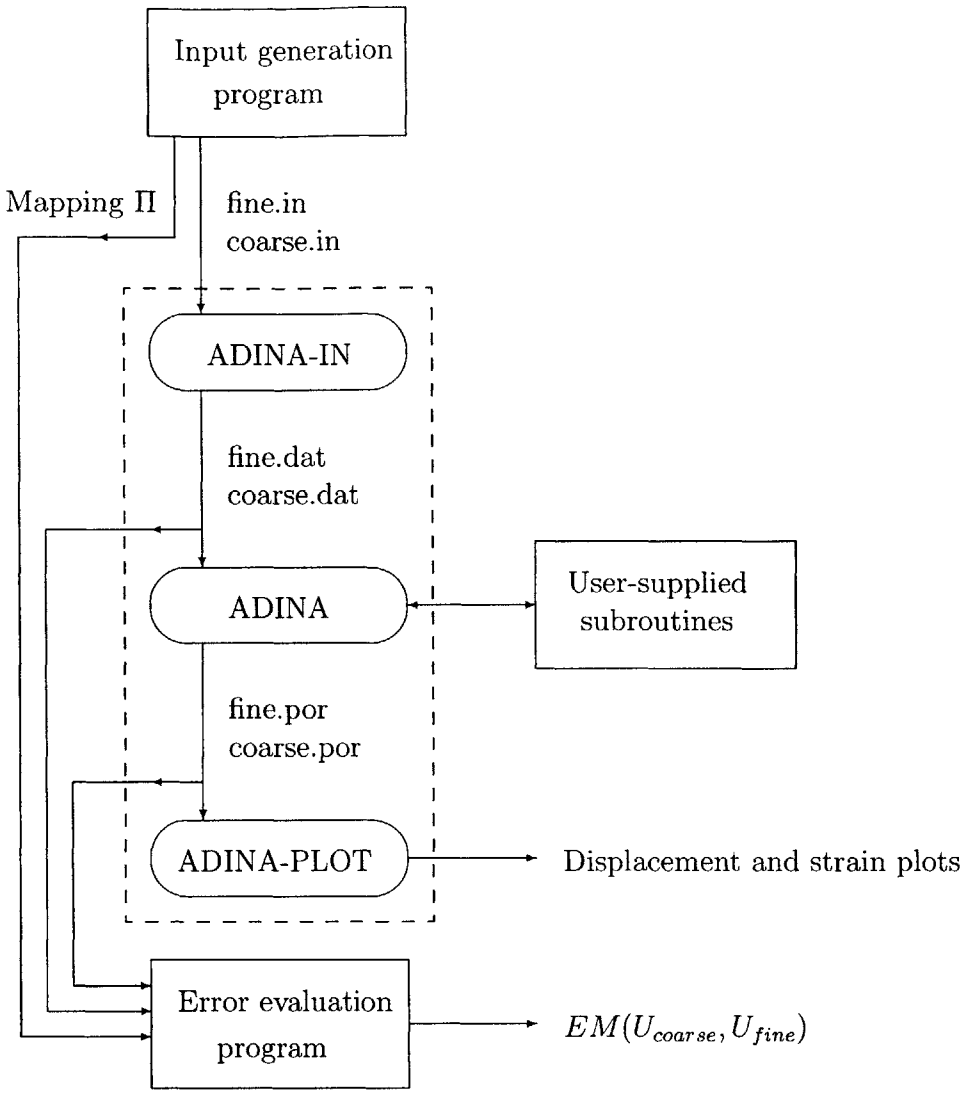

Figure 4-3: Procedure employed to evaluate error measures. We coded the input generation program, the user-supplied subroutines and the error evaluation program in FORTRAN. Our input generation program creates the input files (".in" files), which specifies the finite element problems entirely (location of all nodes, loading vectors R_{coarse} and R_{fine}, director vectors, material properties, boundary conditions,...), as well as the mapping Π. The input files are read into ADINA-IN to generate the data files (".dat" files). For each element in the meshes, ADINA passes to our user-supplied subroutines all information required to establish the element stiffness matrix. Each element stiffness matrix is established by our user-supplied subroutines and passed to ADINA which then assembles these matrices into the structure stiffness matrices K_{coarse} and K_{fine}. The problems $KU = R$ are then solved by ADINA using a sparse solver. Our user-supplied subroutines are then called again to establish the strains within each element. The solutions are output to porthole files (".por") which can be read by ADINA-PLOT to generate displacement and strain plots. The data and porthole files and the mapping Π are used as input by our error evaluation program to establish the error measure $EM(U_{coarse}, U_{fine})$.

At an arbitrary Gauss point of the reference mesh we can evaluate all cartesian finite element strains. We can then make use of Π to determine what point of the coarse mesh corresponds to that fine mesh Gauss point and evaluate the coarse solution cartesian strains there. We then subtract the two strains to form Δe, and we therefore obtain $EM(U, U_h)$ by carrying out the multiplication $\Delta e^T\ C\ \Delta e$ and looping over all Gauss points.

Since the Gaussian quadrature method only requires the calculations to be carried out at Gauss points, we could have alternatively specified the mapping for Gauss points directly, instead of specifying the mapping for nodes and then extrapolating to Gauss points.

We have mentioned that Δe is based on *cartesian* strains. These strains are used because they can easily be compared between two solutions. We would not be able to directly subtract the strains expressed in element-based coordinate systems (such as $e_{\bar{r}\bar{r}}$, $e_{\bar{s}\bar{s}}$,... see [11]) because they are expressed on different coordinate systems.

This choice of strains implies that in calculating the contribution of a given Gauss point x_{GP} to $EM(U, U_h)$ in practice we need to follow the following steps when we are using MITC shell elements:

1. We first evaluate the strains (i.e. the B_h operator) for the fine mesh in the element-based $(r, s, t) = (\xi_1, \xi_2, \xi_3)$ coordinate system because this is the coordinate system in which the tying process is done.

2. We "rotate" these strains to the global cartesian (x, y, z) coordinate system, to obtain $B_{ref}(x_{GP})U_{ref}(x_{GP})$.

3. We repeat the first two steps for the coarse mesh to obtain $B_h(\Pi^{-1}(x_{GP}))U_h(\Pi^{-1}(x_{GP}))$.

4. We express the material law tensor in the $(\bar{r}, \bar{s}, t)$ because this is the coordinate system in which the material law tensor (including the assumption of no through-thickness stress) is most readily expressed.

5. We "rotate" the material law tensor to the (x, y, z) coordinate system to obtain the C matrix.

6. We carry out the matrix multiplication $\Delta e^T\, C \Delta e$.

Finally, a critical issue in the implementation of our procedure is to assure accuracy of the error measure. For this work, we used three pieces of code:

1. An input generator: This piece of code generates all input data that is used by the finite element program, such as the coordinates of all nodes, the director vectors at all nodes, the material properties, integration schemes, types of elements used, etc. This data is then read by the ADINA code.

2. An element stiffness matrix evaluation code: The ADINA code builds the structure stiffness matrix by assembling element stiffness matrices calculated by our element stiffness matrix evaluation code. This piece of code basically reads in all the information pertaining to each element and returns the corresponding element stiffness matrix.

3. An error measure calculator: This piece of code reads in all the information generated by the solution of the problem using a coarse and a reference mesh, and from this data evaluates the error measure $EM(U_h, U_{ref})$.

All three pieces of code were written in FORTRAN, and all computations are carried out with DOUBLE PRECISION. All input data are generated with 14 digit accuracy, and the same accuracy is used throughout the element stiffness evaluation algorithm (in particular the coefficients of the assumed shape functions, the location of the Gauss points and the Gaussian weights are all supplied with at least 14 digit accuracy). Due to the number of multiplications involved in establishing the stiffness matrices, some accuracy is lost but these matrices were verified to be accurate to 12 digits. This level of accuracy was confirmed by comparing the stiffness matrices obtained using our code with stiffness matrices obtained by two separate, entirely independent codes used as a reference. One of these codes was written in FORTRAN by an independent researcher, the other was written by ourselves in the Maple computing language. Considering that our reference solutions in the following section are based on meshes including on the order of 10^5-10^6 degrees of freedom, it can be roughly estimated that,

including round-off errors introduced by the solution of the system of equations, we can count on nodal displacements being known with 8 digit accuracy. In the error measure calculator, all computations are carried out with DOUBLE PRECISION accuracy, with all data being read with 14 digit accuracy. As a result, the error measure $EM(U_h, U_{ref})$ is evaluated with 7 digit accuracy (an order of accuracy is lost due to the computations).

This level of accuracy should be compared to the error introduced by replacing the exact solution of the problem by an approximate solution computed on a very fine mesh. In our experience (see Section 4.2), depending on the type of element used our reference solutions can be considered accurate up to between the fifth digit (worst case) and seventh digit (best case). Hence, the error in evaluating EM due to finite precision arithmetic is negligible.

Error plotting

It is also possible to employ the basic approach (steps 1 through 6) described above to generate a plot of the error density $\Delta e^T\ C\ \Delta e$ over the reference mesh, allowing to determine in what area of the structure the coarse mesh solution differs significantly from the reference solution. No such possibility exists in the context of the traditional performance assessment procedures described in Section 4.1.1.

Even more detailed information can be plotted: by replacing Δe by $\Delta e_{membrane}$ (respectively Δe_{shear}, $\Delta e_{bending}$) defined as the difference between the membrane (resp. shear, bending) strains of the coarse and reference solutions expressed in the cartesian coordinate system and plotting ${\Delta e_{membrane}}^T\ C \Delta e_{membrane}$ (respectively ${\Delta e_{shear}}^T\ C \Delta e_{shear}$, ${\Delta e_{bending}}^T\ C \Delta e_{bending}$) we can determine how each part of the strain tensor converges at every point of the structure. This can be used to determine whether a given formulation features membrane locking versus shear locking, etc.

To obtain displacement and strain plots, ADINA PLOT is used.

Convergence analysis

Clearly the main interest of the proposed procedure lies in its use to assess the convergence rates and the presence of locking in new or existing finite element schemes.

Obviously, in order to assure the accuracy of our procedure, we need to employ the finest possible mesh to establish our reference solution. As far as coarse meshes are concerned, we would like to employ the largest possible range of element sizes. It should be noted however that so as to maintain the accuracy of the method we need to make sure that the reference solution is significantly more accurate than the solution obtained using the finest of the coarse meshes. Hence the finest coarse mesh should be significantly coarser than the reference mesh. In our computations, we empirically determined that to assure accuracy we should not use coarse meshes for which the element size h is smaller than $3h_{ref}$.

As an example, in the study of the hyperboloid of Section 4.2.1 one of the sequences of uniform meshes we use is as follows: 6×6, 12×12, 18×18, 24×24, with the reference being computed on a 72×72 mesh (see Figure 4-6 for a typical mesh).

In any case however, we should always keep in mind that our error measure is only as good as the reference solution we employ, and it is therefore very important to determine the accuracy of the reference solutions we use.

4.2 Test problems

4.2.1 Clamped hyperboloid

The first problem considered is described in Figure 4-4.

The mid-surface of this structure is described by the equation

$$x^2 + z^2 = 1 + y^2 \tag{4.16}$$

i.e. the mid-surface is a hyperboloid of one sheet, a doubly-ruled surface. We impose clamped boundary conditions at both ends $y = 1$ and $y = -1$ and hence we can use

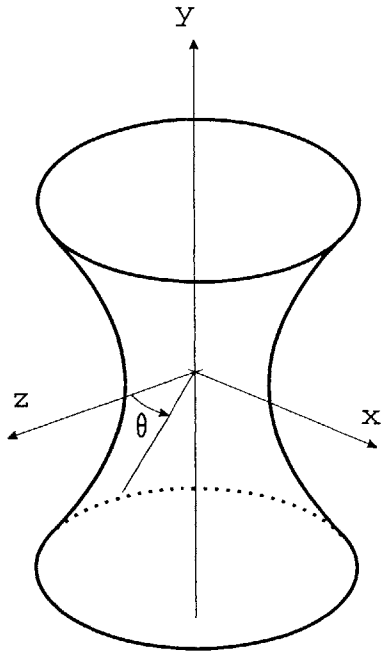

Figure 4-4: Hyperboloid's mid-surface geometry. The polar angle θ used to describe the loading is indicated.

$L = 1$. The loading imposed is the periodic pressure

$$p(\theta) = P_0 cos(2\theta) \tag{4.17}$$

where θ denotes the polar angle, as shown in Figure 4-4. Using symmetries, the analysis was performed using one eighth of the structure. Note that the analysis can also be carried out on one sixteenth of the structure using antisymmetry conditions at $\theta = 45^o$.

This problem is similar to the clamped cylinder problem which is frequently used in testing shell finite element formulation. That problem is well known to be membrane-dominated and to feature boundary layers in the regions near the clamped boundary conditions.

We introduced this new test because unlike the clamped cylinder problem, the hyperboloid problem has non-zero Gaussian curvature, making it a more general and also a tougher problem to solve. Indeed the geometry of the mid-surface does not

allow to align the sides of quadrilateral elements with the asymptotic lines. It is known that finite elements perform better when their sides can be oriented that way (see [19]). In industrial applications though it is generally not possible to align the mesh with the asymptotic lines and therefore we should not use this feature in our tests.

The first step with a new problem like this one consists in determining the asymptotic behavior. We follow here the method presented in [40]: we study the behavior of $\bar{\rho}$ defined as

$$\bar{\rho} = \frac{log(E_h(t_{i+1})) - log(E_h(t_i))}{log(t_i) - log(t_{i+1})} \tag{4.18}$$

where $E_h(t_i)$ denotes the finite element strain energy with the thickness t_i. For our study, we use the sequence of thicknesses $t_i = 10^{-i}$ with $i \in \{2,3,4,5,6,7,8\}$. For each thickness, the problem is solved using a mesh consisting of 72×72 MITC16 shell elements. A boundary layer is present along the clamped edge, see Figure 4-5. Due to the presence of this layer, we use locally refined meshes (also referred to as "graded meshes") in some of our numerical experiments, and uniform meshes in others.

In our mesh grading scheme, the modelled geometry is subdivided into two regions: one band of width $6\sqrt{t_i}$ along the clamped boundary condition, and the remainder of the geometry. Each of these two regions is then meshed using a uniform mesh, see Figure 4-7. We used the same number of elements in each of the two regions. Note that the width $6\sqrt{t_i}$ is selected based on the theoretical knowledge that along a line that is not an asymptotic line layer thicknesses vary as $\sqrt{t}$, and the constant 6 is chosen based on numerical experiments. For each thickness, the smoothness of the numerical solution is checked. It is known that if $\bar{\rho}$ goes to 1 as i is increased then the problem considered is membrane-dominated. The results, obtained with 72×72 element MITC16 meshes and presented in Table 4.1, show that this problem is also membrane-dominated.

Alternatively, we can also determine that this test problem is membrane-dominated by directly considering the behavior of the ratio of the membrane and shear energy of the finite element solution to the total energy of the finite element solution for a

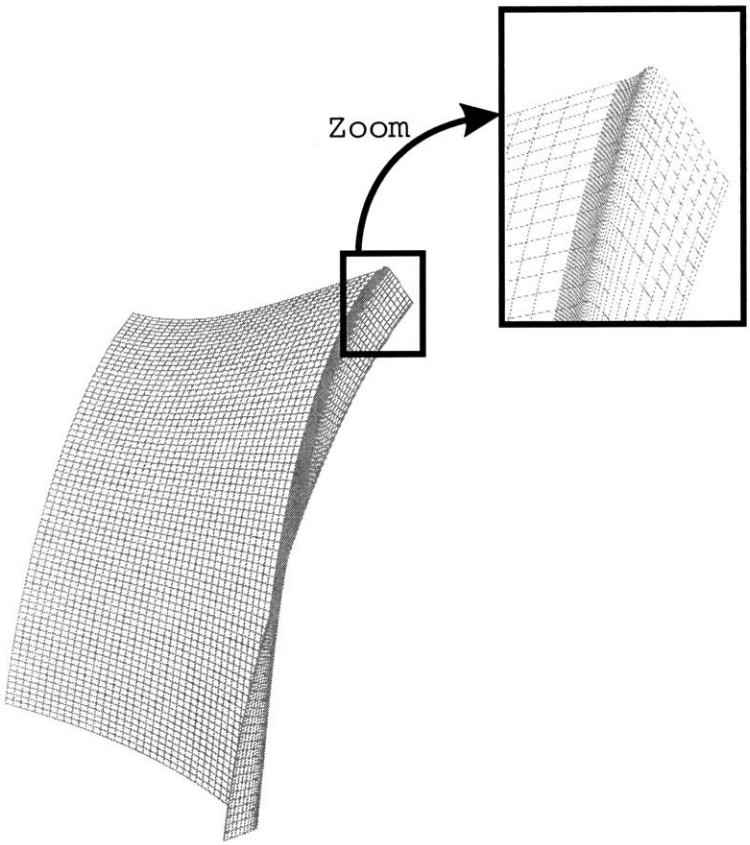

Figure 4-5: Deformation of the clamped hyperboloid. The boundary layer along the clamped edge is clearly visible. Graded 72×72 MITC16 mesh, $t = 0.0001$.

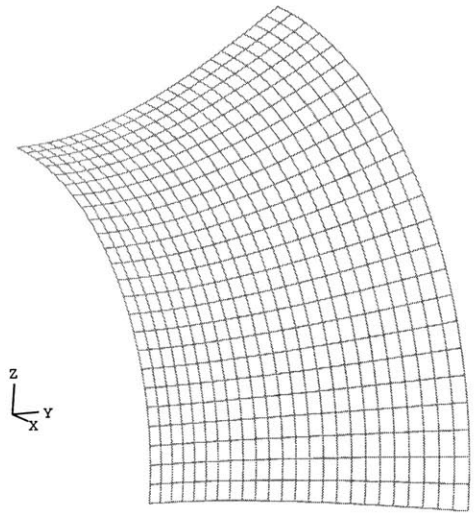

Figure 4-6: Hyperboloid: example of a uniform mesh

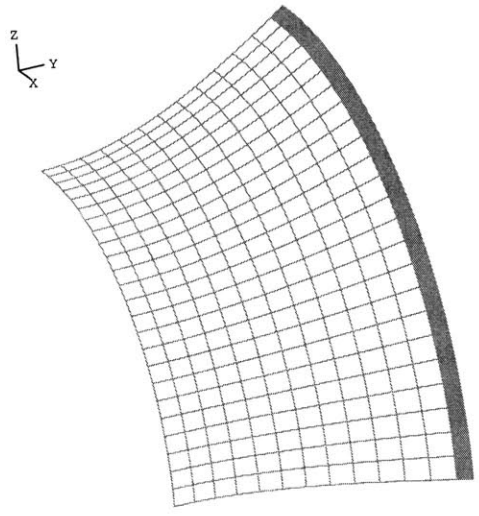

Figure 4-7: Hyperboloid: example of a graded mesh

Table 4.1: Asymptotic behavior of the clamped hyperboloid problem.

Thickness	Strain energy	$\bar{\rho}$
10^{-2}	$0.539187\ 10^{3}$	
		1.0465
10^{-3}	$0.600115\ 10^{4}$	
		1.0134
10^{-4}	$0.618988\ 10^{5}$	
		1.00412
10^{-5}	$0.624889\ 10^{6}$	
		1.00129
10^{-6}	$0.626748\ 10^{7}$	
		1.000406
10^{-7}	$0.627335\ 10^{8}$	
		1.000128
10^{-8}	$0.627521\ 10^{9}$	

number of thicknesses. The membrane and shear energy is easily evaluated numerically by employing one point Gaussian integration through the thickness instead of two point integration. The ratio is observed to go to 1 as the thickness goes to zero, which again indicates that the problem is membrane-dominated.

4.2.2 Free hyperboloid

The second problem is also based on the geometry described in Figure 4-4 and the previous section, and the loading is also identical. However, instead of the top and bottom ends ($|y| = 1$) being clamped, in this case they are left free. Again, using symmetries, it is possible to reduce the analysis to one eighth of the structure.

This problem is similar to the free cylinder problem which is frequently used in testing shell finite element formulation. That problem is known to be bending-dominated.

Similarly to the clamped hyperboloid, we introduced this new test because un-

Table 4.2: Asymptotic behavior of the free hyperboloid problem.

Thickness	Strain energy	$\bar{\rho}$
10^{-2}	$0.4528376142\ 10^{6}$	
		2.995898782
10^{-3}	$0.4485814136\ 10^{9}$	
		2.999941952
10^{-4}	$0.4485214602\ 10^{12}$	
		2.999981403
10^{-5}	$0.4485022539\ 10^{15}$	

like the free cylinder problem, the free hyperboloid problem has non-zero Gaussian curvature, making it a more general and also a tougher problem to solve.

The asymptotic behavior of this problem is again determined by employing the approach presented in [40]. The results presented in Table 4.2 show that the free hyperboloid problem is bending-dominated.

Again, alternatively, we can also determine that this test problem is bending-dominated by directly considering the behavior of the ratio of the membrane and shear energy of the finite element solution to the total energy of the finite element solution for a number of thicknesses. The ratio is observed to go to 0 as the thickness goes to zero, which again indicates that the problem is bending-dominated.

4.2.3 Scordelis-Lo roof

The Scordelis-Lo roof problem was described in Section 2.2.1. This problem is known to be of mixed nature: it is proven analytically in [22, 13] that the scaling factor for this problem is $\rho = 1.75$.

In general however we can not expect to be able to obtain analytical values for ρ for complex problems featuring a mixed asymptotic behavior and we must therefore rely on numerically-evaluated values. It is therefore important to establish how accurate these estimates can be expected to be. Of course it is useful to give some guidelines

on how to obtain more accurate approximate values for ρ. A previously-reported numerically-obtained value for ρ is 1.72 (reported in [40], see also [2]). This value was obtained through the use of uniform meshes of 72×72 MITC4 elements. Here we investigate the use of the MITC4, MITC9 and MITC16 elements combined with graded meshes.

In this problem, a boundary layer develops at the free edge of the structure, as shown in Figure 2-4. The width of this boundary layer is proportional to the fourth root of the thickness $t^{1/4}$ as reported in [40] and in accordance with Table 2.1. We make use of that known feature of the solution by meshing the structure appropriately: similarly to what we did in Section 4.2.1, we subdivide the geometry into two regions: one band of width $5t^{1/4}$ along the free edge (the constant 5 was chosen based on experiments), and the remainder of the geometry. Each of these two regions is then meshed using a uniform mesh. We use the same number of elements in each of the two regions.

We show the results of our calculations with the MITC4 (respectively MITC9 and MITC16) in Table 4.3 (respectively Table 4.4 and Table 4.5). The values for the strain energies are based on a Young's modulus of $E = 2.10^{11}$ and a unit density for the loading. Obviously, the values of these parameters do not affect the values of $\bar{\rho}$ since the problem is linear in these parameters. The Poisson ratio is $\nu = 1/3$.

Tables 4.3, 4.4 and 4.5 indicate that there is generally good agreement between the numerically evaluated values of $\bar{\rho}$ and the exact limit value $\rho = 1.75$. We note that the MITC9 and MITC16 elements give markedly better results than the MITC4 elements. Indeed, when MITC4 meshes are used we do not observe convergence of $\bar{\rho}$ to the limit value of 1.75 whereas with the MITC9 and MITC16 elements this convergence is clear, even with the coarse meshes. One reason for the lesser predictive ability of the MITC4 elements in this problem may be due to the fact that they cannot approximate the geometry quite as accurately as the other elements.

Based on these experiments, we see the advantage of using refined meshes that take into account the presence of boundary and internal layers. When these layers are properly meshed, we managed to obtain values of $\bar{\rho}$ that clearly tend to the theoretical

Table 4.3: Asymptotic behavior of the Scordelis-Lo roof problem modelled with the MITC4 element.

Thickness	Strain energy 48×48 mesh	$\bar{\rho}$	Strain energy 192×192 mesh	$\bar{\rho}$
10^{-3}	$0.4938160272\ 10^{1}$		$0.4958376653\ 10^{1}$	
		1.722804494		1.736533671
10^{-4}	$0.2608372878\ 10^{3}$		$0.2703168919\ 10^{3}$	
		1.699225692		1.738856762
10^{-5}	$0.1304954495\ 10^{5}$		$0.1481596513\ 10^{5}$	
		1.634801963		1.736058214
10^{-6}	$0.5628560401\ 10^{6}$		$0.8068413768\ 10^{6}$	

Table 4.4: Asymptotic behavior of the Scordelis-Lo roof problem modelled with the MITC9 element.

Thickness	Strain energy 24×24 mesh	$\bar{\rho}$	Strain energy 96×96 mesh	$\bar{\rho}$
10^{-3}	$0.4931704257\ 10^{1}$		$0.4960927023\ 10^{1}$	
		1.737552061		1.737565383
10^{-4}	$0.2694939907\ 10^{3}$		$0.2710991906\ 10^{3}$	
		1.742100294		1.742088308
10^{-5}	$0.1488159153\ 10^{5}$		$0.149698183\ 10^{5}$	
		1.74538403		1.745223152
10^{-6}	$0.828005883\ 10^{6}$		$0.8326062782\ 10^{6}$	

Table 4.5: Asymptotic behavior of the Scordelis-Lo roof problem modelled with the MITC16 element.

Thickness	Strain energy 18×18 mesh	$\bar{\rho}$	Strain energy 72×72 mesh	$\bar{\rho}$
10^{-3}	$0.4962325778\ 10^{1}$		$0.4961039829\ 10^{1}$	
		1.737573087		1.737564775
10^{-4}	$0.2711804386\ 10^{3}$		$0.2711049757\ 10^{3}$	
		1.742106457		1.742060303
10^{-5}	$0.149749305\ 10^{5}$		$0.1496917245\ 10^{5}$	
		1.745455704		1.746848934
10^{-6}	$0.8333367221\ 10^{6}$		$0.835692960\ 10^{6}$	

limit of 1.75 even with fairly coarse meshes.

4.3 Consistency results

The first use we can make of our error measure is to check the consistency of the MITC family of shell elements. In [17], a patch test [11] was conducted, and it was shown that the MITC9 and MITC16 elements passed approximately the plate in tension patch test, while this same test was passed by the MITC4 element, as reported in [24]. Our own patch tests confirmed these results. Note that, for shells, patch tests are very limited since only one geometry (plate) can be considered.

However, it is important to note that passing all applicable patch tests is a sufficient but not necessary condition for consistency. Indeed, despite the fact that the MITC elements have been used extensively in research and industry for years, we do not know of any problem which would indicate that the MITC elements are not consistent.

Since the plate patch tests (tension, shear, bending) are not passed exactly by the higher-order MITC elements (inaccuracy of about 3% were observed in our tests), we need to look for weaker proofs of consistency.

If a finite element formulation is consistent with the basic shell model of reference [21] then necessarily a very fine mesh of elements following that formulation will give a strain energy close to that of the exact solution. The difficulty in using this property to test for consistency – besides the fact that it is only a necessary condition for consistency – is that while we need to prove consistency for complex geometries and loading conditions, usually analytical solutions for such problems are not available and therefore we do not know the strain energy of the exact solution. To generate a reference strain energy we can however make use of the fact that for a displacement-based formulation, we have

$$E_h - E_0 \simeq Ch^{2k} \tag{4.19}$$

where E_h is the strain energy of the finite element solution obtained using elements of typical size h, E_0 is the strain energy of the exact solution and k is the degree of the complete polynomial included in the formulation (see [11]). We can make use of Equation 4.19 to evaluate E_0 from the strain energies E_{h1} and E_{h2} in two finite element models with typical element sizes h_1 and h_2 through the formula (derived directly from Equation 4.19):

$$E_0 = \frac{1}{(\frac{h_1}{h_2})^{2k} - 1}[(\frac{h_1}{h_2})^{2k} E_{h2} - E_{h1}] \tag{4.20}$$

In Table 4.6, we report the reference energy calculated by use of the extrapolation formula in Equation 4.20 by use of a 24×24 element and a 72×72 element QUAD16 model of the clamped hyperboloid problem. This same table also reports the strain energies obtained with fine meshes of MITC4, MITC9 and MITC16 elements. For the MITC4 (resp. MITC9, MITC16) element, we use a 192×192 (resp. 96×96, 72×72) element graded mesh. The strain energies obtained with the MITC elements, considering t as small as 10^{-5}, agree with the extrapolated reference strain energy up to at least the third digit, and especially for the higher-order elements frequently significantly better.

As a more refined approach, we now make use of our error measure by evaluating in Equation 4.14 the reference strain $e_{ref} = B_{ref} U_{ref}$ by use of a very fine mesh of

Table 4.6: Clamped hyperboloid problem: consistency.

t	Extrapolated energy using QUAD16 elements	MITC4	MITC9	MITC16
10^{-2}	$0.53918719.10^3$	$0.53913610.10^3$	$0.53918715.10^3$	$0.53918722.10^3$
10^{-3}	$0.60011490.10^4$	$0.60002983.10^4$	$0.60011496.10^4$	$0.60011498.10^4$
10^{-4}	$0.61898762.10^5$	$0.61878678.10^5$	$0.61898766.10^5$	$0.61898767.10^5$
10^{-5}	$0.62488944.10^6$	$0.62436470.10^6$	$0.62488945.10^6$	$0.62488946.10^6$
10^{-6}	$0.62760826.10^7$	$0.62566295.10^7$	$0.62674820.10^7$	$0.62674820.10^7$

displacement-based elements and $e_h = B_h U_h$ with a number of coarse meshes made of MITC elements. If the MITC elements yield a solution that converges to the solution of the basic shell model of [21], then the error measure must go to zero as the MITC mesh is refined. Obviously, we would also like to observe the error measure converge with the optimal convergence order allowed by the interpolation orders of each element[3]. The numerical results are listed in Table 4.7 and Figure 4-8 plots the relative consistency measure $CM(U_{ref}, U_h) = EM(U_{ref}, U_h)/E(U_{ref}, U_{ref})$ in terms of the typical element size h. Note that a sufficiently accurate solution could not be obtained with the displacement-based QUAD4 element in this problem[4]. Figure 4-8 shows that the optimal order of convergence is essentially observed for the two elements considered since all curves have essentially the optimal slope. We notice some tapering of the curves as the typical element size h goes to zero. This is attributable to the fact that our reference solutions are obtained numerically and do not coincide perfectly with the exact solution of the basic shell model.

[3]i.e. for the MITC4 (respectively MITC9 and MITC16) element, the optimal order of convergence is 2 (respectively 4 and 6).

[4]How accurate a solution obtained with a displacement-based element is can be determined by comparing its strain energy to the extrapolated strain energy given in Table 4.6.

Table 4.7: Clamped hyperboloid problem: consistency measures $EM(U_{ref}, U_h)$ and reference energies $E(U_{ref}, U_{ref})$. The meshes employed are as described in Figure 4-7 with $w = 6\sqrt{t}$. The reference strain energy corresponding to each pair of element and thickness is also listed. Reference solutions are obtained using a 96×96 mesh of QUAD9 elements (respectively 72×72 mesh of QUAD16 elements).

t	N	MITC9	t	N	MITC16
	8	$0.36157456.10^{1}$		6	$0.53809780.10^{0}$
	16	$0.2729640.10^{0}$		12	$0.74511808.10^{-2}$
10^{-2}	24	$0.7748706.10^{-1}$	10^{-2}	18	$0.76200790.10^{-3}$
	32	$0.45843046.10^{-1}$		24	$0.22847192.10^{-3}$
Ref. Energy		$0.53915455.10^{3}$	Ref. Energy		$0.53918765.10^{3}$
	8	$0.11536674.10^{2}$		6	$0.16566580.10^{1}$
	16	$0.11261795.10^{1}$		12	$0.23023926.10^{-1}$
10^{-3}	24	$0.56751889.10^{0}$	10^{-3}	18	$0.27714610.10^{-2}$
	32	$0.48634601.10^{0}$		24	$0.12663554.10^{-2}$
Ref. Energy		$0.60006837.10^{4}$	Ref. Energy		$0.60011489.10^{4}$
	8	$0.41491546.10^{2}$		6	$0.54423253.10^{1}$
	16	$0.44159542.10^{1}$		12	$0.80471268.10^{-1}$
10^{-4}	24	$0.25293664.10^{1}$	10^{-4}	18	$0.11566017.10^{-1}$
	32	$0.22786689.10^{1}$		24	$0.24927619.10^{-2}$
Ref. Energy		$0.6189652.10^{5}$	Ref. Energy		$0.61898762.10^{5}$
	8	$0.19032766.10^{3}$		6	$0.19766029.10^{2}$
	16	$0.17719283.10^{2}$		12	$0.30625693.10^{0}$
10^{-5}	24	$0.90007180.10^{1}$	10^{-5}	18	$0.46218727.10^{-1}$
	32	$0.77658352.10^{1}$		24	$0.24927619.10^{-1}$
Ref. Energy		$0.62488197.10^{6}$	Ref. Energy		$0.62488944.10^{6}$
	8	$0.11877174.10^{4}$		6	$0.88822782.10^{2}$
	16	$0.92923590.10^{2}$		12	$0.14295396.10^{1}$
10^{-6}	24	$0.35649103.10^{2}$	10^{-6}	18	$0.19221583.10^{0}$
	32	$0.26862169.10^{2}$		24	$0.87288115.10^{-1}$
Ref. Energy		$0.62674582.10^{7}$	Ref. Energy		$0.62674820.10^{7}$

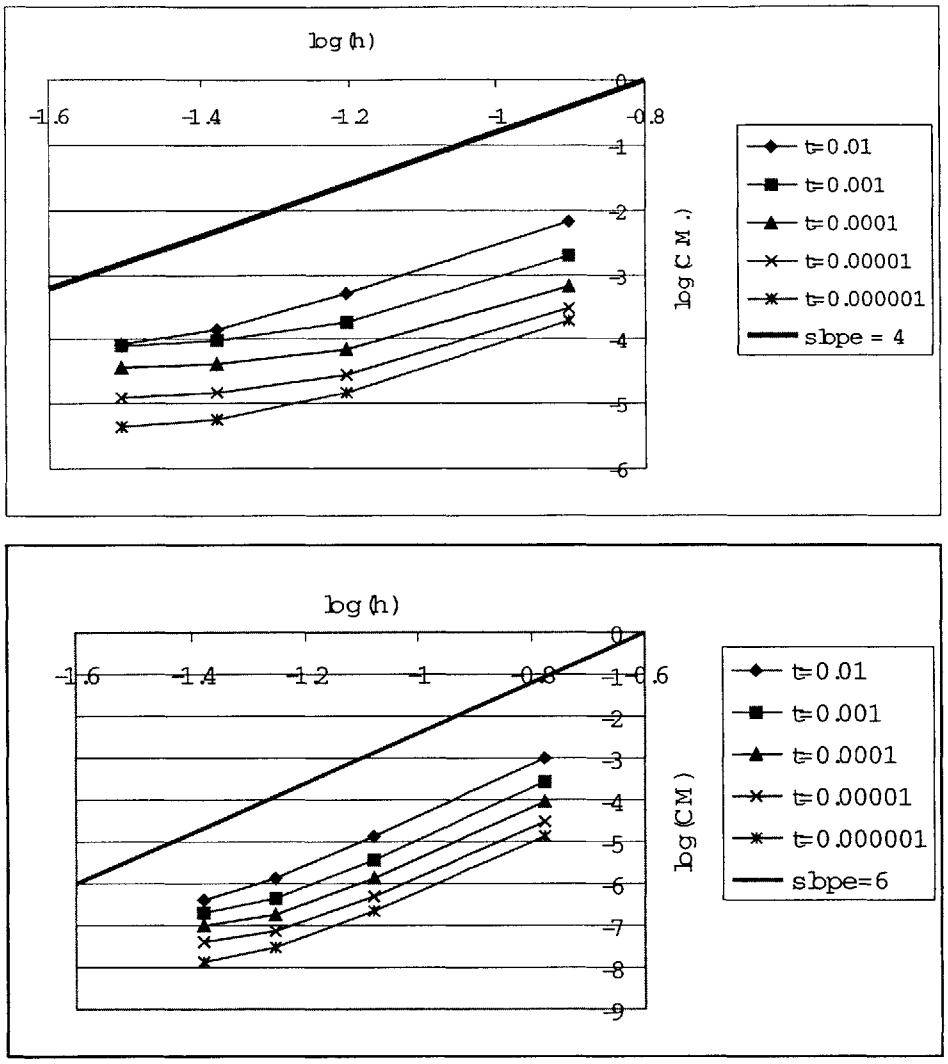

Figure 4-8: Clamped hyperboloid: consistency. Graded meshes are employed. Top to bottom: MITC9, MITC16. For 4-node elements accurate enough reference solutions can not be reached with the QUAD4 example. $C.M.$ denotes the relative convergence measure, i.e. $C.M. = \frac{\int_\Omega \Delta e^T C \Delta e d\Omega}{E(U_{ref}, U_{ref})}$. The reference solutions are established with QUAD9 and QUAD16 elements.

4.4 Error measure results

4.4.1 Introduction to the convergence results

In this section, we use the error measure presented in Section 4.1.3 to assess the convergence of the quadrilateral MITC elements.

Since we have established through our numerical experiments of Section 4.3 that the MITC elements are consistent with the mathematical model, we can use these elements to establish our reference solutions. This is particularly important for two reasons. First, we have mentioned in the consistency experiments of Section 4.3 that it was not possible to obtain a very accurate reference solution using the QUAD4 element for the clamped hyperboloid problem. Second, considering now the free hyperboloid, we know that we must expect severe locking due to the bending-dominated nature of the problem. Displacement-based elements can not be used to establish an accurate reference solution in this case.

For these two problems, and each of the three MITC elements, we employ a highly refined mesh to establish a reference solution and coarse meshes to assess the convergence. For the MITC4 element, the coarse meshes consist of 24×24, 32×32, 48×48 and 64×64 elements, and the reference solution is established with a 192×192 element mesh. For the MITC9 element, the coarse meshes consist of 8×8, 16×16, 24×24 and 32×32 elements, and the reference solution is established with a 96×96 element mesh. For the MITC16 element, the coarse meshes consist of 6×6, 12×12, 18×18 and 24×24 elements, and the reference solution is established with a 72×72 element mesh.

For each problem and each element, we employ two separate meshes: a uniform mesh, see Figure 4-6, and a locally refined mesh, where again we use the refinement method presented in Figure 4-7 with the width of the refined regions equal to $6\sqrt{t}$ (for the clamped condition) and $0.5\sqrt{t}$ (for the free condition).

In each case, we plot the relative error measure $RE(U_{ref}, U_h) = \frac{EM(U_{ref}, U_h)}{E(U_{ref}, U_{ref})}$ against the typical element size $h = 1/N$ as the mesh is refined for the thicknesses $t =$

10^{-i} with $i > 1$ [5]. If an element provides uniform optimal convergence, the curves corresponding to the different thicknesses will all be parallel to each other and have the optimal slope permitted by the order of their interpolation spaces[6], and there would be little to no upwards vertical shifting of the curves as thickness is reduced (see Equation 4.10). If the curves do not have the optimal slope, we conclude that the convergence order is not optimal. If there is some upwards shifting of the curves, we conclude that the convergence is not uniform.

It should be noted that because of the very nature of the benchmark problems selected, the sides of the elements do not coincide with the asymptotic lines of the mid-surface. The fact that meshes not aligned with the asymptotic lines, the anticlastic nature of the geometry of the mid-surface and the presence of boundary layers combine to make these very tough tests [7].

4.4.2 Clamped hyperboloid

Table 4.8 lists the values of the error measure EM calculated for the clamped hyperboloid modelled with uniform meshes, as well as the strain energies of the reference solutions. The relative errors RE are shown in Figure 4-9. We observe that for all three elements studied the convergence order lowers (the curves "flatten out") as the shell thickness is reduced and there is some upwards shifting.

Table 4.9 lists the values of the error measure EM calculated for the clamped hyperboloid modelled with locally refined meshes, as well as the strain energies of the

[5] Of course below a certain thickness it is not possible to solve the finite element problem as the stiffness matrices becomes ill-conditioned, leading to instabilities in the numerical solution or solver failure. We report here all results that could be obtained without ill-conditioning occurring.

[6] As mentioned earlier, for the MITC4 which can represent linear displacements exactly a slope of 2 would be optimal, for the MITC9 which can represent quadratic displacements exactly a slope of 4 would be optimal and for the MITC16 which can represent cubic displacements a slope of 6 would be optimal

[7] Using tough tests to evaluate the performance of a formulation is necessary for two reasons. First, we want to really challenge the formulation to determine what the worst possible performance of the formulation is. Secondly, we want the discrepancy between the solutions obtained with coarse meshes to be significantly different from the reference solution. If our coarse solutions are too close to the reference solution, random noise due to numerical factors (in particular roundoff errors and inaccuracies introduced during the inversion of the system of equations, see Section 4.1.4) can become dominant, making any interpretation of the convergence curves impossible.

Table 4.8: Clamped hyperboloid problem: error measures $EM(U_{ref}, U_h)$ and reference energies $E(U_{ref}, U_{ref})$ with uniform mesh. Reference solutions for MITC4 (respectively MITC9, MITC16) elements are obtained using a 192×192 (respectively 96×96, 72×72) MITC4 (respectively MITC9, MITC16) mesh.

t	N	MITC4	t	N	MITC9	t	N	MITC16
	24	$0.39341768.10^{1}$		8	$0.18495199.10^{1}$		6	$0.18020321.10^{0}$
	32	$0.21898101.10^{1}$		16	$0.11912044.10^{0}$		12	$0.24889979.10^{-2}$
10^{-2}	48	$0.93953547.10^{0}$	10^{-2}	24	$0.23393160.10^{-1}$	10^{-2}	18	$0.27922297.10^{-3}$
	64	$0.50124749.10^{0}$		32	$0.73429880.10^{-2}$		24	$0.82933440.10^{-4}$
Ref. Energy		$0.53914225.10^{3}$	Ref. Energy		$0.53918719.10^{3}$	Ref. Energy		$0.53918722.10^{3}$
	24	$0.11388235.10^{3}$		8	$0.11243278.10^{3}$		6	$0.73408903.10^{2}$
	32	$0.66835353.10^{2}$		16	$0.27308241.10^{2}$		12	$0.71402511.10^{1}$
10^{-3}	48	$0.29293179.10^{2}$	10^{-3}	24	$0.69269992.10^{0}$	10^{-3}	18	$0.75797627.10^{0}$
	64	$0.15680075.10^{2}$		32	$0.2258505.10^{1}$		24	$0.12476850.10^{0}$
Ref. Energy		$0.59999325.10^{4}$	Ref. Energy		$0.60011407.10^{4}$	Ref. Energy		$0.60011495.10^{4}$
	24	$0.13752604.10^{4}$		8	$0.11211661.10^{4}$		6	$0.76123636.10^{3}$
	32	$0.99916806.10^{3}$		16	$0.53468970.10^{3}$		12	$0.40066573.10^{3}$
10^{-4}	48	$0.65215106.10^{3}$	10^{-4}	24	$0.37208383.10^{3}$	10^{-4}	18	$0.25017209.10^{3}$
	64	$0.42797645.10^{3}$		32	$0.24657007.10^{3}$		24	$0.13141655.10^{3}$
Ref. Energy		$0.61864817.10^{5}$	Ref. Energy		$0.61897481.10^{5}$	Ref. Energy		$0.61898155.10^{5}$
	24	$0.16137350.10^{5}$		8	$0.14648218.10^{5}$		6	$0.10231835.10^{5}$
	32	$0.11248242.10^{5}$		16	$0.59562424.10^{4}$		12	$0.40508672.10^{4}$
10^{-5}	48	$0.66295506.10^{4}$	10^{-5}	24	$0.35484599.10^{4}$	10^{-5}	18	$0.25014217.10^{4}$
	64	$0.44711344.10^{4}$		32	$0.25148014.10^{4}$		24	$0.18719914.10^{4}$
Ref. Energy		$0.62398674.10^{6}$	Ref. Energy		$0.62481284.10^{6}$	Ref. Energy		$0.62488216.10^{6}$
	24	$0.17018021.10^{6}$		8	$0.15733300.10^{6}$		6	$0.11474229.10^{6}$
	32	$0.12021244.10^{6}$		16	$0.67745155.10^{5}$		12	$0.48798593.10^{5}$
10^{-6}	48	$0.71052354.10^{5}$	10^{-6}	24	$0.39794749.10^{5}$	10^{-6}	18	$0.28451718.10^{5}$
	64	$0.47469333.10^{5}$		32	$0.26327434.10^{5}$		24	$0.18888280.10^{5}$
Ref. Energy		$0.62507615.10^{7}$	Ref. Energy		$0.62609621.10^{7}$	Ref. Energy		$0.62674820.10^{7}$

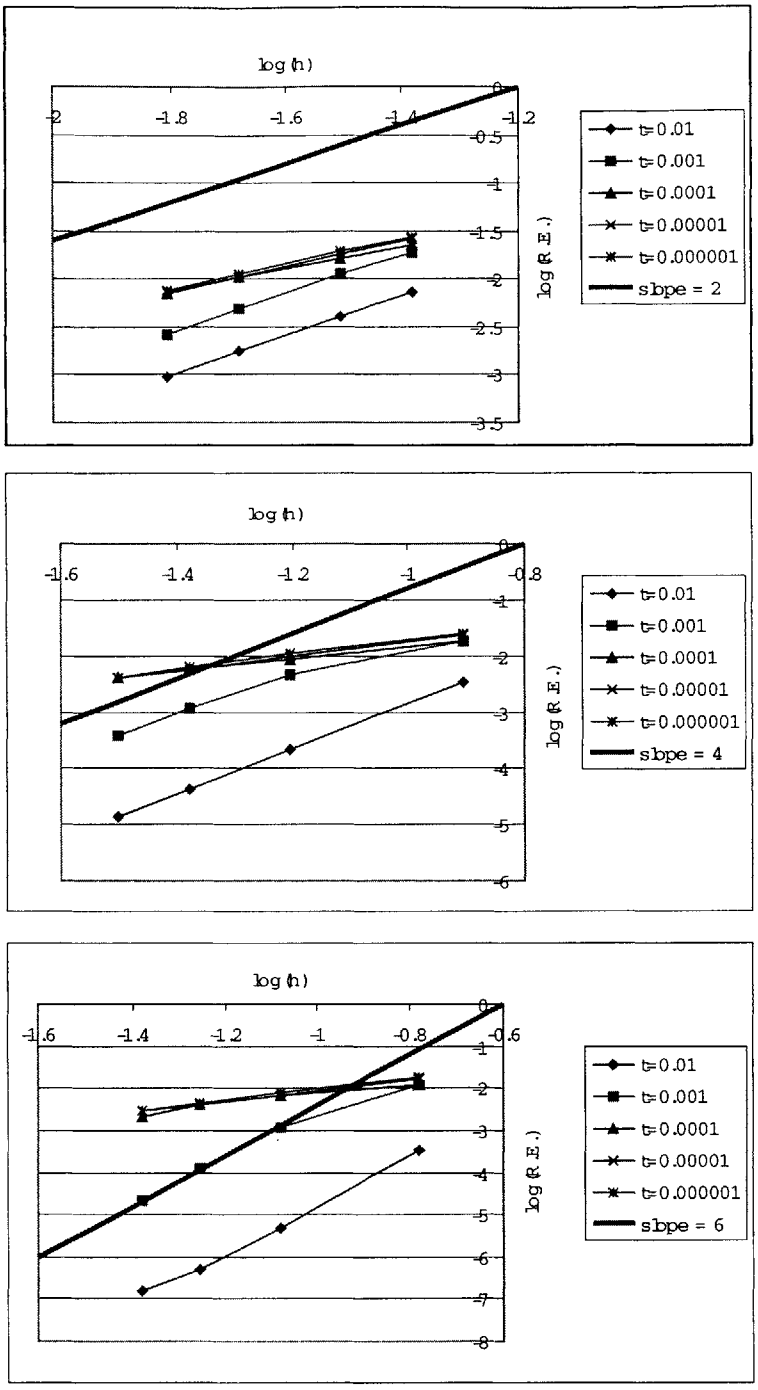

Figure 4-9: Clamped hyperboloid modelled with uniform meshes: convergence. Top to bottom: MITC4, MITC9, MITC16. The reference solutions are established using very fine meshes of the same MITC elements.

reference solutions. The relative errors RE are shown in Figure 4-10. We observe that for all three elements studied the convergence order remains constant and optimal as the shell thickness is reduced and there is some minor *downwards* shifting of the curves indicating that the elements actually perform slightly better at smaller thicknesses. This downwards shifting is probably due to the fact that as the thickness is reduced, an increasing fraction of the total strain energy comes from membrane and shear action and bending becomes less important. An *upwards* shift is observed when an element locks in bending-dominated cases.

In Table 4.10 we report results obtained with a wider refined boundary region: here we set this width to $15\sqrt{t}$ instead of $6\sqrt{t}$. Note that this meshing scheme can not be used when $t = 10^{-2}$. For all the thicknesses studied we observe qualitatively the same results with this meshing pattern as when the refined region is narrower. This implies that the choice of the width of the refined region is not a critical one: provided a reasonable width is selected with Table 2.1 in mind, optimal uniform convergence is observed.

4.4.3 Free hyperboloid

Table 4.11 lists the values of the error measure EM calculated for the free hyperboloid modelled with uniform meshes, as well as the strain energies of the reference solutions. The relative errors RE are shown in Figure 4-11.

Table 4.12 lists the values of the error measure EM calculated for the free hyperboloid modelled with locally refined meshes, as well as the strain energies of the reference solutions. The relative errors RE are shown in Figure 4-12.

From Figures 4-11, we observe that when uniform meshes are employed for this problem the convergence order is low and clearly sub-optimal for relatively thick shells. When locally refined meshes are employed, we conclude from Figure 4-12 that the optimal convergence rates are recovered for all elements. However, for the MITC9 and MITC16 elements some upwards shifting of the curves is observed, indicating that the convergence is not uniform. We attribute this non-uniformity to spurious shear strains in the finite element solution, see Figure 4-13.

Table 4.9: Clamped hyperboloid problem: error measure $EM(U_{ref}, U_h)$ and reference energies $E(U_{ref}, U_{ref})$ with graded mesh. The meshes employed are as described in Figure 4-7 with $w = 6\sqrt{t}$. Reference solutions for MITC4 (respectively MITC9, MITC16) elements are obtained using a 192×192 (respectively 96×96, 72×72) MITC4 (respectively MITC9, MITC16) mesh.

t	N	MITC4	t	N	MITC9	t	N	MITC16
	24	$0.51216745.10^{1}$		8	$0.36116578.10^{1}$		6	$0.53808129.10^{0}$
	32	$0.28478056.10^{1}$		16	$0.24692384.10^{0}$		12	$0.73989732.10^{-2}$
10^{-2}	48	$0.12205125.10^{1}$	10^{-2}	24	$0.48485835.10^{-1}$	10^{-2}	18	$0.70492752.10^{-3}$
	64	$0.65085399.10^{0}$		32	$0.15193060.10^{-1}$		24	$0.16989619.10^{-3}$
Ref. Energy		$0.53913610.10^{3}$	Ref. Energy		$0.53918715.10^{3}$	Ref. Energy		$0.53918722.10^{3}$
	24	$0.47614302.10^{2}$		8	$0.11476748.10^{2}$		6	$0.16563965.10^{1}$
	32	$0.27097576.10^{2}$		16	$0.7643617.10^{0}$		12	$0.22190212.10^{-1}$
10^{-3}	48	$0.11828517.10^{2}$	10^{-3}	24	$0.15225938.10^{0}$	10^{-3}	18	$0.18600742.10^{-2}$
	64	$0.63508722.10^{1}$		32	$0.47648841.10^{-1}$		24	$0.33107839.10^{-3}$
Ref. Energy		$0.60002983.10^{4}$	Ref. Energy		$0.60011494.10^{4}$	Ref. Energy		$0.60011498.10^{4}$
	24	$0.81376109.10^{3}$		8	$0.41207395.10^{2}$		6	$0.54409834.10^{1}$
	32	$0.50641762.10^{3}$		16	$0.27316750.10^{1}$		12	$0.76068406.10^{-1}$
10^{-4}	48	$0.24250934.10^{3}$	10^{-4}	24	$0.52804427.10^{0}$	10^{-4}	18	$0.67433328.10^{-1}$
	64	$0.13585188.10^{3}$		32	$0.16388742.10^{0}$		24	$0.13140647.10^{-2}$
Ref. Energy		$0.61878678.10^{5}$	Ref. Energy		$0.61898766.10^{5}$	Ref. Energy		$0.61898767.10^{5}$
	24	$0.11844320.10^{5}$		8	$0.18838524.10^{3}$		6	$0.19762087.10^{2}$
	32	$0.76762359.10^{4}$		16	$0.12112321.10^{2}$		12	$0.29223663.10^{0}$
10^{-5}	48	$0.43045298.10^{4}$	10^{-5}	24	$0.23368748.10^{1}$	10^{-5}	18	$0.30532623.10^{-1}$
	64	$0.26726276.10^{4}$		32	$0.72375199.10^{0}$		24	$0.85891040.10^{-2}$
Ref. Energy		$0.62436470.10^{6}$	Ref. Energy		$0.62488945.10^{6}$	Ref. Energy		$0.62488946.10^{6}$
	24	$0.16983036.10^{6}$		8	$0.11846829.10^{4}$		6	$0.88813013.10^{2}$
	32	$0.11184599.10^{6}$		16	$0.74948993.10^{2}$		12	$0.13879814.10^{1}$
10^{-6}	48	$0.59927032.10^{5}$	10^{-6}	24	$0.14415752.10^{2}$	10^{-6}	18	$0.14608371.10^{0}$
	64	$0.37171547.10^{5}$		32	$0.44259376.10^{1}$		24	$0.39427488.10^{-1}$
Ref. Energy		$0.62566295.10^{7}$	Ref. Energy		$0.62674820.10^{7}$	Ref. Energy		$0.62674820.10^{7}$

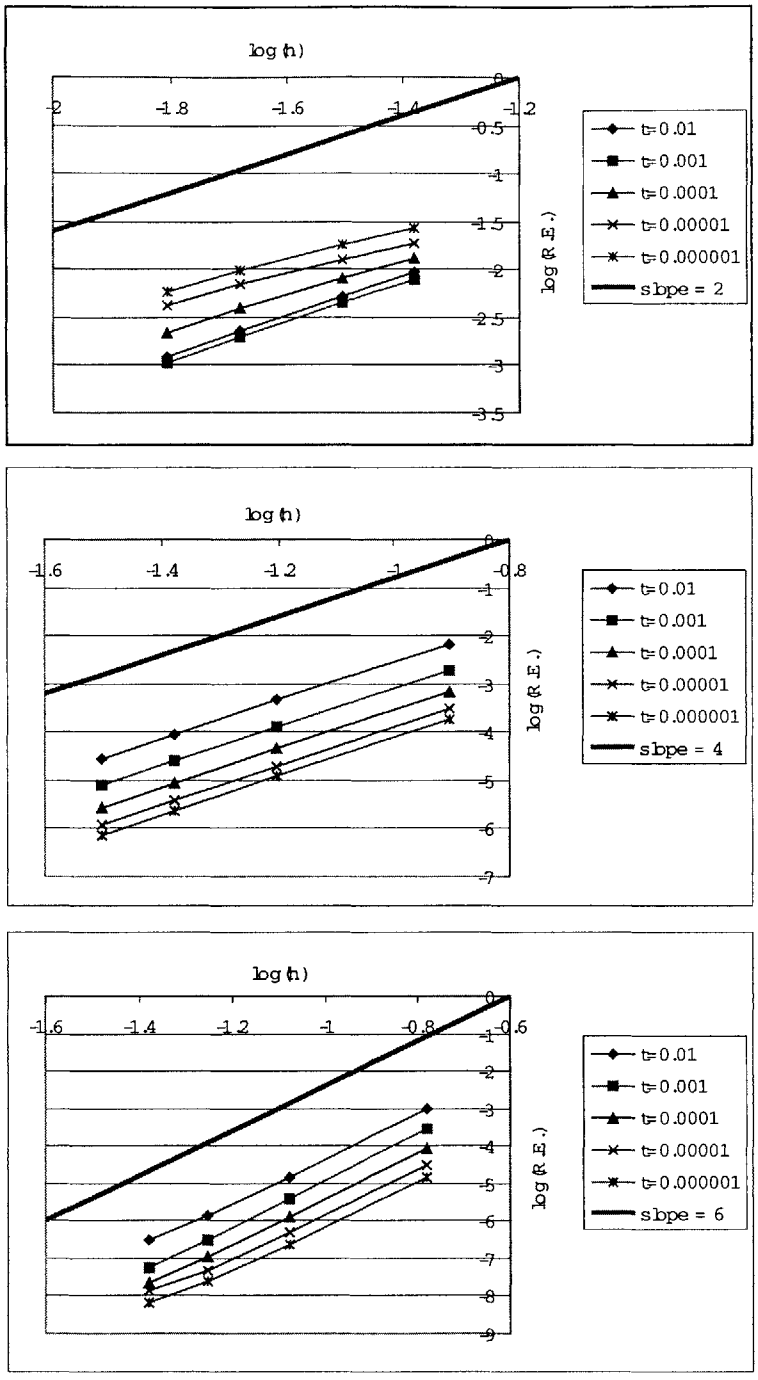

Figure 4-10: Clamped hyperboloid modelled with graded meshes: convergence. Top to bottom: MITC4, MITC9, MITC16. The reference solutions are established using very fine meshes of the same MITC elements.

Table 4.10: Clamped hyperboloid problem: error measure $E(U_{ref}, U_h)$ with wider refined layer. The meshes employed are as described in Figure 4-7 with $w = 15\sqrt{t}$. The reference strain energy corresponding to each thickness is also listed. Reference solutions are obtained using a 192×192 mesh.

t	N	MITC4
10^{-3}	24	$0.10686863.10^3$
	32	$0.62240597.10^2$
	48	$0.27220360.10^2$
	64	$0.14573248.10^2$
Reference Energy		$0.5999979.10^4$
10^{-4}	24	$0.94278961.10^3$
	32	$0.59140273.10^3$
	48	$0.28428606.10^3$
	64	$0.15949176.10^3$
Reference Energy		$0.61877837.10^5$
10^{-5}	24	$0.11429373.10^5$
	32	$0.78505005.10^4$
	48	$0.43816738.10^4$
	64	$0.27337262.10^4$
Reference Energy		$0.62436267.10^6$
10^{-6}	24	$0.13315888.10^6$
	32	$0.90340395.10^5$
	48	$0.51805649.10^5$
	64	$0.33873580.10^5$
Reference Energy		$0.62566391.10^7$

Table 4.11: Free hyperboloid problem: error measure with uniform mesh. The meshes employed are as described in Figure 4-6. The reference strain energy corresponding to each pair of element and thickness is also listed. Reference solutions for MITC4 (respectively MITC9, MITC16) elements are obtained using a 192×192 (respectively 96×96, 72×72) MITC4 (respectively MITC9, MITC16) mesh.

t	N	MITC4	t	N	MITC9	t	N	MITC16
	24	$0.72855075.10^3$		8	$0.33196961.10^3$		6	$0.28927719.10^3$
	32	$0.49234764.10^3$		16	$0.23416893.10^3$		12	$0.21533942.10^3$
10^{-2}	48	$0.29709714.10^3$	10^{-2}	24	$0.18331049.10^3$	10^{-2}	18	$0.15534610.10^3$
	64	$0.20612393.10^3$		32	$0.14098954.10^3$		24	$0.10929069.10^3$
Ref. Energy		$0.45278930.10^6$	Ref. Energy		$0.45281686.10^6$	Ref. Energy		$0.45283762.10^6$
	24	$0.44398166.10^6$		8	$0.11786257.10^7$		6	$0.15551939.10^5$
	32	$0.24871533.10^6$		16	$0.44470786.10^5$		12	$0.86264262.10^4$
10^{-3}	48	$0.10902938.10^6$	10^{-3}	24	$0.94170794.10^4$	10^{-3}	18	$0.74982012.10^4$
	64	$0.59778884.10^5$		32	$0.56432844.10^4$		24	$0.66075789.10^4$
Ref. Energy		$0.44858915.10^9$	Ref. Energy		$0.44857874.10^9$	Ref. Energy		$0.44858130.10^9$
	24	$0.43435928.10^9$		8	$0.24971031.10^{11}$		6	$0.20081647.10^9$
	32	$0.24089397.10^9$		16	$0.73559245.10^9$		12	$0.53663836.10^6$
10^{-4}	48	$0.10315750.10^9$	10^{-4}	24	$0.12647260.10^9$	10^{-4}	18	$0.16112248.10^6$
	64	$0.55030769.10^8$		32	$0.35640494.10^8$		24	$0.10762272.10^6$
Ref. Energy		$0.44853495.10^{12}$	Ref. Energy		$0.44851520.10^{12}$	Ref. Energy		$0.44853338.10^{12}$
	24	$0.43361004.10^{12}$		8	$0.37908020.10^{15}$		6	$0.18420106.10^{14}$
	32	$0.24040719.10^{12}$		16	$0.37181878.10^{14}$		12	$0.19932182.10^{11}$
10^{-5}	48	$0.10291407.10^{12}$	10^{-5}	24	$0.3693825.10^{13}$	10^{-5}	18	$0.11209628.10^{10}$
	64	$0.54874523.10^{11}$		32	$0.71389892.10^{12}$		24	$0.62564826.10^9$
Ref. Energy		$0.44878506.10^{15}$	Ref. Energy		$0.44886247.10^{15}$	Ref. Energy		$0.44959833.10^{15}$

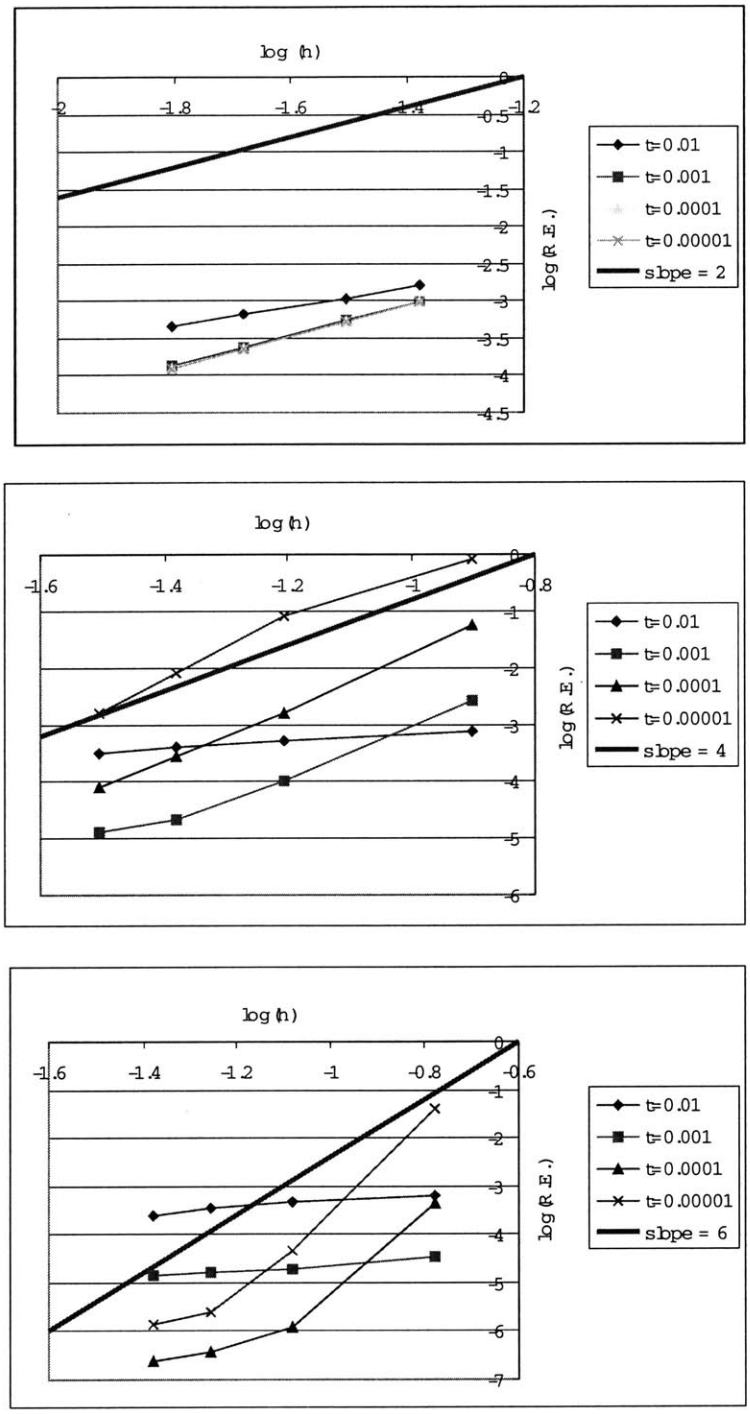

Figure 4-11: Free hyperboloid modelled with uniform meshes: convergence. Top to bottom: MITC4, MITC9, MITC16. The reference solutions are established using a very fine mesh of the same MITC elements.

Table 4.12: Free hyperboloid problem: error measure with graded mesh. The meshes employed are as described in Figure 4-7 with $w = 0.5\sqrt{t}$. The reference strain energy corresponding to each pair of element and thickness is also listed. Reference solutions for MITC4 (respectively MITC9, MITC16) elements are obtained using a 192×192 (respectively 96×96, 72×72) MITC4 (respectively MITC9, MITC16) mesh.

t	N	MITC4	t	N	MITC9	t	N	MITC16
	24	$0.71918770.10^{3}$		8	$0.22277779.10^{3}$		6	$0.21606074.10^{2}$
	32	$0.40106127.10^{3}$		16	$0.11945223.10^{2}$		12	$0.14889883.10^{1}$
10^{-2}	48	$0.17242825.10^{3}$	10^{-2}	24	$0.26357486.10^{1}$	10^{-2}	18	$0.21364503.10^{0}$
	64	$0.92073475.10^{2}$		32	$0.88084694.10^{0}$		24	$0.46812929.10^{-1}$
Ref. Energy		$0.45284701.10^{6}$	Ref. Energy		$0.45284688.10^{6}$	Ref. Energy		$0.45284690.10^{6}$
	24	$0.673760306.10^{6}$		8	$0.13338949.10^{8}$		6	$0.10981791.10^{6}$
	32	$0.37710558.10^{6}$		16	$0.27740606.10^{6}$		12	$0.63322788.10^{4}$
10^{-3}	48	$0.16355965.10^{6}$	10^{-3}	24	$0.29407718.10^{4}$	10^{-3}	18	$0.21275709.10^{4}$
	64	$0.87866179.10^{5}$		32	$0.70179931.10^{4}$		24	$0.83471833.10^{3}$
Ref. Energy		$0.44860911.10^{9}$	Ref. Energy		$0.44861047.10^{9}$	Ref. Energy		$0.44861198.10^{9}$
	24	$0.69053694.10^{9}$		8	$0.33132311.10^{12}$		6	$0.75614437.10^{10}$
	32	$0.37187383.10^{9}$		16	$0.22890523.10^{11}$		12	$0.10425136.10^{8}$
10^{-4}	48	$0.15810902.10^{9}$	10^{-4}	24	$0.22479694.10^{10}$	10^{-4}	18	$0.19065895.10^{7}$
	64	$0.084613210.10^{8}$		32	$0.41437454.10^{9}$		24	$0.12225507.10^{7}$
Ref. Energy		$0.44884510.10^{12}$	Ref. Energy		$0.44874675.10^{12}$	Ref. Energy		$0.44855220.10^{12}$

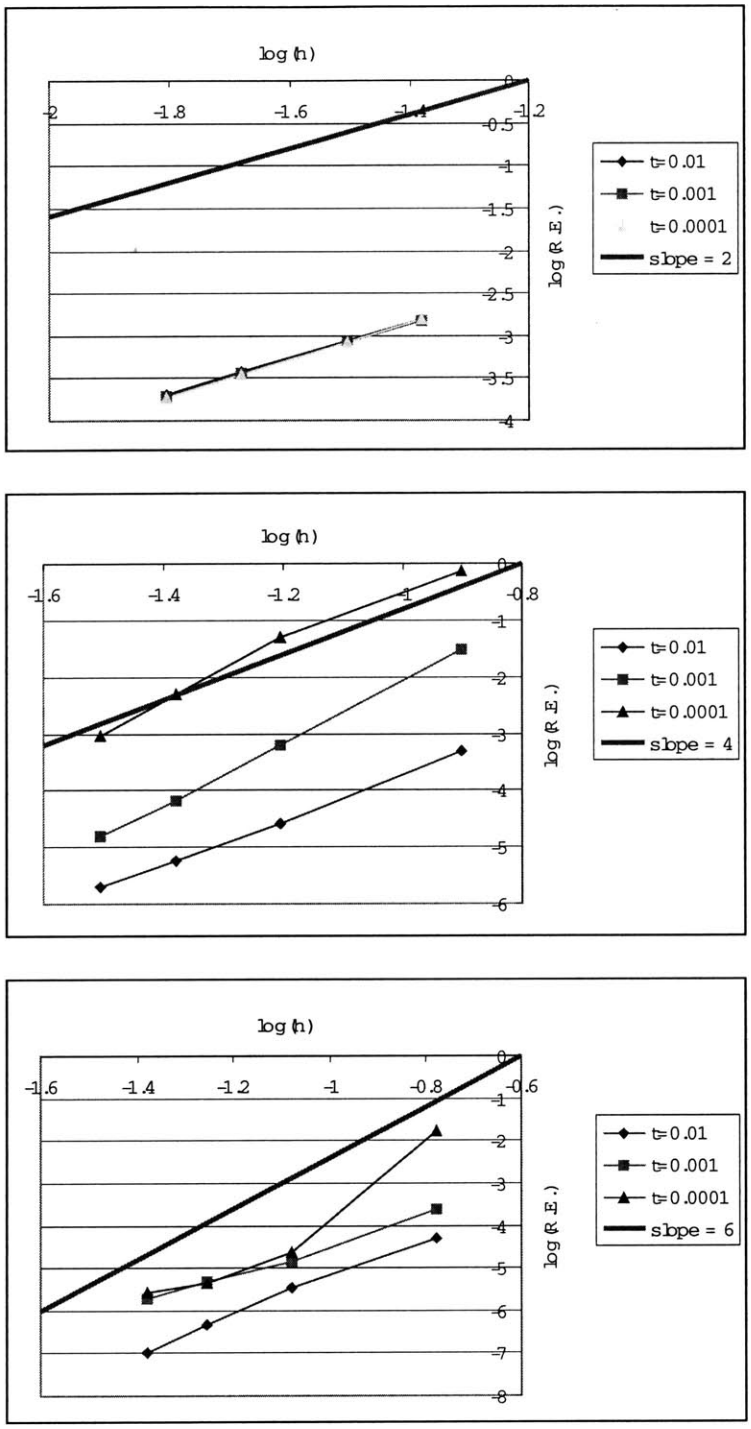

Figure 4-12: Free hyperboloid modelled with graded meshes: convergence. Top to bottom: MITC4, MITC9, MITC16. The reference solutions are established using very fine meshes of the same MITC elements.

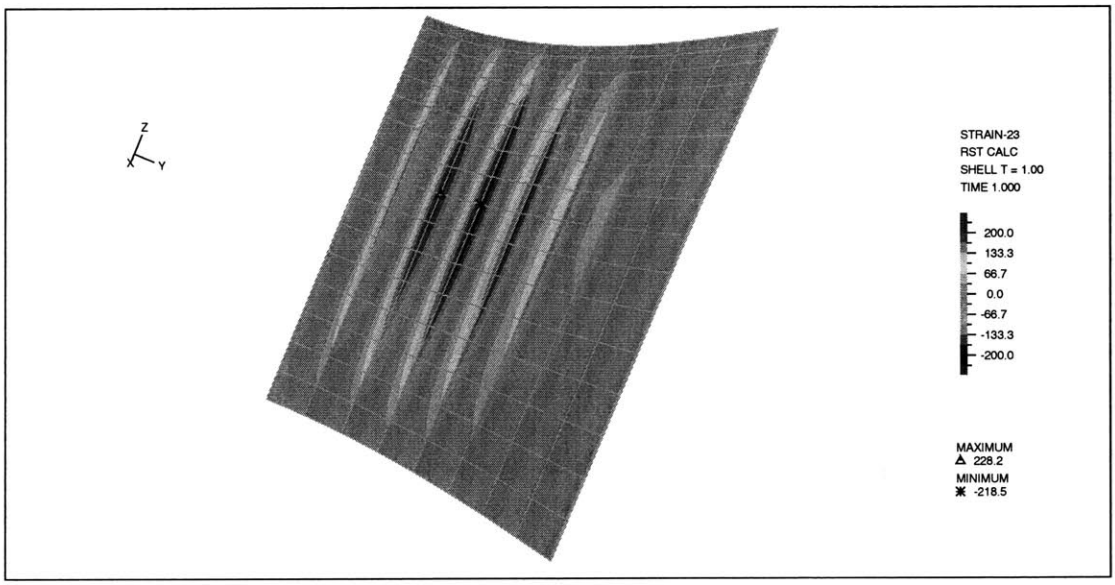

Figure 4-13: Spurious transverse shear strain $e_{\bar{s}\bar{t}}$ in the finite element solution of the free hyperboloid with the graded 16×16 MITC9 mesh for the thickness $t = 10^{-4}$. The $\bar{s}$ direction is the same as the θ direction, see Figure 4-4. The magnitude of $e_{\bar{s}\bar{t}}$ is to compare with the magnitude of the largest strain, $e_{\bar{r}\bar{s}}$, presented on Figure 4-14. Also the lack of smoothness in $e_{\bar{s}\bar{t}}$ is obvious.

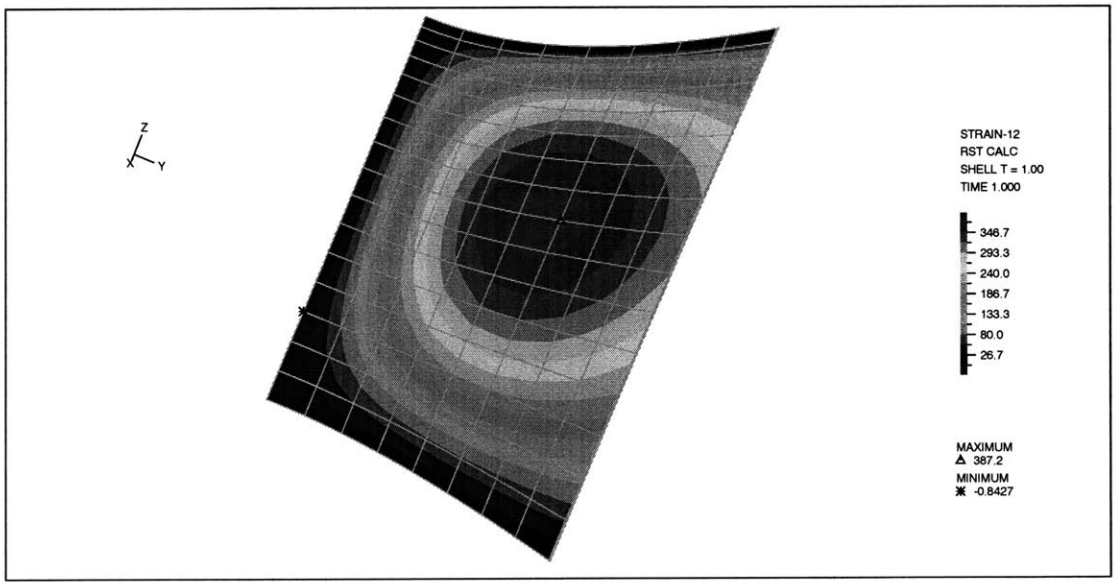

Figure 4-14: Strain $e_{\bar{r}\bar{s}}$ in the finite element solution of the free hyperboloid with the graded 16×16 MITC9 mesh for the thickness $t = 10^{-4}$. This component of the strain tensor is seen to be very smooth, even with this relatively coarse mesh.

Conclusions

Shells of small thickness feature boundary and internal layers which need to be taken into account when modelling a shell structure with the finite element method. Indeed, our numerical tests of Section 4 demonstrate that the choice of meshes employed in an analysis can crucially influence the convergence order of the finite element solution to the exact solution of the mathematical model. The location and width of boundary and internal layers can be predicted, as indicated in Section 2. A gallery of typical boundary and internal layers was produced, demonstrating the complexity of these phenomena and their strong dependance on loadings, boundary conditions and shell mid-surface nature.

We reviewed the derivation of the basic shell problem and the formulation of the MITC family of elements and justified the use of mixed-interpolation methods by the need to alleviate the locking phenomenon. We indicated what error measure procedures have been employed to test existing finite element schemes. In particular, we showed that until now there did not exist a procedure that allowed to rigorously assess the discrepancy between the exact mathematical solution of a shell problem and the approximate solution of the same problem obtained through the use of a finite element procedure. We designed a new error measure method that can be used to evaluate this discrepancy. Our proposed error measure, which is physically based, defines a norm for the error in the strains and can be extended to other problems where mixed-interpolated finite element methods are used, such as plates, beams or incompressible materials.

We used this new error measure to confirm in the case of a membrane-dominated problem that the finite element solution obtained with the MITC elements converges

with optimal convergence order to the solution obtained with a very fine mesh of displacement-based elements. From this observation, we concluded that the MITC elements are consistent with the basic shell model.

Having confirmed consistency, we studied the convergence properties of the MITC elements in the case of tough new benchmark problems. Specifically, we investigated the influence of meshes on the convergence rates observed in a membrane-dominated problem and a bending-dominated problem. We compared two mesh patterns: uniform meshes which do not take into account the presence of layers and locally refined meshes in which smaller elements are grouped in the region where layers are expected. Our investigation of the MITC elements indicates that the use of locally refined meshes is crucial in allowing the optimal convergence rates to be observed. In the case of a membrane-dominated problem, uniformly optimal convergence was observed. For the MITC9 and MITC16 elements, this convergence was observed to be non-uniform due to spurious transverse shear strains, indicating that some improvements of these elements are possible. In Appendix D a modified MITC9 scheme is proposed which does not feature this phenomenon.

A natural extension of the work presented in this thesis would be the study by the same approach of other existing mixed finite element formulations, such as the isoparametric u/p elements used in incompressible material analysis, or the MITC plate elements.

Appendix A

Mixed strains in the MITC4 element

In this appendix, we list the explicit expressions for the mixed strains in the MITC4 element.

A.1 Conventions employed

The degrees of freedom of the element are numbered as follow:

- $1-5$: translation then rotation degrees of freedom for node number 1,
- $6-10$: translation then rotation degrees of freedom for node number 2,
- $11-15$: translation then rotation degrees of freedom for node number 3,
- $16-20$: translation then rotation degrees of freedom for node number 4.

The rotation degrees of freedom for node number k are considered about the directions $\vec{V}_1^k$ and $\vec{V}_2^k$ defined (cf [11]) by:

- if $\vec{V}_n^k$, the normal vector at node number k, is not colinear with the Cartesian

base vector $\vec{e}_y$:

$$\begin{cases} \vec{V_1^k} = \dfrac{\vec{e}_y \times \vec{V_n^k}}{\|\vec{e}_y \times \vec{V_n^k}\|} \\ \vec{V_2^k} = \vec{V_n^k} \times \vec{V_1^k} \end{cases} \tag{A.1}$$

- if $\vec{V_n^k}$ is colinear with the Cartesian base vector $\vec{e}_y$:

$$\begin{cases} \vec{V_1^k} = \vec{e}_z \\ \vec{V_2^k} = \vec{e}_x \end{cases} \tag{A.2}$$

A.2 Assumed strain matrix components

We give here the terms for the assumed strain matrices $B^{AS}_{\xi_1\xi_3}$ and $B^{AS}_{\xi_2\xi_3}$ in the case where none of the four nodal normal vectors is colinear with $\vec{e}_y$:

$$B^{AS}_{\xi_1\xi_3}(1) = \frac{1}{32}\left(a_1 V^1_{n1} + a_2 V^2_{n1}\right)(1+\xi_2) \tag{A.3}$$

$$B^{AS}_{\xi_1\xi_3}(2) = \frac{1}{32}\left(a_1 V^1_{n2} + a_2 V^2_{n2}\right)(1+\xi_2) \tag{A.4}$$

$$B^{AS}_{\xi_1\xi_3}(3) = \frac{1}{32}\left(a_1 V^1_{n3} + a_2 V^2_{n3}\right)(1+\xi_2) \tag{A.5}$$

$$\begin{aligned} B^{AS}_{\xi_1\xi_3}(4) = {} & \tfrac{1}{32}\, a_1 \left(V^1_{n1} V^1_{n2} X^1_1 - V^1_{n1} V^1_{n2} X^2_1 - X^1_2 {V^1_{n3}}^2 - X^1_2 {V^1_{n1}}^2 + \right. \\ & \left. X^2_2 {V^1_{n3}}^2 + X^2_2 {V^1_{n1}}^2 + V^1_{n3} V^1_{n2} X^1_3 - V^1_{n3} V^1_{n2} X^2_3\right)(1+\xi_2)/\sqrt{{V^1_{n3}}^2 + {V^1_{n1}}^2} \end{aligned} \tag{A.6}$$

$$B^{AS}_{\xi_1\xi_3}(5) = \frac{1}{32}\,\frac{a_1\left(V^1_{n3} X^1_1 - V^1_{n3} X^2_1 - V^1_{n1} X^1_3 + V^1_{n1} X^2_3\right)(1+\xi_2)}{\sqrt{{V^1_{n3}}^2 + {V^1_{n1}}^2}} \tag{A.7}$$

$$B^{AS}_{\xi_1\xi_3}(6) = -B^{AS}_{\xi_1\xi_3}(1) \tag{A.8}$$

$$B^{AS}_{\xi_1\xi_3}(7) = -B^{AS}_{\xi_1\xi_3}(2) \tag{A.9}$$

$$B^{AS}_{\xi_1\xi_3}(8) = -B^{AS}_{\xi_1\xi_3}(3) \tag{A.10}$$

$$\begin{aligned} B^{AS}_{\xi_1\xi_3}(9) = \tfrac{1}{32} a_2 (V^2_{n1}\, V^2_{n2}\, X^1_1 - V^2_{n1}\, V^2_{n2} X^2_1 - X^1_2\, {V^2_{n3}}^2 - X^1_2\, {V^2_{n1}}^2 + \\ X^2_2\, {V^2_{n3}}^2 + X^2_2\, {V^2_{n1}}^2 + V^2_{n3}\, V^2_{n2}\, X^1_3 - V^2_{n3}\, V^2_{n2}\, X^2_3)(1+\xi_2)/\sqrt{{V^2_{n3}}^2 + {V^2_{n1}}^2} \end{aligned} \tag{A.11}$$

$$B^{AS}_{\xi_1\xi_3}(10) = \frac{1}{32} \frac{a_2\,(V^2_{n3}\, X^1_1 - V^2_{n3}\, X^2_1 - V^2_{n1}\, X^1_3 + V^2_{n1}\, X^2_3)\,(1+\xi_2)}{\sqrt{{V^2_{n3}}^2 + {V^2_{n1}}^2}} \tag{A.12}$$

$$B^{AS}_{\xi_1\xi_3}(11) = \frac{1}{32}\,(a_3\, V^3_{n1} + a_4\, V^4_{n1})\,(-1+\xi_2) \tag{A.13}$$

$$B^{AS}_{\xi_1\xi_3}(12) = \frac{1}{32}\,(a_3\, V^3_{n2} + a_4\, V^4_{n2})\,(-1+\xi_2) \tag{A.14}$$

$$B^{AS}_{\xi_1\xi_3}(13) = \frac{1}{32}\,(a_3\, V^3_{n3} + a_4\, V^4_{n3})\,(-1+\xi_2) \tag{A.15}$$

$$\begin{aligned} B^{AS}_{\xi_1\xi_3}(14) = \tfrac{1}{32} a_3 (V^3_{n1}\, V^3_{n2}\, X^3_1 - V^3_{n1}\, V^3_{n2} X^4_1 - X^3_2\, {V^3_{n3}}^2 - X^3_2\, {V^3_{n1}}^2 \\ + X^4_2\, {V^3_{n3}}^2 + X^4_2\, {V^3_{n1}}^2 + V^3_{n3}\, V^3_{n2}\, X^3_3 - V^3_{n3}\, V^3_{n2}\, X^4_3)(-1+\xi_2)/\sqrt{{V^3_{n3}}^2 + {V^3_{n1}}^2} \end{aligned} \tag{A.16}$$

$$B^{AS}_{\xi_1\xi_3}(15) = \frac{1}{32} \frac{a_3\,(V^3_{n3}\, X^3_1 - V^3_{n3}\, X^4_1 - V^3_{n1}\, X^3_3 + V^3_{n1}\, X^4_3)\,(-1+\xi_2)}{\sqrt{{V^3_{n3}}^2 + {V^3_{n1}}^2}} \tag{A.17}$$

$$B^{AS}_{\xi_1\xi_3}(16) = -B^{AS}_{\xi_1\xi_3}(11) \tag{A.18}$$

$$B^{AS}_{\xi_1\xi_3}(17) = -B^{AS}_{\xi_1\xi_3}(12) \tag{A.19}$$

$$B^{AS}_{\xi_1\xi_3}(18) = -B^{AS}_{\xi_1\xi_3}(13) \tag{A.20}$$

$$\begin{aligned} B^{AS}_{\xi_1\xi_3}(19) = {} & \tfrac{1}{32} a_4 (V^4_{n1}\, V^4_{n2}\, X^{X3}_1 - V^4_{n1}\, V^4_{n2}\, X^4_1 - X^3_2\, {V^4_{n3}}^2 - X^3_2\, {V^4_{n1}}^2 \\ & + X^4_2\, {V^4_{n3}}^2 + X^4_2\, {V^4_{n1}}^2 + V^4_{n3}\, V^4_{n2}\, X^3_3 - V^4_{n3}\, V^4_{n2}\, X^4_3)(-1+\xi_2)/\sqrt{{V^4_{n3}}^2 + {V^4_{n1}}^2} \end{aligned} \tag{A.21}$$

$$B^{AS}_{\xi_1\xi_3}(20) = \frac{1}{32} \frac{a_4\,(V^4_{n3}\, X^3_1 - V^4_{n3}\, X^4_1 - V^4_{n1}\, X^3_3 + V^4_{n1}\, X^4_3)\,(-1+\xi_2)}{\sqrt{{V^4_{n3}}^2 + {V^4_{n1}}^2}} \tag{A.22}$$

$$B^{AS}_{\xi_2\xi_3}(1) = \frac{1}{32}\,(a_1\, V^1_{n1} + a_4\, V^4_{n1})\,(1+\xi_1) \tag{A.23}$$

$$B^{AS}_{\xi_2\xi_3}(2) = \frac{1}{32}\,(a_1\, V^1_{n2} + a_4\, V^4_{n2})\,(1+\xi_1) \tag{A.24}$$

$$B^{AS}_{\xi_2\xi_3}(3) = \frac{1}{32}\,(a_1\, V^1_{n3} + a_4\, V^4_{n3})\,(1+\xi_1) \tag{A.25}$$

$$\begin{aligned} B^{AS}_{\xi_2\xi_3}(4) = {} & \tfrac{1}{32} a_1 (V^1_{n1}\, V^1_{n2}\, X^1_1 - V^1_{n1}\, V^1_{n2}\, X^4_1 - X^1_2\, {V^1_{n3}}^2 - X^1_2\, {V^1_{n1}}^2 \\ & + X^4_2\, {V^1_{n3}}^2 + X^4_2\, {V^1_{n1}}^2 + V^1_{n3}\, V^1_{n2}\, X^1_3 - V^1_{n3}\, V^1_{n2}\, X^4_3)(1+\xi_1)/\sqrt{{V^1_{n3}}^2 + {V^1_{n1}}^2} \end{aligned} \tag{A.26}$$

$$B^{AS}_{\xi_2\xi_3}(5) = \frac{1}{32} \frac{a_1\,(V^1_{n3}\, X^1_1 - V^1_{n3}\, X^4_1 - V^1_{n1}\, X^1_3 + V^1_{n1}\, X^4_3)\,(1+\xi_1)}{\sqrt{{V^1_{n3}}^2 + {V^1_{n1}}^2}} \tag{A.27}$$

$$B^{AS}_{\xi_2\xi_3}(6) = -\frac{1}{32}\,(a_2\, V^2_{n1} + a_3\, V^3_{n1})\,(-1+\xi_1) \tag{A.28}$$

$$B^{AS}_{\xi_2\xi_3}(7) = -\frac{1}{32}\left(a_2\, V^2_{n2} + a_3\, V^3_{n2}\right)(-1+\xi_1) \tag{A.29}$$

$$B^{AS}_{\xi_2\xi_3}(8) = -\frac{1}{32}\left(a_2\, V^2_{n3} + a_3\, V^3_{n3}\right)(-1+\xi_1) \tag{A.30}$$

$$\begin{aligned} B^{AS}_{\xi_2\xi_3}(9) = &-\tfrac{1}{32}a_2(V^2_{n1}\, V^2_{n2}\, X^2_1 - \, V^2_{n1}\, V^2_{n2}\, X^3_1 - 1\, X^2_2\, {V^2_{n3}}^2 - \, X^2_2\, {V^2_{n1}}^2 \\ &+X^3_2\, {V^2_{n3}}^2 + X^3_2\, {V^2_{n1}}^2 + V^2_{n3}\, V^2_{n2}\, X^2_3 - \, V^2_{n3}\, V^2_{n2}\, X^3_3)(-1+\xi_1)/\sqrt{{V^2_{n3}}^2 + {V^2_{n1}}^2} \end{aligned} \tag{A.31}$$

$$B^{AS}_{\xi_2\xi_3}(10) = -\frac{1}{32}\,\frac{a_2\left(V^2_{n3}\, X^2_1 - \, V^2_{n3}\, X^3_1 - \, V^2_{n1}\, X^2_3 + V^2_{n1}\, X^3_3\right)(-1+\xi_1)}{\sqrt{{V^2_{n3}}^2 + {V^2_{n1}}^2}} \tag{A.32}$$

$$B^{AS}_{\xi_2\xi_3}(11) = -B^{AS}_{\xi_2\xi_3}(6) \tag{A.33}$$

$$B^{AS}_{\xi_2\xi_3}(12) = -B^{AS}_{\xi_2\xi_3}(7) \tag{A.34}$$

$$B^{AS}_{\xi_2\xi_3}(13) = -B^{AS}_{\xi_2\xi_3}(8) \tag{A.35}$$

$$\begin{aligned} B^{AS}_{\xi_2\xi_3}(14) = &-\tfrac{1}{32}a_3(V^3_{n1}\, V^3_{n2}\, X^2_1 - \, V^3_{n1}\, V^3_{n2}\, X^3_1 - 1\, X^2_2\, {V^3_{n3}}^2 - \, X^2_2\, {V^3_{n1}}^2 \\ &+X^3_2\, {V^3_{n3}}^2 + X^3_2\, {V^3_{n1}}^2 + V^3_{n3}\, V^3_{n2}\, X^2_3 - \, V^3_{n3}\, V^3_{n2}\, X^3_3)(-1+\xi_1)/\sqrt{{V^3_{n3}}^2 + {V^3_{n1}}^2} \end{aligned} \tag{A.36}$$

$$B^{AS}_{\xi_2\xi_3}(15) = -\frac{1}{32}\,\frac{a_3\left(V^3_{n3}\, X^2_1 - \, V^3_{n3}\, X^3_1 - \, V^3_{n1}\, X^2_3 + V^3_{n1}\, X^3_3\right)(-1+\xi_1)}{\sqrt{{V^3_{n3}}^2 + {V^3_{n1}}^2}} \tag{A.37}$$

$$B^{AS}_{\xi_2\xi_3}(16) = -B^{AS}_{\xi_2\xi_3}(1) \tag{A.38}$$

$$B^{AS}_{\xi_2\xi_3}(17) = -B^{AS}_{\xi_2\xi_3}(2) \tag{A.39}$$

$$B^{AS}_{\xi_2\xi_3}(18) = -B^{AS}_{\xi_2\xi_3}(3) \tag{A.40}$$

$$\begin{aligned} B^{AS}_{\xi_2\xi_3}(19) = \tfrac{1}{32} a_4 (V^4_{n1}\, V^4_{n2}\, X^1_1 - V^4_{n1}\, V^4_{n2}\, X^4_1 - X^1_2\, {V^4_{n3}}^2 - X^1_2\, {V^4_{n1}}^2 \\ + X^4_2\, {V^4_{n3}}^2 + X^4_2\, {V^4_{n1}}^2 + V^4_{n3}\, V^4_{n2}\, X^1_3 - V^4_{n3}\, V^4_{n2}\, X^4_3)(1+\xi_1))/\sqrt{{V^4_{n3}}^2 + {V^4_{n1}}^2} \end{aligned} \tag{A.41}$$

$$B^{AS}_{\xi_2\xi_3}(20) = \frac{1}{32} \frac{a_4 \left(V^4_{n3}\, X^1_1 - V^4_{n3}\, X^4_1 - V^4_{n1}\, X^1_3 + V^4_{n1}\, X^4_3\right)(1+\xi_1)}{\sqrt{{V^4_{n3}}^2 + {V^4_{n1}}^2}} \tag{A.42}$$

In the special case where one (or several) of the nodal normal vectors is (or are) colinear with $\vec{e}_y$, the terms in $B^{AS}_{\xi_1\xi_3}$ and $B^{AS}_{\xi_2\xi_3}$ are slightly different than the expressions given above, and they are in fact marginally simpler than the expressions given above. Therefore in all cases the assumed strain matrices are relatively simple and it is more computationally efficient to evaluate the assumed strain matrices directly from these expressions rather than by following the conventional tying procedure. The terms of the direct interpolation strain matrices, which we do not list here, are relatively more complex and are therefore evaluated using the usual method.

We coded the MITC4 element using this procedure. The time required to establish the stiffness matrix using 2x2x2 Gaussian quadrature was measured at $1.97 \cdot 10^{-4}$ second per element. This is to be compared to $2.27 \cdot 10^{-4}$ second per element for our conventionally computed MITC4 element (15 percent improvement), and to $4.3 \cdot 10^{-4}$ second per element for the same element in ADINA (54 percent improvement). All these computations were carried out on an 833MHz Pentium 3 computer.

It should be noted also that the proposed procedure should compare to the conventional procedure even more favorably in the case of higher order elements such as the MITC9 and MITC16 elements for three reasons:

- In higher order elements, all five non-zero strains are mixed interpolated, compared to just two in the case of the MITC4 element.

- In higher order elements, more tying points are employed making the tying procedure all the more computationally expensive.

- In higher order elements, higher order Gaussian quadrature needs to be used. In the proposed procedure all geometric constants are computed once and for all outside the integration loops over all integration points.

We list below the code employed to calculate the expressions in Equations A.3 through A.42. The corresponding code used to evaluate the calculate the B matrices of the MITC9 and MITC16 is immediate.

We should mention that besides allowing to implement faster *existing* MITC elements, this analytical treatment of the B matrices could be used to create new element formulations. For instance, new triangular elements[1] could be studied through this approach. In particular, we can evaluate using this approach the B matrices of potential new formulations to determine whether they result in elements that satisfy the ellipticity condition, etc.

Finally, we note that all our implementations of the MITC4 element compute faster than similar implementations of the displacement-based QUAD4 element.

[1]Here we note that isotropic triangular elements are highly desirable.

```
> h1:=.25*(1+r)*(1+s):
h2:=.25*(1-r)*(1+s):
h3:=.25*(1-r)*(1-s):
h4:=.25*(1+r)*(1-s):
X:=X1*h1+X2*h2+X3*h3+X4*h4+ 0.5*t*(a1*h1*VNIX1+a2*h2*VNIX2+a3*h3*VNIX3
+a4*h4*VNIX4):
Xr:=diff(X,r):
Xs:=diff(X,s):
Xt:=diff(X,t):
Y:=Y1*h1+Y2*h2+Y3*h3+Y4*h4+ 0.5*t*(a1*h1*VNIY1+a2*h2*VNIY2+a3*h3*VNIY3
+a4*h4*VNIY4):
Yr:=diff(Y,r):
Ys:=diff(Y,s):
Yt:=diff(Y,t):
Z:=Z1*h1+Z2*h2+Z3*h3+Z4*h4+ 0.5*t*(a1*h1*VNIZ1+a2*h2*VNIZ2+a3*h3*VNIZ3
+a4*h4*VNIZ4):
Zr:=diff(Z,r):
Zs:=diff(Z,s):
Zt:=diff(Z,t):
V1X1:=VNIZ1/sqrt(VNIZ1^2+VNIX1^2):
V1Y1:=0:
V1Z1:=-VNIX1/sqrt(VNIZ1^2+VNIX1^2):
V2X1:=-VNIX1*VNIY1/sqrt(VNIZ1^2+VNIX1^2):
V2Y1:=(VNIX1^2+VNIZ1^2)/sqrt(VNIZ1^2+VNIX1^2):
V2Z1:=-VNIZ1*VNIY1/sqrt(VNIZ1^2+VNIX1^2):
V1X2:=VNIZ2/sqrt(VNIZ2^2+VNIX2^2):
V1Y2:=0:
V1Z2:=-VNIX2/sqrt(VNIZ2^2+VNIX2^2):
V2X2:=-VNIX2*VNIY2/sqrt(VNIZ2^2+VNIX2^2):
V2Y2:=(VNIX2^2+VNIZ2^2)/sqrt(VNIZ2^2+VNIX2^2):
V2Z2:=-VNIZ2*VNIY2/sqrt(VNIZ2^2+VNIX2^2):
V1X3:=VNIZ3/sqrt(VNIZ3^2+VNIX3^2):
V1Y3:=0:
V1Z3:=-VNIX3/sqrt(VNIZ3^2+V NIX3^2):
V2X3:=-VNIX3*VNIY3/sqrt(VNIZ3^2+VNIX3^2):
```

```
V2Y3:=(VNIX3^2+VNIZ3^2)/sqrt(VNIZ3^2+VNIX3^2):
V2Z3:=-VNIZ3*VNIY3/sqrt(VNIZ3^2+VNIX3^2):
V1X4:=VNIZ4/sqrt(VNIZ4^2+VNIX4^2):
V1Y4:=0:
V1Z4:=-VNIX4/sqrt(VNIZ4^2+ VNIX4^2):
V2X4:=-VNIX4*VNIY4/sqrt(VNIZ4^2+VNIX4^2):
V2Y4:=(VNIX4^2+VNIZ4^2)/sqrt(VNIZ4^2+VNIX4^2):
V2Z4:=-VNIZ4*VNIY4/sqrt(VNIZ4^2+VNIX4^2):
U1:=linalg[matrix](1,20,[h1, 0, 0,
-0.5*t*a1*h1*V2X1,0.5*t*a1*h1*V1X1, h2, 0, 0,
-0.5*t*a2*h2*V2X2, 0.5*t*a2*h2*V1X2, h3, 0, 0,
-0.5*t*a3*h3*V2X3, 0.5*t*a3*h3*V1X3, h4, 0, 0,
-0.5*t*a4*h4*V2X4,0.5*t*a4*h4*V1X4]):
U2:=linalg[matrix](1,20,[0,h1, 0, -0.5*t*a1*h1*V2Y1,
0.5*t*a1*h1*V1Y1, 0,h2, 0,-0.5*t*a2*h2*V2Y2,
0.5*t*a2*h2*V1Y2,0,h3,0,-0.5*t*a3*h3*V2Y3,
0.5*t*a3*h3*V1Y3,0,h4,0,
-0.5*t*a4*h4*V2Y4,0.5*t*a4*h4*V1Y4]):
U3:=linalg[matrix](1,20,[0,0,h1,-0.5*t*a1*h1*V2Z1,
0.5*t*a1*h1*V1Z1,0,0,h2,-0.5*t*a2*h2*V2Z2,
0.5*t*a2*h2*V1Z2,0,0,h3,-0.5*t*a3*h3*V2Z3,
0.5*t*a3*h3*V1Z3,0,0,h4,-0.5
*t*a4*h4*V2Z4, 0.5*t*a4*h4*V1Z4]):
U1r:=map(diff, U1, r):
U2r:=map(diff,U2, r):
U3r:=map(diff, U3, r):
U1s:=map(diff, U1, s):
U2s:=map(diff, U2, s):
U3s:=map(diff, U3, s):
U1t:=map(diff, U1, t):
U2t:=map(diff, U2, t):
U3t:=map(diff, U3,t):
EDIrr:=linalg[matrix](1,20):
EDIss:=linalg[matrix](1,20):
EDIrs:=linalg[matrix](1,20):
```

```
EDIst:=linalg[matrix](1,20):
EDIrt:=linalg[matrix](1,20):
for m from 1 to 20 do
EDIrr[1,m]:=U1r[1,m]*Xr+U2r[1,m]*Yr+U3r[1,m]*Zr;
EDIss[1,m]:=U1s[1,m]*Xs+U2s[1,m]*Ys+U3s[1,m]*Zs;
EDIrs[1,m]:=.5*(U1r[1,m]*Xs+U2r[1,m]*Ys+U3r[1,m]*Zs+U1s[1,m]*Xr+U2s[1,
m]*Yr+U3s[1,m]*Zr);
EDIst[1,m]:=.5*(U1s[1,m]*Xt+U2s[1,m]*Yt+U3s[1,m]*Zt+U1t[1,m]*Xs+U2t[1,
m]*Ys+U3t[1,m]*Zs);
EDIrt[1,m]:=.5*(U1r[1,m]*Xt+U2r[1,m]*Yt+U3r[1,m]*Zt+U1t[1,m]*Xr+U2t[1,
m]*Yr+U3t[1,m]*Zr);
end do;
EMixedrt[1,m]:=evalf(eval(EDIrt[1,m],[r=0,s=1]))*(1+s)*0.5+evalf(eval
(EDIrt[1,m],[r=0,s=-1]))*(1-s)*0.5;
EMixedst[1,m]:=evalf(eval(EDIst[1,m],[r=1,s=0]))*(1+r)*0.5+evalf(eval
(EDIst[1,m],[r=-1,s=0]))*(1-r)*0.5;
end do;
```

Appendix B

Application of the proposed error measure to a Timoshenko beam

In this appendix, we illustrate the error measure of Equation 4.14 as it applies to a Timoshenko beam [11, 59].

This appendix serves two purposes. First this appendix takes advantage of the simpler geometry to introduce the proposed error measure in a context where all quantities involved can be readily evaluated algebraically, and secondly it illustrates how the proposed error measure can be used in other contexts than shells. Other applications of our error measure include the assessment of the performance of mixed formulations for incompressible and near incompressible materials, incompressible flows and plate structures.

B.1 Structure considered

We consider a straight cantilever beam occupying the domain $\Omega = [0; L]$. The thickness of the beam is denoted by t and its width is 1. The beam is clamped at $x = 0$. We consider two separate loading: a concentrated force F applied at the free end, and a concentrated moment C applied at the free end. Both loadings are represented simultaneously in Figure B-1. The beam is made of a linear isotropic elastic material with Young's modulus E and shear modulus G .

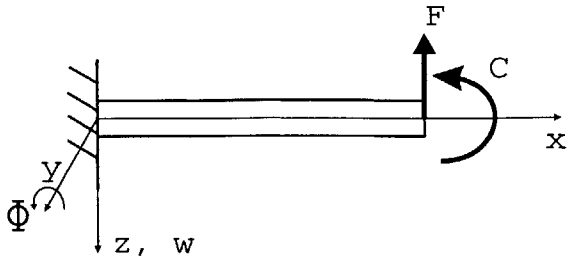

Figure B-1: Beam problem definition. The two separate loadings (a force F and a moment C) are shown simultaneously.

The beam is modelled using the Timoshenko beam theory (see [11, 59]), with the shear correction factor, usually denoted k, set to 1.

The governing equations for the beam are:

$$\begin{cases} Q = Gt(\frac{dw}{dx} + \Phi) \\ M = EI\frac{d\Phi}{dx} \end{cases} \tag{B.1}$$

where Q is the shear force, M is the bending moment, w and Φ are the z direction translation and y axis rotation and $I = \frac{t^3}{12}$ is the second moment of the cross-section.

This beam structure can be regarded as a very basic shell structure, with only two strains present:

$$\begin{cases} \epsilon_{xx} = z\frac{d\Phi}{dx} \\ \gamma_{xz} = \Phi + \frac{dw}{dx} \end{cases} \tag{B.2}$$

In the absence of curvature, the membrane problem decouples from shear and bending (see Section 1.2.5), and since here no loading is applied in the axial direction, there is no membrane effect.

B.2 Exact solutions

Considering the loading by a concentrated force, the exact solution is

$$\begin{cases} w = \frac{F}{EI}[\frac{(x-L)^3}{6} - \frac{L^2x}{2} + \frac{L^3}{6}] - \frac{F}{Gt}x \\ \Phi = -\frac{F}{EI}[\frac{(x-L)^2}{2} - \frac{L^2}{2}] \end{cases} \tag{B.3}$$

In particular the tip displacements are

$$\begin{cases} w(L) = -\frac{FL^3}{3EI} - \frac{FL}{Gt} \\ \Phi(L) = \frac{FL^2}{2EI} \end{cases} \tag{B.4}$$

Note that these displacements reduce to the Bernoulli beam theory solution if we impose $G = +\infty$.

The exact strains are given by

$$\begin{cases} \gamma_{xz} = -\frac{F}{Gt} \\ \epsilon_{xx} = \frac{Fz}{EI}(L - x) \end{cases} \tag{B.5}$$

Considering the loading by a concentrated moment, the exact solution is

$$\begin{cases} w = -\frac{Cx^2}{2EI} \\ \Phi = \frac{Cx}{EI} \end{cases} \tag{B.6}$$

In particular the tip displacements are

$$\begin{cases} w = -\frac{CL^2}{2EI} \\ \Phi = \frac{CL}{EI} \end{cases} \tag{B.7}$$

This solution is the same as the one that is obtained in the Bernoulli beam theory because there is no shearing action involved.

The exact strains are given by

$$\begin{cases} \gamma_{xz} = 0 \\ \epsilon_{xx} = \frac{Cz}{EI} \end{cases} \tag{B.8}$$

B.3 Solutions with one finite element

We consider this beam modelled by a single finite element. The stiffness matrix for the 2-node mixed-formulated beam finite element assuming constant shear (considering the boundary conditions) is given by

$$\begin{pmatrix} \frac{Gt}{L} & \frac{Gt}{2} \\ \\ \frac{Gt}{2} & \frac{GtL}{4} + \frac{EI}{L} \end{pmatrix}. \tag{B.9}$$

Considering the force loading, the nodal displacements are

$$\begin{cases} w = -\frac{FL^3}{4EI} - \frac{FL}{Gt} \\ \Phi = \frac{FL^2}{2EI} \end{cases} \tag{B.10}$$

Also, the mixed-interpolated formulation yields the exact shear strain at every point in the beam and the exact bending strain at the element midpoint:

$$\begin{cases} \epsilon_{xx} = \frac{FLz}{2EI} \\ \gamma_s^{MI} = \frac{F}{Gt} \end{cases} \tag{B.11}$$

Considering the moment loading, the nodal displacements are

$$\begin{cases} w = -\frac{CL^2}{2EI} \\ \Phi = \frac{CL}{EI} \end{cases} \tag{B.12}$$

which is the exact solution (see Equation B.7). Also the mixed interpolated formulation gives the exact shear strain (which is zero) and the exact bending strains at all points in the beam:

$$\begin{cases} \epsilon_{xx} = \frac{C}{EI} z \\ \gamma_s^{MI} = 0 \end{cases} \tag{B.13}$$

B.4 Error measures with one finite element

In this section, based on the strains evaluated in Sections B.2 and B.3, we evaluate the error measure given in Equation 4.12, as it applies to this beam structure modelled using a single mixed-formulated finite element.

Considering the moment loading, since the exact strains are obtained at all points

in the beam, our error estimate, which in this case reduces to

$$EM(U, U_h) = \frac{t}{2} \int_{x=0}^{x=L} \Delta\epsilon_{xz} G \Delta\epsilon_{xz} + \Delta\epsilon_{xx} E \Delta\epsilon_{xx} dx \tag{B.14}$$

vanishes. This example illustrates the fact that the proposed error measure is a norm for the strain error but not for the displacements: as a matter of fact, in this example, the finite element solution in the displacement is not equal to the exact solution (For instance, the exact displacement w is a parabola given in Equation B.6, whereas the finite element solution is linear) but the error estimator vanishes because the strains are predicted exactly at every point.

In the case of the tip force loading, after some algebra, we find that

$$EM(U, U_h) = \frac{6F^2L^3}{EI} \tag{B.15}$$

and of course the only contribution to this error measure comes from the bending part of the strain energy since the element was shown to give the exact shear strain at every point in the beam.

B.5 Finite element solutions with N elements

We now consider the same two problems, but we now model the beam structure with N equally-sized mixed-interpolated finite elements.

It can be seen that with N elements instead of 1, the finite element solution verifies the following properties:

1. When the loading is a tip moment, the strains are predicted exactly at all points.

2. When the loading is a tip force, the shear strain is predicted exactly at all points and the bending strain is predicted exactly at the midpoint of each element.

We can make use of these two properties combined with the fact that the strains

in the element with nodes $n+1$ and n verify

$$\begin{cases} \gamma_{xz}^{AS} = \frac{w_{n+1}-w_n}{L/N} + \frac{\Phi_{n+1}+\Phi_n}{2} \\ \epsilon_{xx} = \frac{Nz}{L}(\Phi_{n+1} - \Phi_n) \end{cases} \tag{B.16}$$

(Note that these equations can be understood as two-point discretizations of Equation B.2) and the exact strains given by Equations B.5 and B.8 to attain expressions for the nodal displacements and rotations.

With some algebra, for the case of a tip moment, we obtain that the nodal displacements and rotations are given by

$$\begin{cases} w_n = -\frac{n^2}{2}\frac{CL^2}{EIN^2} \\ \Phi_n = n\frac{CL}{EIN} \end{cases} \tag{B.17}$$

where w_k and Φ_k denote the displacement and rotation of the k^{th} node (the nodes are numbered from 0 at the clamped end to N at the tip). We can see by comparing Equation B.17 and Equation B.6 that the mixed-formulated finite element considered gives the exact displacements and rotations at the nodes. In fact it gives the exact rotations at all points.

With some algebra, for the case of a tip force, we obtain that the nodal displacements and rotations are given by

$$\begin{cases} w_n = \frac{FL^3}{EIN^3}(\frac{n^3}{6} - \frac{Nn^2}{2} + \frac{n}{12}) - \frac{FLn}{GtN} \\ \Phi_n = (-\frac{1}{2}n^2 + Nn)\frac{FL^2}{EIN^2} \end{cases} \tag{B.18}$$

B.6 Error measure with N elements used

We can make use of Equations B.5, B.8, B.17, B.18, B.16 and B.14 to evaluate our proposed error measure of Equation 4.12.

In the case of the moment loading, it is clear that our error measure vanishes, since all strains are predicted exactly by the mixed element.

In the case of the force loading, with some algebra we obtain that $EM(U, U_h) =$

$\frac{F^2L^3}{2Et^3N^2}$.

From Equation B.4, we see that the strain energy in the exact solution is

$$E(U,U) = -\frac{1}{2}Fw(L) = \frac{F^2}{2}(\frac{L^3}{3EI} + \frac{L}{Gt}) \tag{B.19}$$

We make use of the fact that $I = t^3/12$ to express this strain energy in terms of t only:

$$E(U,U) = F^2(\frac{2L^3}{Et^3} + \frac{L}{2Gt}) \tag{B.20}$$

Hence the relative error for this problem is

$$RE(U,U_h) = \frac{EM(U,U_h)}{E(U,U)} = \frac{\frac{F^2L^3}{2Et^3N^2}}{F^2(\frac{2L^3}{Et^3} + \frac{L}{2Gt})} = \frac{1}{N^2}\ \frac{1}{4 + \frac{E}{G}(\frac{t}{L})^2} \tag{B.21}$$

Therefore we have

$$RE(U,U_h) \leq \frac{1}{4N^2} = \frac{h^2}{4L^2} \tag{B.22}$$

where $h = L/N$ is the element size. The fact that we could find an upper bound for the relative error of the form Ch^2 with C independent of t indicates that there is no locking[1], since the optimal order of convergence, which is 2 for the linear element element considered, is attained.

B.7 Alternative error measures

We have mentioned that our proposed error measure of Equation 4.12 is a norm for the strain error but is in general not a norm for the displacements [2]. This might be a difficulty for specific problems where we need to evaluate the error in the displacements with great accuracy. In this section, we comment on three alternative error measures that are norms for the displacements.

[1] Of course, in this problem only shear locking could be present.

[2] Our proposed error measure is a norm for the displacements when applied to a displacement-based finite element because in that case it reduces to $E(U - U_h, U - U_h)$.

B.7.1 Strain energy

In this section, we consider the strain energy as an alternative error measure:

$$\overline{EM}(U, U_h) = E(U - U_h, U - U_h) \tag{B.23}$$

This new error measure defines a norm for the displacements. It differs slightly from our proposed error measure (see Equation 4.12) in that in Equation B.23 we calculate the error in the displacements and then evaluate the corresponding strain using the usual displacement based displacement/strain operator, whereas in our proposed error measure we evaluate finite element strains from the nodal displacements using the mixed interpolations for those components of the strains that are mixed-interpolated and then subtract these strains from the exact strains to obtain the strain error.

Considering the problem with the tip force, using Equations B.5, B.8, B.17, B.18, B.16 and B.14, the definitions of the bending and shear strains and the proper interpolation functions, we find after some algebra that the contribution from the element with nodes n and $n+1$ to the bending part of the error measure $\overline{EM}$ is

$$\overline{EM}_{bn} = \frac{FL^2}{2EN^3t^3} \tag{B.24}$$

and for the shear part

$$\overline{EM}_{sn} = \frac{3}{2}\frac{GF^2L^5}{N^5E^2t^5}(4n^2 + 4n(1-2N) + 1 - 4N + 4N^2) \tag{B.25}$$

Totalling these contributions from all elements we find that the contribution to $\overline{EM}$ from bending is

$$\overline{EM}_b = \frac{F^2L^3}{2Et^3N^2} \tag{B.26}$$

and the contribution from shear is

$$\overline{EM}_s = \frac{N(4N^2-1)}{N^5}\frac{GF^2L^5}{2E^2t^5} \tag{B.27}$$

It should be noted that the contribution from bending is the same for this alternative error measure as for our proposed error measure, which comes immediately from the fact the bending strains are not mixed-interpolated in the element considered. The shear contribution differs however: in our proposed error measure there is no contribution from shear. It can be argued that from the point of view of the engineer, our error measure is in this regard more logical: considering that the shear strains are predicted exactly at all points in the structure, it is unexpected to have a non-zero contribution to the error measure coming from shear.

The relative error is

$$\overline{RE}(U,U_h) = \frac{\overline{EM}(U,U_h)}{E(U,U)} = \frac{\frac{F^2L^3}{2Et^3N^2} + \frac{N(4N^2-1)}{N^5}\frac{GF^2L^5}{2E^2t^5}}{F^2(\frac{2L^3}{Et^3} + \frac{L}{2Gt})} \tag{B.28}$$

and after simplification

$$\overline{RE}(U,U_h) = \frac{1}{N^2}\ \frac{1 + \frac{4N^2-1}{N^2}\frac{L^2}{t^2}\frac{G}{E}}{4 + \frac{E}{G}\frac{t^2}{L^2}} \tag{B.29}$$

This expression cannot be put in the form

$$\text{for } t \text{ small enough,} \quad \overline{RE}(U,U_h) \leq C\frac{1}{N^2} \tag{B.30}$$

with C a constant independent of the thickness t. As a matter of fact for t small enough, $\frac{1+\frac{(4N^2-1)}{N^2}\frac{L^2}{t^2}\frac{G}{E}}{4+\frac{E}{G}\frac{t^2}{L^2}}$ behaves as $\frac{4N^2-1}{4N^2}\frac{L^2}{t^2}\frac{G}{E}$ and goes to infinity as t goes to zero. Note that it is therefore the contribution to the error measure coming from shear that prevents Equation B.30 from holding. Hence, using the error measure $\overline{EM}$ we would get the impression that the element shear locks, although in reality the shear strain is predicted exactly at all points! [3]

[3]We implemented the error measure $\overline{EM}$ of Equation B.23 for shell problems and observed in this case also that the relative error $\overline{RE}$ can take surprisingly large values even when a reasonably accurate solution has been reached due to this effect.

B.7.2 $A_m + A_b$

An other error measure that has been proposed for the case of bending-dominated problems in [22] is

$$EM^*(U, U_h) = A_m(U - U_h, U - U_h) + A_b(U - U_h, U - U_h) \tag{B.31}$$

One advantage of this error measure is that it defines a norm equivalent to the norm for the space $\mathcal{V}$, as proven in [22]. Using Equations B.26 and B.27, we obtain immediately that

$$EM^*(U, U_h) = \frac{F^2 L^6}{t^6 N^2}[\frac{1}{2E} + \frac{G}{2E^2}\frac{4N^2 - 1}{N^4}] \tag{B.32}$$

and therefore the relative error in this norm is

$$RE^*(U, U_h) = \frac{EM^*(U, U_h)}{A_m(U, U) + A_b(U, U)} = \frac{\frac{F^2 L^6}{N^2 t^6}[\frac{1}{2E} + \frac{G}{2E^2}\frac{4N^2-1}{N^2}]}{F^2(\frac{2L^6}{Et^6} + \frac{L^2}{2t^2 G}]} \tag{B.33}$$

We can simplify this expression to

$$RE^*(U, U_h) = \frac{1}{N^2}\frac{\frac{1}{2E} + \frac{G}{2E^2}\frac{4N^2-1}{N^2}}{2 + \frac{t^4}{2L^4 G}} \tag{B.34}$$

and we can therefore put this in the form

$$RE^*(U, U_h) \leq C\frac{1}{N^2} \tag{B.35}$$

with C a constant independent of the thickness t. Hence in this error measure we find, similarly to our proposed error measure, that there is no locking.

One disadvantage of using $EM^*(U, U_h)$ as an error measure is that this method only applies in the case of bending-dominated problems and we need to resort to a different error measure to assess the performance of a finite element formulation in a membrane-dominated or mixed case for instance. Another disadvantage of this approach is that the physical relevance of EM^* is not immediate. The use of $A_m + A_b$

as an error norm for shells is demonstrated in Appendix C.

B.7.3 $EM + ||.||^2_{L^2}$

We mentioned in Section 4.1.3 that our proposed method could be modified into a norm for the displacements by adding to it the L^2 norm of the displacements, in the form

$$\overline{EM}(U, U_h) = EM(U, U_h) + C||u - u_h||^2_{L^2} + C'||\theta - \theta_h||^2_{L^2} \tag{B.36}$$

where we denote by u the translational degrees of freedom and θ the rotational degrees of freedom. In the case of the Timoshenko beam this expression simplifies to

$$\overline{EM}(U, U_h) = EM(U, U_h) + C\int_0^L (w - w_h)^2 dx + C'\int_0^L (\Phi - \Phi_h)^2 dx \tag{B.37}$$

From Equations B.3 and B.18, we evaluate

$$\int_0^L (w - w_h)^2 dx = \frac{F^2L^7}{E^2I^2}\frac{394N^3 - 8N}{N^7} \tag{B.38}$$

and

$$\int_0^L (\Phi - \Phi_h)^2 dx = \frac{F^2L^5}{120E^2I^2}\frac{1}{N^4} \tag{B.39}$$

As expected, both terms vary with N as $1/N^4$, whereas the error in the strains vary as $1/N^2$. Hence we have

$$\overline{EM}(U, U_h) = \frac{F^2L^3}{2Et^3N^2} + C\frac{F^2L^7}{E^2I^2}\frac{394N^3 - 8N}{N^7} + C'\frac{F^2L^5}{120E^2I^2}\frac{1}{N^4} \tag{B.40}$$

We can also evaluate the L^2 norms for the translations and rotations in the exact solution

$$\int_0^L w^2 dx = \frac{F^2L^3}{420E^2I^2G^2t^2}(11L^4G^2t^2 + 77L^2EIGt + 140E^2I^2) \tag{B.41}$$

and

$$\int_0^L \Phi^2 dx = \frac{2}{15}\frac{F^2L^5}{E^2I^2} \tag{B.42}$$

which show that these quantities vary like t^{-6} as t goes to zero. We could propose to use $C = t^3E/L^4$ and $C' = t^3E/L^2$. Defining

$$\overline{RE}(U, U_h) = \frac{EM(U, U_h) + C||w - w_h||^2_{L^2} + C'||\Phi - \Phi_h||^2_{L^2}}{E(U, U) + C||w||^2_{L^2} + C'||\Phi||^2_{L^2}} \tag{B.43}$$

this choice of constants would result in

$$\overline{RE}(U, U_h) = \frac{\frac{L^3}{2t^3N^2} + \frac{L^3t^3}{I^2}\frac{394N^3-8N}{N^7} + \frac{t^3}{L^2}\frac{L^5}{120I^2}\frac{1}{N^4}}{(\frac{2L^3}{t^3} + \frac{LE}{2Gt}) + \frac{t^4}{420LI^2G^2}(\frac{11L^4G^2}{t} + 77\frac{L^2EIG}{t^2} + 140\frac{E^2I^2}{t^3}) + \frac{t^3}{L^2}\frac{2}{15}\frac{L^5}{I^2}} \tag{B.44}$$

All three terms of the numerator and denominator vary like $1/t^3$ and the numerator varies with N as $1/N^2$, which implies that we have, for t small enough,

$$\overline{RE}(U, U_h) \leq C\frac{1}{N^2} \tag{B.45}$$

The disadvantage of the error measure $\overline{EM}$ is that it does not have a clear physical significance.

Appendix C

A_m and $A_m + A_b$ norms

In this appendix, we demonstrate the use of A_m and $A_m + A_b$ as error measures for membrane-dominated and bending-dominated problems, respectively. These error measures have been proposed in [22], where it is shown that $A_m + A_b$ defines a norm that is equivalent to $||.||_{\mathcal{V}}$. Some results obtained with these norms were presented in [41].

In Section B.7.2 we have applied the norm $Am + Ab$ to a bending-dominated beam problem. We recall that, in considering bending-dominated problems, we defined

$$EM^*(U, U_h) = A_m(U - U_h, U - U_h) + A_b(U - U_h, U - U_h) \tag{C.1}$$

and

$$RE^*(U, U_h) = \frac{EM^*(U, U_h)}{A_m(U, U) + A_b(U, U)} \tag{C.2}$$

For membrane-dominated cases we now add the definitions

$$EM^{**}(U, U_h) = A_m(U - U_h, U - U_h) \tag{C.3}$$

and

$$RE^{**}(U, U_h) = \frac{EM^{**}(U, U_h)}{A_m(U, U)} \tag{C.4}$$

For our numerical tests, we plot $RE^*(U_{ref}, U_h)$ (for the free hyperboloid) and $RE^{**}(U_{ref}, U_h)$

(for the clamped hyperboloid). Results obtained with the MITC4, MITC9 and MITC16 elements are reported in Figures C-1 and C-2.

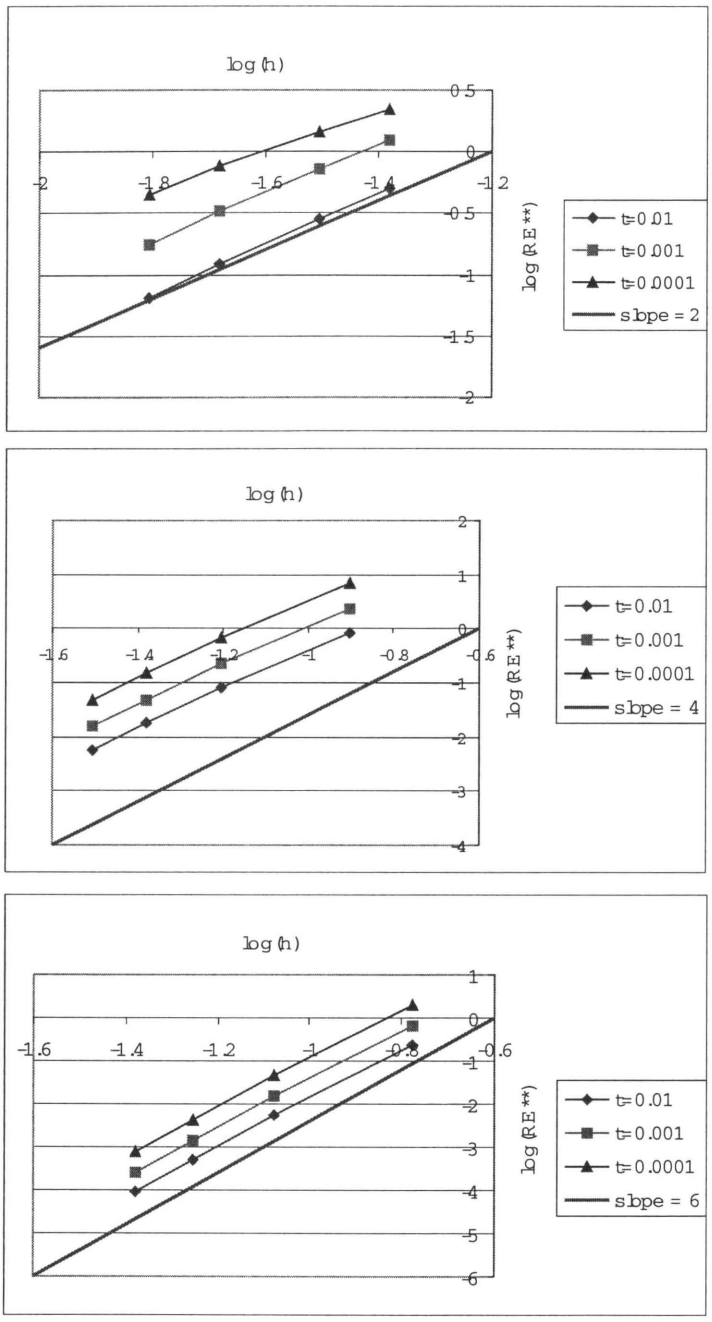

Figure C-1: Convergence of the MITC elements in the clamped hyperboloid problem, measured in A_m norm. Graded meshes are employed. Top to bottom: MITC4, MITC9, MITC16. RE^{**} denotes the relative error measure defined by $\frac{A_m(U_{ref}-U_h, U_{ref}-U_h)}{A_m(U_{ref}, U_{ref})}$.

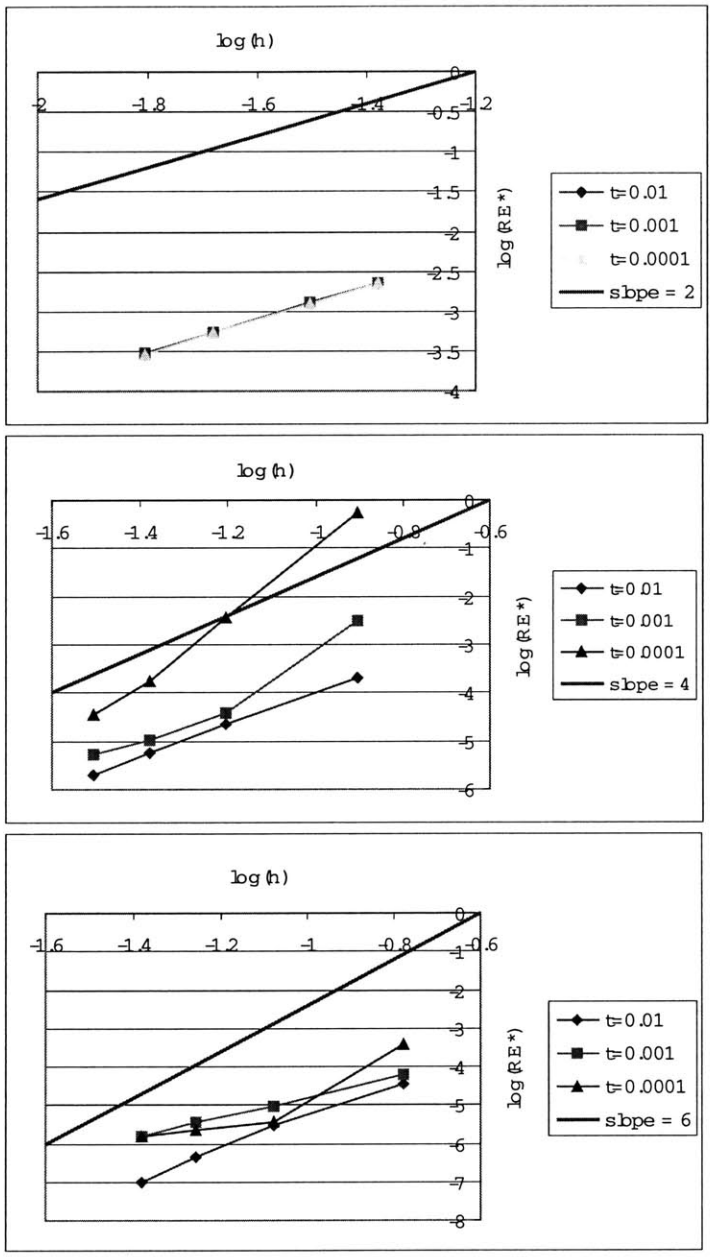

Figure C-2: Convergence of the MITC elements in the free hyperboloid problem, measured in $A_m + A_b$ norm. Graded meshes are employed. Top to bottom: MITC4, MITC9, MITC16. RE^* denotes the relative error measure defined by $\frac{(A_b+A_m)(U_{ref}-U_h, U_{ref}-U_h)}{(A_b+A_m)(U_{ref}, U_{ref})}$.

Appendix D

Modified MITC9 element

In this appendix, we present results obtained with a modified MITC9 element [3]. In Section D.1, we present the formulation and in Section D.2 we give the convergence curves obtained in the study of the hyperboloid problems introduced in Section 4.2 with the error measure presented in Section 4.1.3 as well as the error measures introduced in Appendix C.

D.1 Formulation of the modified MITC9 element

In Section 3.2 we presented the MITC9 formulation [3]. We now introduce a slightly modified formulation, which we denote by MITC9m. The aim is to improve on the performance of the MITC9 performance, which was analyzed in detail in Section 4.4 and in particular we aim at designing an element that does not feature the spurious shear strains observed in the free hyperboloid problem while possessing the other convergence and consistency properties of the MITC9 element.

The MITC9m formulation differs from the MITC9 in the location of the tying points employed for the transverse shear strains: instead of using the points of local coordinates $\{-\sqrt{\frac{3}{5}}, 0, \sqrt{\frac{3}{5}}\} \times \{-\frac{1}{\sqrt{3}}, \frac{1}{\sqrt{3}}\}$ for the strain e_{23}, we use the points of coordinates $\{-1, 0, 1\} \times \{-\frac{1}{\sqrt{3}}, \frac{1}{\sqrt{3}}\}$ (and permutation of r and s for e_{13}) . The tying schemes for the MITC9m formulation is then as indicated below, following the notations of Section 3.2.

MITC9m element

$$\begin{cases} n_{11} = 6 \\ \tilde{\mathcal{E}}^h_{11} = \text{span}\{1, r, s, rs, s^2, rs^2\} \\ \{(r^k_{11}, s^k_{11}), k \in \{1, .., n_{11}\}\} = \{-\frac{1}{\sqrt{3}}, \frac{1}{\sqrt{3}}\} \times \{-\sqrt{\frac{3}{5}}, 0, \sqrt{\frac{3}{5}}\} \end{cases} \tag{D.1}$$

$$\begin{cases} n_{22} = 6 \\ \tilde{\mathcal{E}}^h_{22} = \text{span}\{1, r, s, rs, r^2, sr^2\} \\ \{(r^k_{22}, s^k_{22}), k \in \{1, .., n_{22}\}\} = \{-\sqrt{\frac{3}{5}}, 0, \sqrt{\frac{3}{5}}\} \times \{-\frac{1}{\sqrt{3}}, \frac{1}{\sqrt{3}}\} \end{cases} \tag{D.2}$$

$$\begin{cases} n_{12} = 4 \\ \tilde{\mathcal{E}}^h_{12} = \text{span}\{1, r, s, rs\} = Q_1 \\ \{(r^k_{12}, s^k_{12}), k \in \{1, .., n_{12}\}\} = \{-\frac{1}{\sqrt{3}}, \frac{1}{\sqrt{3}}\} \times \{-\frac{1}{\sqrt{3}}, \frac{1}{\sqrt{3}}\} \end{cases} \tag{D.3}$$

$$\begin{cases} n_{13} = 6 \\ \tilde{\mathcal{E}}^h_{13} = \text{span}\{1, r, s, rs, s^2, rs^2\} \\ \{(r^k_{13}, s^k_{13}), k \in \{1, .., n_{13}\}\} = \{-\frac{1}{\sqrt{3}}, \frac{1}{\sqrt{3}}\} \times \{-1, 0, 1\} \end{cases} \tag{D.4}$$

$$\begin{cases} n_{23} = 6 \\ \tilde{\mathcal{E}}^h_{23} = \text{span}\{1, r, s, rs, r^2, sr^2\} \\ \{(r^k_{23}, s^k_{23}), k \in \{1, .., n_{23}\}\} = \{-1, 0, 1\} \times \{-\frac{1}{\sqrt{3}}, \frac{1}{\sqrt{3}}\} \end{cases} \tag{D.5}$$

With this formulation, ellipticity was verified. Namely, the stiffness matrix corresponding to an undistorted element integrated using $3 \times 3 \times 2$ Gaussian quadrature possesses exactly 6 zero eigenvalues corresponding to the 6 rigid body motions.

D.2 Performance of the MITC9m element

We first test the consistency of the MITC9m element by making use of our error measure in the clamped and free hyperboloid problems of Section 4.2. Reference solutions are obtained with the standard MITC9 element. Consistency curves, in Figure D-1, show that the solutions obtained with coarse MITC9m meshes converge to the reference solution with optimal convergence rate in both problems when graded meshes are used.

Table D.1: Consistency of the MITC9m element: error measure $EM(U_{ref}, U_h)$. The graded meshes employed are as described in Figure 4-7 with $w = 6\sqrt{t}$ in the case of the clamped hyperboloid and $w = 0.5\sqrt{t}$ in the case of the free hyperboloid. Reference solutions are obtained using a 96×96 MITC9 mesh.

t	N	Clamped hyperboloid	t	N	Free hyperboloid
	8	$0.36115547.10^{1}$		8	$0.10370282.10^{3}$
	16	$0.24685113.10^{0}$		16	$0.97671531.10^{1}$
10^{-2}	24	$0.48465478.10^{-1}$	10^{-2}	24	$0.24394495.10^{1}$
	32	$0.15186116.10^{-1}$		32	$0.84610499.10^{0}$
Ref. Energy		$0.53918715.10^{3}$	Ref. Energy		$0.45284688.10^{6}$
	8	$0.11627105.10^{2}$		8	$0.14557312.10^{7}$
	16	$0.77652754.10^{0}$		16	$0.26178373.10^{5}$
10^{-3}	24	$0.15226465.10^{0}$	10^{-3}	24	$0.62555838.10^{4}$
	32	$0.47649688.10^{-1}$		32	$0.28986428.10^{4}$
Ref. Energy		$0.60011496.10^{4}$	Ref. Energy		$0.44861047.10^{9}$
	8	$0.67414870.10^{2}$		8	$0.4466077.10^{10}$
	16	$0.29241326.10^{1}$		16	$0.47133493.10^{9}$
10^{-4}	24	$0.53161125.10^{0}$	10^{-4}	24	$0.44796142.10^{8}$
	32	$0.16407883.10^{0}$		32	$0.75962476.10^{7}$
Ref. Energy		$0.61898766.10^{5}$	Ref. Energy		$0.44874675.10^{12}$

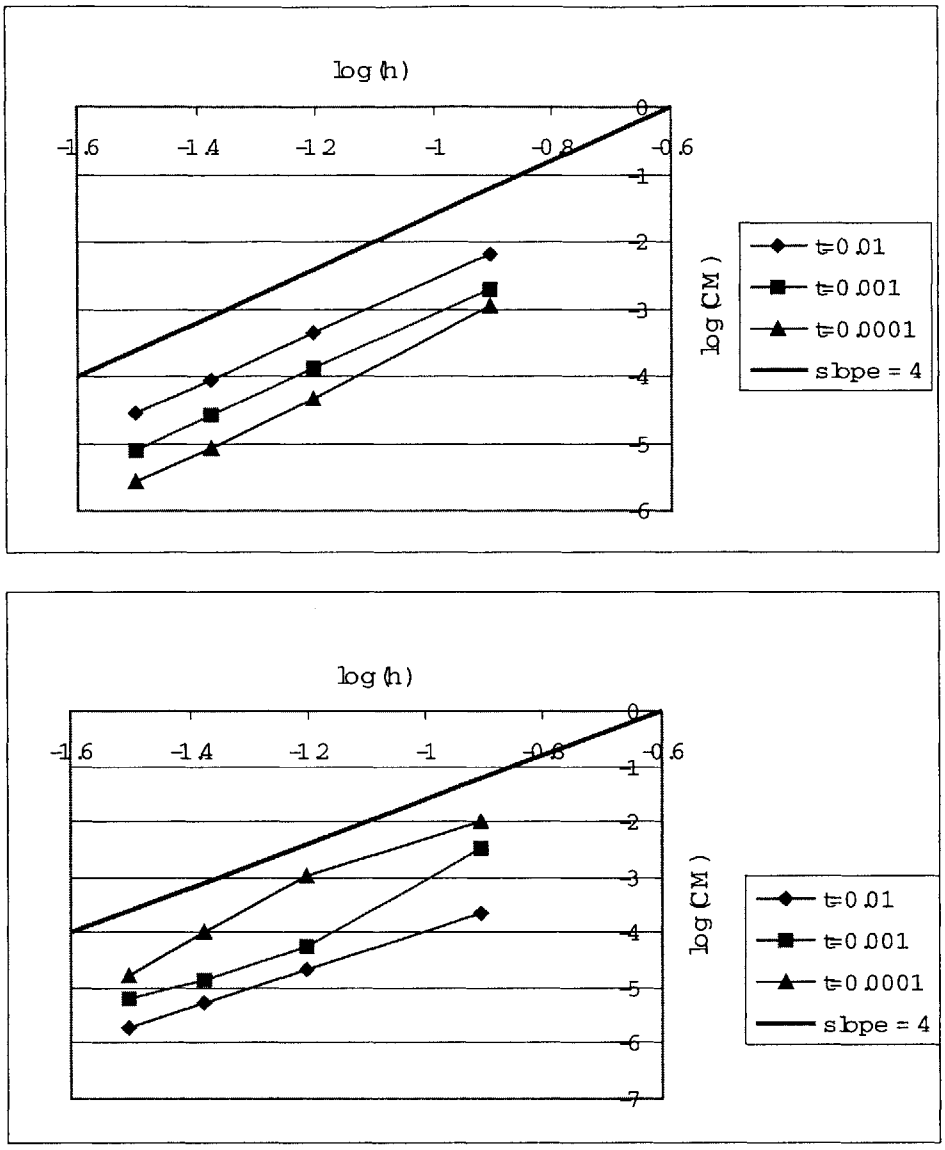

Figure D-1: MITC9m element: consistency. Top: clamped hyperboloid. Bottom: free hyperboloid. The same graded meshes are employed as for the MITC9 element in Section 4.4. CM denotes the consistency measure defined by $\frac{EM(U_{ref},U_h)}{E(U_{ref},U_{ref})}$.

Table D.2: Convergence of the MITC9m element: error measure $EM(U_{ref}, U_h)$ and reference energies $E(U_{ref}, U_{ref})$. The graded meshes employed are as described in Figure 4-7 with $w = 6\sqrt{t}$ in the case of the clamped hyperboloid and $w = 0.5\sqrt{t}$ in the case of the free hyperboloid. The reference strain energy corresponding to each pair of element and thickness is also listed. Reference solutions are obtained using a 96×96 MITC9m mesh.

t	N	Clamped hyperboloid	t	N	Free hyperboloid
	8	$0.36115547.10^{1}$		8	$0.10370270.10^{3}$
	16	$0.24685110.10^{0}$		16	$0.97670721.10^{1}$
10^{-2}	24	$0.48465434.10^{-1}$	10^{-2}	24	$0.24393836.10^{1}$
	32	$0.15186065.10^{-1}$		32	$0.84604594.10^{0}$
Ref. Energy		$0.53918715.10^{3}$	Ref. Energy		$0.45284689.10^{6}$
	8	$0.11627105.10^{2}$		8	$0.14557272.10^{7}$
	16	$0.77652744.10^{0}$		16	$0.26172363.10^{5}$
10^{-3}	24	$0.15226457.10^{0}$	10^{-3}	24	$0.62496493.10^{4}$
	32	$0.47649634.10^{-1}$		32	$0.28927112.10^{4}$
Ref. Energy		$0.60011496.10^{4}$	Ref. Energy		$0.44861096.10^{9}$
	8	$0.67414867.10^{2}$		8	$0.44637508.10^{10}$
	16	$0.29241312.10^{1}$		16	$0.47046110.10^{9}$
10^{-4}	24	$0.53161079.10^{0}$	10^{-4}	24	$0.44138314.10^{8}$
	32	$0.16407830.10^{0}$		32	$0.69531755.10^{7}$
Ref. Energy		$0.61898766.10^{5}$	Ref. Energy		$0.44852090.10^{12}$

Next, we study the convergence of the MITC9m solutions towards a reference solution established using the MITC9m element. Convergence curves are shown in Figure D-2 and are very similar to the consistency curves of Figure D-1, reflecting the fact that the reference solutions used in each case are very similar. We can compare these graphes to those for the standard MITC9 element, see Figures 4-10 and 4-12. We note that in the clamped case the MITC9m shows a downwards shifting pattern similar to that of the MITC9. In the free case, the MITC9m shows a markedly improved behavior over the MITC9 element, with significantly less upwards shifting and lower overall error levels at all thicknesses. This improvement is due to the fact that the MITC9m element does not show the spurious shear strains observed when the MITC9 element is employed.

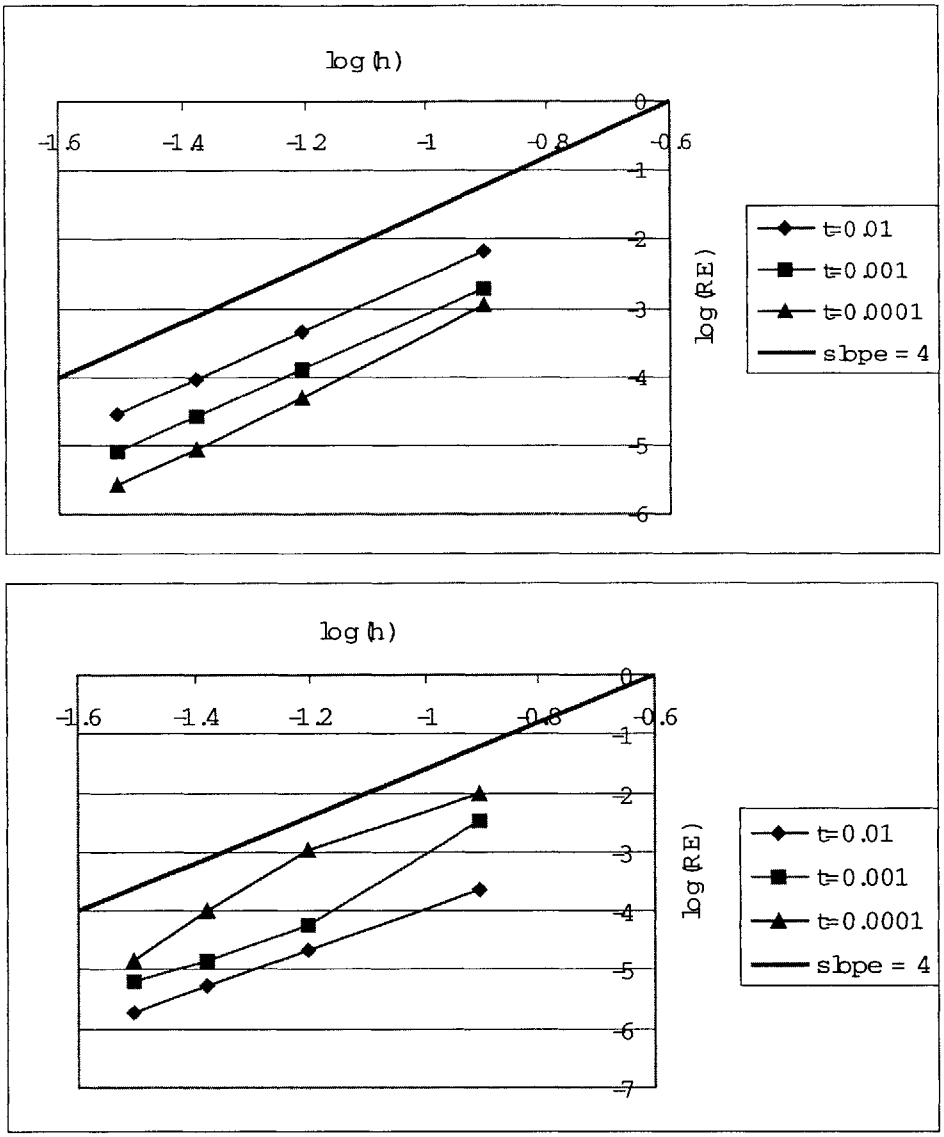

Figure D-2: Convergence of the MITC9m element in our error measure. Top: clamped hyperboloid. Bottom: free hyperboloid. Graded meshes are employed. RE denotes the relative error defined by $\frac{EM(U_{ref},U_h)}{E(U_{ref},U_{ref})}$.

Table D.3: Convergence of the MITC9m element in the alternative error measures A_m and $A_b + A_m$. In the case of the clamped hyperboloid, the error measure is $EM^{**} = A_m(U_{ref} - U_h, U_{ref} - U_h)$ and the reference energy is $A_m(U_{ref}, U_{ref})$. In the case of the free hyperboloid, the error measure is $EM^{*} = (A_m + A_b)(U_{ref} - U_h, U_{ref} - U_h)$ and the reference energy is $(A_m + A_b)(U_{ref}, U_{ref})$. The graded meshes employed are as described in Figure 4-7 with $w = 6\sqrt{t}$ in the case of the clamped hyperboloid and $w = 0.5\sqrt{t}$ in the case of the free hyperboloid. Reference solutions are obtained using a 96×96 MITC9m mesh.

t	N	Clamped hyperboloid	t	N	Free hyperboloid
	8	$0.4305880947.10^5$		8	$0.8836665295.10^8$
	16	$0.4250709711.10^4$		16	$0.1032012493.10^8$
10^{-2}	24	$0.9043990351.10^3$	10^{-2}	24	$0.2602084402.10^7$
	32	$0.2914403958.10^3$		32	$0.9078487631.10^6$
$A_m(U_{ref}, U_{ref})$		$0.5168073413.10^5$	$(A_m + A_b)(U_{ref}, U_{ref})$		$0.4488212531.10^{12}$
	8	$0.1487134002.10^8$		8	$0.6493011952.10^{15}$
	16	$0.1351746429.10^7$		16	$0.1198651055.10^{14}$
10^{-3}	24	$0.2867979515.10^6$	10^{-3}	24	$0.4764975198.10^{13}$
	32	$0.9234574983.10^5$		32	$0.2431841018.10^{13}$
$A_m(U_{ref}, U_{ref})$		$0.593282783.10^7$	$(A_m + A_b)(U_{ref}, U_{ref})$		$0.4485459071.10^{18}$
	8	$0.2495755932.10^{11}$		8	$0.3999417824.10^{22}$
	16	$0.6531698437.10^9$		16	$0.2392537927.10^{21}$
10^{-4}	24	$0.9373180083.10^8$	10^{-4}	24	$0.1068940464.10^{20}$
	32	$0.2912931662.10^8$		32	$0.1450482115.10^{19}$
$A_m(U_{ref}, U_{ref})$		$0.6171951438.10^9$	$(A_m + A_b)(U_{ref}, U_{ref})$		$0.4487169166.10^{24}$

Finally, we show in Figure D-3 the convergence curves corresponding to the A_m and $A_b + A_m$ norm for the clamped and free hyperboloid respectively.

Clearly, further testing of the MITC9m element is necessary to gain more insight into its behavior.

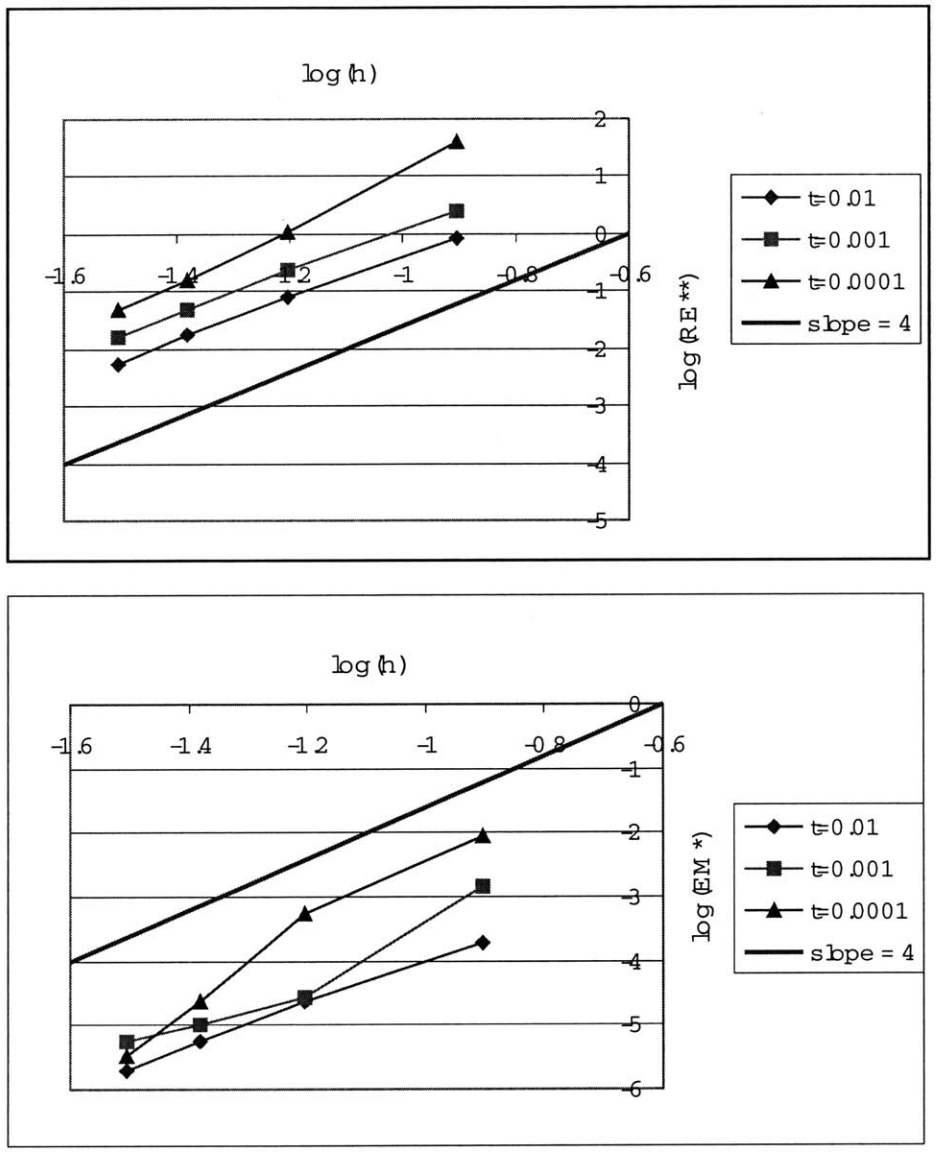

Figure D-3: Convergence of the MITC9m element in alternative error measures. Top: clamped hyperboloid. Bottom: free hyperboloid. Graded meshes are employed. RE^{**} denotes the relative error measure defined by $\frac{A_m(U_{ref}-U_h, U_{ref}-U_h)}{A_m(U_{ref}, U_{ref})}$, and RE^{*} denotes the relative error measure defined by $\frac{(A_b+A_m)(U_{ref}-U_h, U_{ref}-U_h)}{(A_b+A_m)(U_{ref}, U_{ref})}$.

Bibliography

[1] M. Ainsworth and J.T. Oden. *A posteriori error estimation in finite element analysis.* John Wiley & Sons, 2000.

[2] F. Auricchio, L. Beirão da Veiga, and C. Lovadina. Remarks on the asymptotic behaviors of koiter shells. *Computers & Structures*, pages 735–745, 2002.

[3] K.J. Bathe et al. Towards improving the MITC9 shell element, in preparation.

[4] K.J. Bathe and F. Brezzi. A simplified analysis of two plate bending elements – The MITC4 and MITC9 elements. *Proceedings, Conference NUMETA 87, University College of Swansea, Wales*, July 1987.

[5] K.J. Bathe, D. Chapelle, and P.S. Lee. A shell 'highly-sensitive' to thickness changes. *International Journal for Numerical Methods in Engineering.* submitted.

[6] K.J. Bathe and E. Dvorkin. A four-node plate bending element based on Mindlin/Reissner plate theory and a mixed interpolation. *International Journal for Numerical Methods in Engineering*, 21:367–383, 1985.

[7] K.J. Bathe and E. Dvorkin. A formulation of general shell elements - the use of mixed interpolation of tensorial components. *International Journal for Numerical Methods in Engineering*, 22:697–722, 1986.

[8] K.J. Bathe, J.F. Hiller, and H. Zhang. *On the finite element analysis of shells and their full interaction with Navier-Stokes fluid flows.* Computational Structures Technology (B.H.V. Topping, ed.). Civil-Comp Press, 2002.

[9] K.J. Bathe, A. Iosilevich, and D. Chapelle. An evaluation of the MITC shell elements. *Computers & Structures*, 75:1–20, 2000.

[10] K.J. Bathe, A. Iosilevich, and D. Chapelle. An inf-sup test for the shell finite elements. *Computers & Structures*, 75:439–456, 2000.

[11] K.J. Bathe. *Finite element procedures.* Prentice Hall, 1996.

[12] K.J. Bathe. The inf-sup condition and its numerical evaluation for mixed finite element methods. *Computers & Structures*, 79:243–252, 971, 2001.

[13] L. Beirão da Veiga. Asymptotical energy behaviour of two classical intermediate benchmark shell problems. In preparation.

[14] T. Belytschko and W.K. Liu. Test problems and anomalies in shell finite elements. *Reliability of methods for engineering analysis*, pages 393–406, 1986.

[15] F. Brezzi, K.J. Bathe, and M. Fortin. Mixed-interpolated elements for Reissner-Mindlin plates. *International Journal for Numerical Methods in Engineering*, 28:1787–1801, 1989.

[16] F. Brezzi and K.J. Bathe. Studies of finite element procedures -the inf-sup condition, equivalent forms and applications. In *Proceedings of the International Conference on Reliability of Methods for engineering analysis*, pages 197–220, University College, Swansea, 1986.

[17] M.L. Bucalem. *On higher-order mixed-interpolated general shell elements.* PhD thesis, Massachusetts Institute of Technology, 1992.

[18] M. Bucalem and K.J. Bathe. Higher-order MITC general shell elements. *International Journal for Numerical Methods in Engineering*, 36:3729–3754, 1993.

[19] D. Chapelle and K.J. Bathe. Fundamental considerations for the finite element analysis of shell structures. *Computers & Structures*, 66:19–36, 1998.

[20] D. Chapelle and K.J. Bathe. On general shell finite elements and mathematical shell models. *Advances in finite element procedures and techniques, B.H.V. Topping ed.*, pages 25–30, 1998.

[21] D. Chapelle and K.J. Bathe. The mathematical shell model underlying general shell elements. *International journal for numerical methods in engineering*, 48:289–313, 2000.

[22] D. Chapelle and K.J. Bathe. *The finite element analysis of shells – fundamentals.* Springer-Verlag, in press.

[23] S.H. Crandall, N.C. Dahl, and T.J. Lardner. *An introduction to the mechanics of solids, second edition with SI units.* McGraw-Hill, 1999.

[24] E. Dvorkin and K.J. Bathe. A continuum mechanics based four-node shell element for general non-linear analysis. *Engineering Computations*, 1:77–88, 1984.

[25] M. Farshad. *Design and analysis of shell structures.* Kluwer Academic Publishers, 1992.

[26] W. Flügge. *Stresses in shells, second edition.* Springer-Verlag, 1973.

[27] A.L. Gol'denveiser. *Theory of thin elastic shells.* Pergamon Press, 1961.

[28] A.E. Green and W. Zerna. *Theoretical elasticity, second edition.* Oxford University Press, 1968.

[29] J.F. Hiller and K.J. Bathe. On higher-order-accuracy points in isoparametric finite element analysis and an application to error assessment. *Computers & Structures*, pages 1275–1285, 2001.

[30] J.F. Hiller and K.J. Bathe. Precis of functional analysis for engineers. *Finite Element Research Group Report*, 2002.

[31] J.F. Hiller, S. De, and K.J. Bathe. *On the state-of-the-art of finite element procedures and a meshless technique.* Computational Mechanics for the Twenty-First Century (B.H.V. Topping, ed.). Saxe-Coburg Publications, 2000.

[32] J.F. Hiller. On error estimators in finite element analysis. Master's thesis, Massachusetts Institute of Technology, 1999.

[33] E. Hinton. Benchmark testing of finite element software. In *Proceedings of the International Conference on Reliability of Methods for engineering analysis*, pages 375–391, University College, Swansea, 1986.

[34] A. Iosilevich, K.J. Bathe, and F. Brezzi. On evaluating the inf-sup condition for plate bending elements. *International Journal for Numerical Methods in Engineering*, 40:3639–3663, 1997.

[35] A. Iosilevich. *Towards optimal mixed finite elements for general shell structures.* PhD thesis, Massachusetts Institute of Technology, 1999.

[36] L.G. Jaeger. *Elementary theory of elastic plates.* Pergamon Press, 1964.

[37] M. Jawad. *Theory and design of plate and shell structures.* Chapman and Hall, 1994.

[38] V. Kelkar and R. Sewell. *Fundamentals of the analysis and design of shell structures.* Prentice-Hall, 1987.

[39] L.D. Landau and E.M. Lifshitz. *Theory of elasticity, second edition.* Pergamon Press, 1970.

[40] P.S. Lee and K.J. Bathe. On the asymptotic behavior of shell structures and the evaluation in finite element solutions. *Computers & Structures*, 80:235–255, 2002.

[41] D. Lepikson Carvalho de Oliveira. *Formulação e estudo de confiabilidade de elementos finitos mistos para o modelo de casca de Naghdi.* PhD thesis, Escola Politecnica da Universidade de São Paulo, 2001.

[42] C. Lovadina. Energy estimates for linear elastic shells. *Proceedings of the First M.I.T. Conference on Computational Fluid and Solid Mechanics*, pages 330–331, 2001.

[43] A.E.H. Love. *Treatise on the mathematical theory of elasticity, fourth edition.* Dover Publications, 1944.

[44] E.H. Mansfield. *The bending and stretching of plates.* Pergamon Press, 1964.

[45] R.D. Mindlin. Influence of rotary inertia and shear on flexural motion of isotropic elastic plates. *Journal of Applied Mechanics*, 18:31–38, 1951.

[46] P.M. Naghdi. *Foundations of elastatic shell theory.* Berkeley: Institute of Engineering Research, University of California, 1962.

[47] J. Pitkäranta, Y. Leino, O. Ovaskainen, and J. Piila. Shell deformation states and the finite element method: A benchmark study of cylindrical shells. *Computer Methods in Applied Mechanics and Engineering*, 128:81–121, 1995.

[48] J. Pitkäranta, A.M. Matache, and C. Schwab. Fourier mode analysis of layers in shallow shell deformations. *Computer Methods in Applie Mechanical Engineering*, 190:2943–2975, 2001.

[49] J. Pitkäranta and E. Sanchez-Palencia. On the asymptotic behaviour of sensitive shells with small thickness. *Compte-Rendus de l'Académie des Sciences, Serie II*, pages 127–134, 1997.

[50] E. Reissner. The effect of transverse shear deformation on the bending of elastic plates. *Journal of Applied Mechanics*, 67:A69–A77, 1945.

[51] J.D. Renton. *Matrix and tensor analysis of elastic continua.* John Wiley & Sons, 1987.

[52] J. Salençon. *Mécanique des milieux continus.* Presses de l'Ecole Polytechnique, 1995.

[53] J. Sanchez-Hubert. Boundary and internal layers in thin elastic shells. *Proceedings of the First M.I.T. Conference on Computational Fluid and Solid Mechanics*, pages 452–453, 2001.

[54] E. Sanchez-Palencia. Statique et dynamique des coques minces. i. cas de flexion pure inhibée – approximation membranaire. *Compte-Rendus de l'Académie des Sciences, Serie I*, pages 531–537, 1989.

[55] E. Sanchez-Palencia. Statique et dynamique des coques minces. i. cas de flexion pure non inhibée. *Compte-Rendus de l'Académie des Sciences, Serie I*, pages 411–417, 1989.

[56] E. Sanchez-Palencia. Theoretical and numerical aspects of singularities, layers and local locking. *Elastic Shells, Modelling, Analysis and Numerics*, 2000.

[57] S. Timoshenko and J.N. Goodier. *Theory of elasticity.* McGraw-Hill, 1951.

[58] S. Timoshenko and S. Woinowski-Krieger. *Theory of plates and shells.* McGraw-Hill, 1959.

[59] C.M. Wang, J.N. Reddy, and K.H. Lee. *Shear deformable beams and plates.* Elsevier, 2000.

[60] K. Washizu. *Variational methods in elasticity and plasticity, second edition.* Pergamon Press, 1974.

Nomenclature

Δe Strain error, page 89

ϵ Dimensionless thickness: ratio of the shell thickness to a typical length. $\epsilon = t/L$, page 47

ϵ_{xx} Bending strain in the Timoshenko beam , page 137

γ_s^{MI} Mixed interpolated transverse shear strain in the Timoshenko beam , page 139

γ_{xz} Engineering transverse shear strain in the Timoshenko beam , page 137

ν Poison ratio, page 26

Φ Rotation of the Timoshenko beam sections , page 137

Φ_n Timoshenko beam nodal rotation , page 141

Π Mapping of the geometry, page 88

${}^0\vec{g}^i$ Local base vectors in the undeformed configuration , page 24

${}^1\vec{g}^i$ Local base vectors in the deformed configuration , page 24

A_b^h Finite element bending form , page 71

A_b^K Bending operator in the Koiter model , page 30

A_b^N Bending operator in the Naghdi model , page 29

A_m^h Finite element membrane and shear form , page 71

A_m^K Membrane operator in the Koiter model , page 30

A_m^N Membrane and shear operator in the Naghdi model , page 29

B Finite element strain displacement matrix , page 74

B^{AS} Assumed strains strain displacement matrix , page 73

B^{DI} Displacement-based train displacement matrix , page 67

C Constitutive law matrix, including the assumption of no through-thickness stresses , page 74

CM Consistency measure, page 107

E Young's modulus, page 26

$E(.,.)$ Strain energy operator , page 38

$E(\epsilon)$ Strain energy, page 38

e_h Finite element cartesian strains , page 107

e_{ref} Reference cartesian strains , page 106

EM Error measure, page 89

F_b Scaled loading functional for the bending-dominated case , page 39

F_m Scaled loading functional for the membrane-dominated case , page 36

G Shear modulus, page 136

$G(.)$ Loading functional, page 36

I Second moment of the Timoshenko beam cross-section , page 137

K Stiffness matrix, page 74

k Compressibility modulus, page 26

K_{el} Element stiffness matrix , page 67

L Typical length, page 47

M Bending moment in Timoshenko beam , page 137

Q Shear force in Timoshenko beam , page 137

R Ratio of bending energy to strain energy , page 39

R_{min} Radius of curvature with the smallest absolute value , page 22

RE Relative error measure, page 110

t Thickness, page 22

U^{ϵ} Solution of the shell problem for a given relative thickness ϵ , page 36

U_h Finite element solution, page 66

w z direction translation of the Timoshenko beam centerline , page 137

w_n Timoshenko beam nodal displacement , page 141

$\mathcal{BC}$ Boundary conditions , page 33

$\mathcal{U}_0$ Functional space of inextensional displacements , page 35

$\mathcal{V}$ Basic functional space , page 32

$\mathcal{V}^K$ Functional space for the Koiter model , page 33

$\mathcal{V}^N$ Functional space for the Naghdi model , page 33

$\mathcal{V}_m$ Functional space obtained by completion of $\mathcal{V}$ with respect to the membrane operator , page 37

$\chi_{\alpha\beta}$ Bending strain , page 25

$\delta_{\alpha\beta}$ Second order strain component , page 25

η_λ Virtual rotation of the mid-surface , page 27

$\gamma_{\alpha\beta}$ Membrane strain , page 25

λ, μ Lamé constants , page 26

$\overset{2}{\underset{\epsilon}{\rightarrow}}$ Green-Lagrange strain tensor , page 24

$\vec{\phi}$ Mapping function , page 22

$\overset{2}{\vec{\sigma}}$ Stress tensor , page 25

$\overset{4}{\underset{\sim}{C}}$, $\overset{2}{\underset{\sim}{D}}$ Shell material law tensors , page 26

$\overset{2}{\vec{e}}$ Linearized Green-Lagrange strain tensor , page 24

$\vec{F}$ Loading per unit volume , page 27

$\vec{g^i}$ Local base vectors , page 24

$\overset{4}{\vec{H}}$ Material law tensor , page 26

$\vec{U}$ Displacement vector , page 23

$\vec{u}$ Displacement vector for the mid-surface , page 23

$\vec{V}$ Virtual displacement , page 27

$\vec{v}$ Virtual displacement of the mid-surface , page 27

$\vec{x}$ Locator vector , page 22

μ Limit value of $R(\epsilon)$ as ϵ goes to zero , page 39

Ω Domain occupied by the shell , page 21

ω Domain in the local coordinates , page 22

θ_λ Rotations of a fiber perpendicular to the mid-surface , page 23

ξ^i Local shell coordinates , page 22

ζ_α Shear strain , page 25